Identification of Morphologic Parameters Affecting the Prognosis of Lung Squamous Cell Carcinoma Patients by Quantitative Image Analysis

---

Dissertation

zur

Erlangung der naturwissenschaftlichen Doktorwürde
(Dr. sc. nat.)

vorgelegt der

Mathematisch-naturwissenschaftlichen Fakultät

der

Universität Zürich

von

Ruben Casanova Benito

aus

Spanien

Promotionskommission

Prof. Dr. Bernd Bodenmiller (Leitung der Dissertation)
Prof. Dr. Renato Pajarola
Prof. Dr. Alex Soltermann
Prof. Dr. Holger Moch

Zürich, 2017

Table of contents

Summary

Accurate stratification of tumors is an imperative step for adequate cancer management. In addition to staging, morphological subtyping allows stratifying patients into additional prognostic groups. In this thesis, we have used an image-based computational method on pan-cytokeratin immunohistochemical (IHC) stainings to quantify clinically relevant morphologic parameters.

We conducted our analysis on surgically resected lung squamous cell carcinomas (LSCC) and identified tumor fragmentation (TF), as a measure of tumor invasiveness. We showed on two independent clinical cohorts from tissue microarrays (TMA) and whole sections (WS) that this novel parameter was associated with poor prognosis and increased risk of blood vessel infiltration. The poor prognostic value of increasing TF was further confirmed in a third cohort from the cancer genome atlas (TCGA) using a similar human-based score on haematoxylin-eosin (H&E) histochemical stainings. The integration of mRNAseq data from TCGA, and LC-MS/MS proteomics from WS, revealed an up-regulation of extracellular matrix remodeling and focal adhesion processes in tumors with high TF, supporting their increased invasive potential. The proposed histologic parameter is an independent unfavorable prognostic marker that could be envisaged as new grading parameter for LSCC.

We extended our analysis on neoadjuvant chemotherapy treated LSCC in order to characterize the histopathologic response to treatment using quantitative morphologic parameters. In this setting, chemotherapy is given before surgery thus potentially reducing the tumor burden before tumor resection. For this analysis, a cohort of chemo-naïve patients was used for comparison. After neoadjuvant chemotherapy, tumor area ($Tumor_{area}$), the percentage of tumor cells ($Tumor_{\%}$) as well as the amount (TF) and size of the largest residual fragment

($Size_{max}$) were significantly reduced compared to chemo-naïve LSCC. Positron Emission Tomography / Computed Tomography (PET/CT) measurements were integrated for subsequent correlation analysis against quantitative morphometric parameters. An initial study was conducted to assess which PET metrics correlated best with histopathologic tumor regression (TRG) scored, using a classic visual scoring system for non-small cell lung carcinomas. Our analysis showed that background adaptive PET volume metrics of the metabolic tumor volume (BSV) and total lesion glycolysis (BSL) correlated better with histopathological TRG than methods using a fixed threshold (42%) of the maximum standard uptake value SUVmax. Following on these findings, we evaluated and found that $tumor_{area}$ was the morphologic parameter best correlating with SUVmax, BSL and BSV post chemotherapy whereas PET metric before neaoadjuvant therapy were not associated to any morphologic parameter.

Survival analysis of the morphologic parameters showed that $Tumor_{\%,}$ $Tumor_{area}$ and $Size_{max}$ were able to stratify patients into risk categories based on a 3-years overall survival cutoff, whereas TF was the only significant parameter for chemo-naïve LSCC. Quantitative and automatic measurements of the remaining tumor burden could therefore provide the basis of an objective TRG system.

In this doctoral thesis, we highlighted the relevance of using image-based computational methods to supervise pathologists for tumor classification, particularly for lung squamous cell carcinoma. The proposed approach is not restricted to this particular subtype, and is potentially applicable to score morphologic and eventually prognostic parameters for other carcinomas.

Zusammenfassung

Eine angemessene Stratifizierung von Tumoren ist unerlässlich für eine bestmögliche Krebsbehandlung. Neben der Bestimmung des Tumorstadiums verhilft eine morphologische Subtypisierung zur Unterteilung in zusätzliche prognostische Subgruppen.

In der vorliegenden Arbeit wurde eine bildbasierte Berechnungsmethode für die Quantifizierung von klinisch relevanten morphologischen Merkmalen anhand von pan-Zytokeratin-immunhistochemischen Färbungen (IHC) eingesetzt. Durch Analysen von operativ entfernten Plattenepithelkarzinomen der Lunge (LSCC), wurden Tumorfragmentierungen (TF) als Maß für die Invasivität von Tumoren ermittelt.

Zwei unabhängige klinische Studien, von denen tissue microarrays (TMAs) und Gewebeschnitte (WS) untersucht wurden, zeigten, dass dieser neue Parameter mit einer schlechteren Prognose und einem erhöhten Blutgefässinfiltrationsrisiko korreliert. Die Aussagekraft einer hohen TF als ungünstiger prognostischer Marker wurde an einer dritten Kohorte aus der TCGA-Datenbank bestätigt. Hierbei wurde eine ähnliche subjektive Auswertung (Scoring) für HE-Färbungen eingesetzt. mRNAseq-Daten aus der TCGA-Datenbank und LC-MS/MS Proteom-Daten aus den WS zeigten verstärktes «Remodelling» der extrazellulären Matrix und der fokalen Adhäsionen in Tumoren mit hoher TF, was die erhöhte Invasivität unterstützt. Der hier beschriebene histologische Parameter ist ein unabhängiger prognostischer Marker, der als neuer Faktor für die Stadiums Bestimmung von LSCC herangezogen werden könnte.

Um das histopathologische Ansprechen mittels quantitativer morphologischer Parameter zu charakterisieren, wurde die Studie mit Patienten unter Einfluss von neoadjuvanter Chemotherapie erweitert. Um eine potentielle Tumorlast vor der Resektion zu reduzieren, wurde den Patienten vor der Operation Chemotherapie verabreicht. Bei dieser Analyse wurden

chemo-naive Patienten als Kontrollgruppe herangezogen. Nach neoadjuvanter Chemotherapie waren sowohl das Tumorareal und der Prozentanteil an Tumorzellen, als auch die Menge und Grösse der grössten Restfragmente signifikant reduziert im Vergleich zu den chemo-naiven LSCCs. Die Korrelation von PET/CT Messungen mit quantitativen morphometrischen Parametern wurde in der nachfolgenden Analyse untersucht. Es wurde eine Studie, die auf einer klassischen visuellen Auswertung für NSCLC basiert, durchgeführt. Hierbei sollte untersucht werden, welche PET-Metrik am besten mit der ausgewerteten histopathologischen Tumorregression (TRG) korreliert. Unsere Analyse zeigt, dass die adaptive PET-Hintergrundsvolumenmetrik des metabolischen Tumorvolumens (BSV) und der totalen Läsionsglykolyse (BSL) besser mit der histopathologischen TRG korreliert als Methoden, die einen festen Prozentsatz (42%) von der maximalen Standardaufnahme SUVmax verwenden. Im Anschluss zeigte sich, dass man anhand des Tumoranteils (%), der Tumorarea und der maximalen Grösse, die Patienten in drei Risikokategorien, hinsichtlich deren 3-Jahre Gesamtüberleben, unterteilen konnte. Dagegen war die TF der einzige signifikante Parameter bei den chemo-naiven LSCC. Quantitative automatische Messungen der Resttumorlast könnte die Basis für eine objektive TRG bieten.

In der vorliegenden Dissertation wurde die Relevanz von bildbasierten Berechnungsmethoden unterstrichen, die den Pathologen bei der Tumorklassifikation unterstützen können, insbesondere bei LSCC. Der dargestellte Ansatz ist nicht auf einen spezifischen Subtyp begrenzt und kann potentiell für die Auswertung von morphologischen und letztendlich prognostischen Parametern anderer Karzinome angewandt werden.

Chapter 1

Introduction

Lung cancer epidemiology

Lung cancer is the most frequent cancer worldwide with more than 1.8 million newly diagnosed cases in 2012, as indicated in the latest World Cancer Report 2014. It is also the leading cause of cancer deaths with an estimate of 1.6 million deaths, followed by liver and stomach cancer (1). The disease is largely attributed to tobacco smoking habits with estimated 90% to 95% of European and North American cases for men and 74% to 85% for women (2). In addition, smokers have a 10 to 20-fold increased risk of lung cancer as opposed to never smokers (3). Additional risk factors include radon exposure, asbestos, metals, silica dust among others in addition to radiation such as X-rays and gamma rays (4-9). In Switzerland, lung cancer is also the most frequent cause of cancer death, with approximately 3000 people dying each year (10). This accounts for 22% of all cancer deaths among men and 14.9% among women (Figure 1).

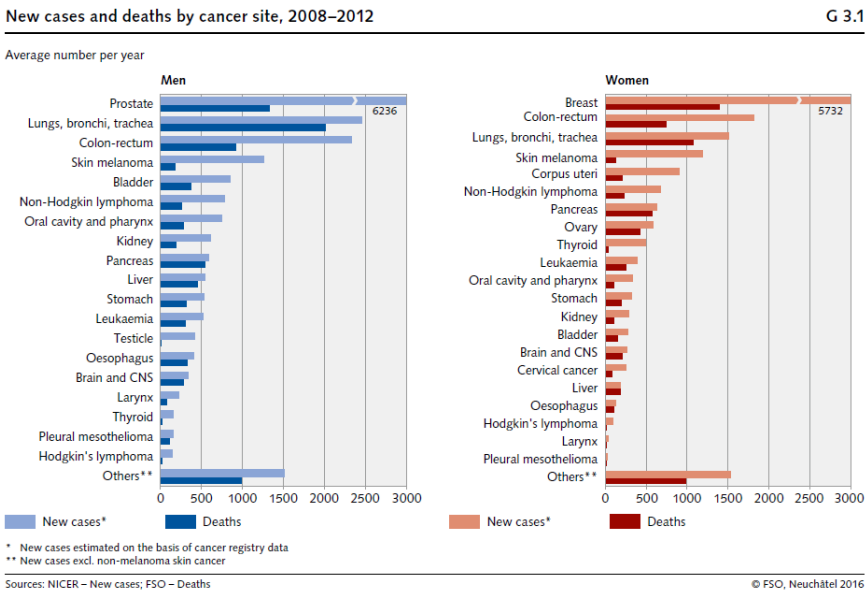

Figure 1: New cases and deaths by cancer site, 2008-2012. Arnt *et al.* Swiss Cancer Report 2015. Bar plots showing the number of new cases and deaths per cancer stratified by sex.

Lung cancer types

Lung carcinoma is a malignancy of the lung and respiratory tracts and comprises two main groups: small cell lung carcinoma (SCLC) and non-small cell lung carcinoma (NSCLC). NSCLC is the most frequent type and accounts for 85% of all lung cancers. The two major subtypes of NSCLC are adenocarcinoma (ADC) and lung squamous carcinoma (LSCC) - the latter representing 25-30% of all lung cancer in Europe (11). Lung cancer arises in different anatomical compartments of the lung, thus giving rise to distinct major histological types (Figure 2) (12). NSCLC is an epithelial malignancy assumed to originate from alveolar or bronchial epithelial cells, whereas SCLC is thought to arise from cells showing neuro-endocrine features and eventual stemness traits (13, 14). In general, LSCC and SCLC are preferentially located in the central compartments of the lung, which include large branching bronchi and bronchioles. ADC is considered to arise from the peripheral compartments of the lung, where terminal bronchioles are more represented.

Tumor imaging and clinical staging

Initial staging of lung cancer generally starts with a radiographic imaging of the chest in order to perform a pre-assessment of the tumor extent of the disease. The clinical TNM staging (primary tumor, lymph nodes and distant metastasis) is nowadays performed by computed tomography (CT) in combination with positron emission tomography (PET), since it is a non-invasive approach to measure tumor size, mediastinal node enlargement, and potential metastases. (15, 16). PET has a poorer resolution than CT and is not adequate to measure the local extent of the tumor. However, it is a readout for the tumor metabolic activity, which is usually measured using the standardized uptake value (SUV). This method is useful to differentiate malignant lesions, which are hyper-metabolic, from benign lesions (17). In addition, PET-CT scans may allow reducing the number of futile thoracotomies but does not

seem to affect patient's survival (18). However, PET-CT alone is not sensitive and specific enough to guide disease management which would require tissue biopsies before deciding further treatment options (19).

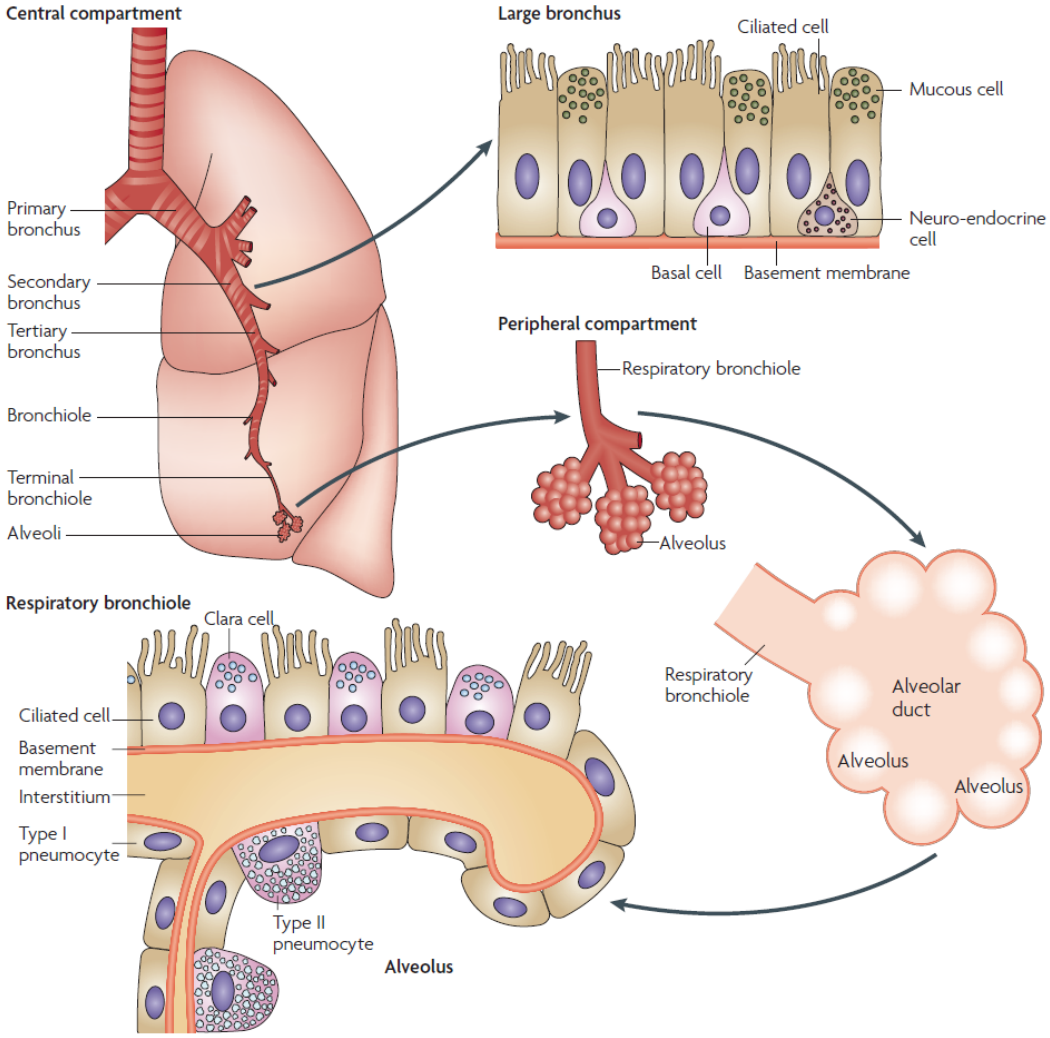

Figure 2: Lung compartments and cell types. Sun S. *et al*. Nat Rev Cancer 2007.

Pathologic staging

The standard of care for patients diagnosed with NSCLC depends on the extent of the disease. TNM staging is the main classification system and allows stratifying patients into prognostic groups. In this model, the anatomical extent of the cancer is assessed by examining the primary tumor (T), lymph nodes (N) and the presence of distant metastasis (M) (Figure 3).

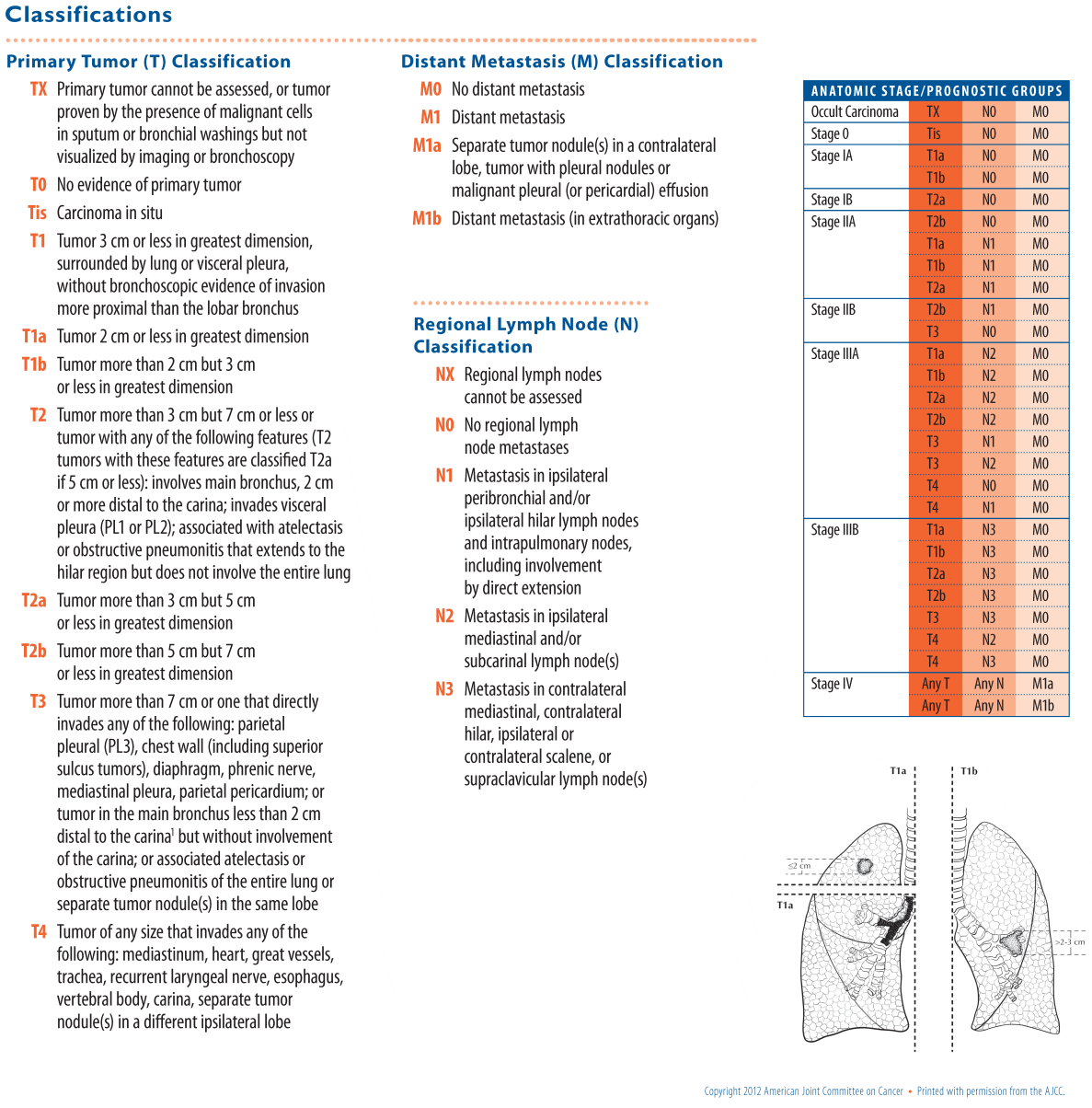

Classifications

Primary Tumor (T) Classification

- **TX** Primary tumor cannot be assessed, or tumor proven by the presence of malignant cells in sputum or bronchial washings but not visualized by imaging or bronchoscopy
- **T0** No evidence of primary tumor
- **Tis** Carcinoma in situ
- **T1** Tumor 3 cm or less in greatest dimension, surrounded by lung or visceral pleura, without bronchoscopic evidence of invasion more proximal than the lobar bronchus
- **T1a** Tumor 2 cm or less in greatest dimension
- **T1b** Tumor more than 2 cm but 3 cm or less in greatest dimension
- **T2** Tumor more than 3 cm but 7 cm or less or tumor with any of the following features (T2 tumors with these features are classified T2a if 5 cm or less): involves main bronchus, 2 cm or more distal to the carina; invades visceral pleura (PL1 or PL2); associated with atelectasis or obstructive pneumonitis that extends to the hilar region but does not involve the entire lung
- **T2a** Tumor more than 3 cm but 5 cm or less in greatest dimension
- **T2b** Tumor more than 5 cm but 7 cm or less in greatest dimension
- **T3** Tumor more than 7 cm or one that directly invades any of the following: parietal pleural (PL3), chest wall (including superior sulcus tumors), diaphragm, phrenic nerve, mediastinal pleura, parietal pericardium; or tumor in the main bronchus less than 2 cm distal to the carina[1] but without involvement of the carina; or associated atelectasis or obstructive pneumonitis of the entire lung or separate tumor nodule(s) in the same lobe
- **T4** Tumor of any size that invades any of the following: mediastinum, heart, great vessels, trachea, recurrent laryngeal nerve, esophagus, vertebral body, carina, separate tumor nodule(s) in a different ipsilateral lobe

Distant Metastasis (M) Classification

- **M0** No distant metastasis
- **M1** Distant metastasis
- **M1a** Separate tumor nodule(s) in a contralateral lobe, tumor with pleural nodules or malignant pleural (or pericardial) effusion
- **M1b** Distant metastasis (in extrathoracic organs)

Regional Lymph Node (N) Classification

- **NX** Regional lymph nodes cannot be assessed
- **N0** No regional lymph node metastases
- **N1** Metastasis in ipsilateral peribronchial and/or ipsilateral hilar lymph nodes and intrapulmonary nodes, including involvement by direct extension
- **N2** Metastasis in ipsilateral mediastinal and/or subcarinal lymph node(s)
- **N3** Metastasis in contralateral mediastinal, contralateral hilar, ipsilateral or contralateral scalene, or supraclavicular lymph node(s)

ANATOMIC STAGE/PROGNOSTIC GROUPS			
Occult Carcinoma	TX	N0	M0
Stage 0	Tis	N0	M0
Stage IA	T1a	N0	M0
	T1b	N0	M0
Stage IB	T2a	N0	M0
Stage IIA	T2b	N0	M0
	T1a	N1	M0
	T1b	N1	M0
	T2a	N1	M0
Stage IIB	T2b	N1	M0
	T3	N0	M0
Stage IIIA	T1a	N2	M0
	T1b	N2	M0
	T2a	N2	M0
	T2b	N2	M0
	T3	N1	M0
	T3	N2	M0
	T4	N0	M0
	T4	N1	M0
Stage IIIB	T1a	N3	M0
	T1b	N3	M0
	T2a	N3	M0
	T2b	N3	M0
	T3	N3	M0
	T4	N2	M0
	T4	N3	M0
Stage IV	Any T	Any N	M1a
	Any T	Any N	M1b

Figure 3: TNM classification of lung cancer. Adapted from https://cancerstaging.org/references-tools/quickreferences/Pages/default.aspx

Staging is primordial for adequate disease management since different treatment modalities are proposed according to the tumor stage. For early stages (I and II), surgical resection is the main treatment option and can in addition be followed by cisplatin-based adjuvant chemotherapy, notably for stages II-III NSCLC. For locally advanced NSCLC (stage III) or metastatic stage IV, disease management is individualized and require multimodal treatments (20). Neoadjuvant or induction chemotherapy can be performed in order to reduce the tumor burden before resection but this is so far not a standard treatment option.

Histopathologic subtyping

NSCLC is a heterogeneous disease including several histological subtypes. ADC and SCC are the two main histologic subtypes in addition to adeno-squamous or large cell neuroendocrine tumors. Histologically, ADC is characterized by the formation of glands often secreting mucin whereas SCC is recognized by the presence of keratin and/or intercellular desmosomes. Large cell carcinoma has no differentiating features (null phenotype) and is thus a poorly differentiated NSCLC. A panel of immunohistochemistry (IHC) stains is used to complete the diagnostic in case of doubts concerning the histological subtype. In practice, p40 and p63 serve as squamous markers and are therefore used to distinguish SCC whereas thyroid transcription factor (TTF-1) and mucin are the main markers for ADC (21). IHC cytokeratin cocktails such as AE1/AE3, which detects CK1-8, 10, 14-16 and 19, are also frequently used to rule out or confirm the epithelial nature of the cancer.

In addition, histologic subtyping is an important factor for treatment decisions. In clinical practice, different therapies are proposed to non-squamous NSCLC due to higher toxicity or reduced efficacy in SCC. As an example, the use of Pemetrexed, a chemotherapy drug and Bevacizumab, an antiangiogenic – anti vascular endothelial growth factor (VEGF) - antibody,

are restricted to non-squamous NSCLC (22-24). In addition, several recurrent genetic alterations are almost constantly constrained to a particular histology, e.g. EGFR mutations in adenocarcinoma.

Molecular subtyping

Molecular subtyping is a primordial component for personalized treatment. In addition to histologic subtyping, molecular testing is performed to detect the presence of specific mutations in order to tailor more personalized treatments (25). In fact, in NSCLC, the identification of recurrent genetic alterations in multiple oncogenes have led to therapeutic strategies notably with the approval of drugs specific to tumors harboring mutations in the epidermal growth factor receptor (EGFR) or rearrangements in the anaplastic lymphoma kinase (ALK) and the ROS1 gene. These genetic alterations are frequent in adenocarcinoma but are only rarely found in lung SCLC (Figure 4). EGFR mutations are observed in 10-35% of NSCLC but almost exclusively seen in adenocarcinoma. The detection of EGFR mutations is recommended being done by polymerase chain reaction (PCR). Tumors with specific EGFR mutations occurring within EGFR exons 18–21, located in the EGFR kinase domain, have an increased sensitivity to Receptor Tyrosine Kinase Inhibitors (RTKIs), such as Gefinitib (26, 27) and Erlotinib (28). ALK rearrangements lead in majority to the fusion of ALK gene with portions of the echinoderm microtubule-associated protein-like 4 (EML4) gene. They occur in 3-7% of NSCLC - predominantly in adenocarcinomas with acinar features- and are more often associated with young and light/non-smokers (29-34).

ROS1 rearrangements occur in 1% of NSCLC and similarly to ALK translocations, can be detected using immunohistochemistry (IHC), fluorescence in-situ testing (FISH) or by next-generation sequencing (NGS). NSCLC with ALK and ROS1 rearrangements can be currently be treated with Crizotinib, a potent dual ALK/MET tyrosine kinase inhibitor. Other potentially targetable genetic

alterations have been identified in NSCLC but have up to day no drugs approved for this type of cancer or are still under development. This includes mutations in KRAS (15-25%), PTEN (4-8%), BRAF (1-3%), HER2 (2-4%), DDR2 (~4%), MET (2-4%), PIK3CA (1-3%), AKT1 (1%), MEK1 (1%), NRAS (1%) as well as RET rearrangements (1%) and FGFR1 amplifications (20%) (35).

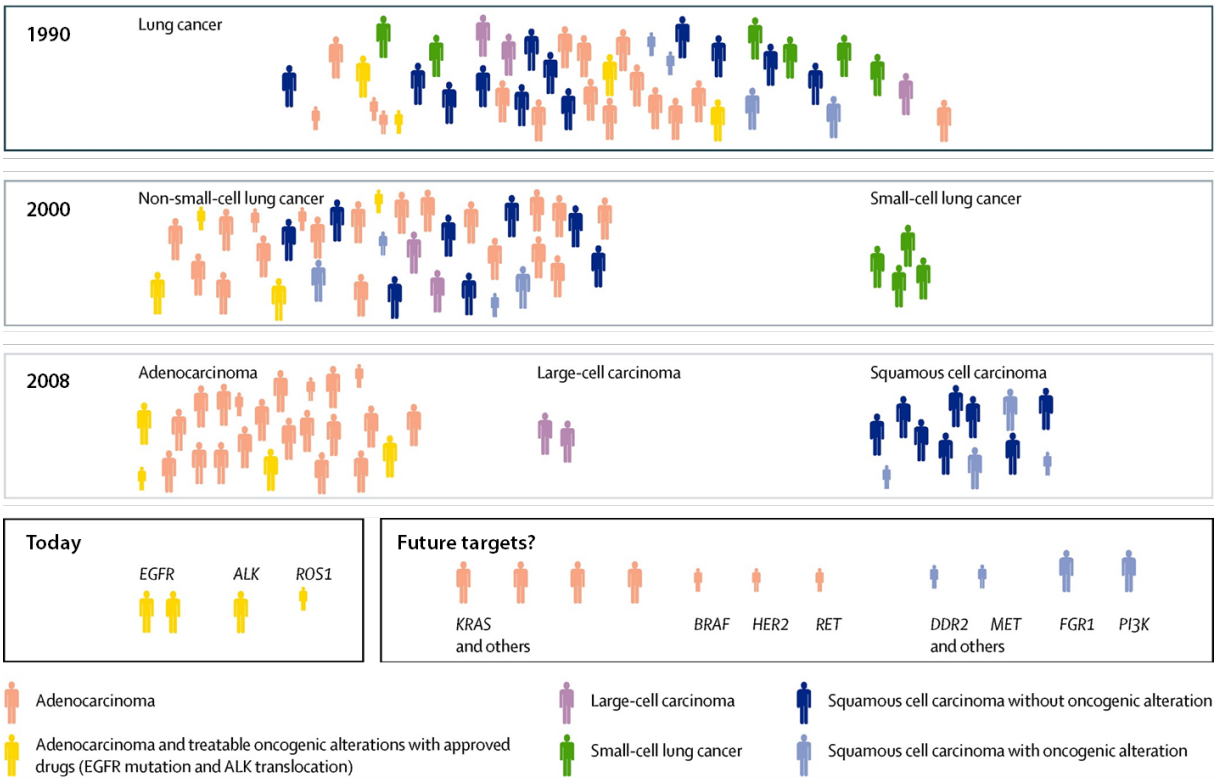

Figure 4: Evolution of lung cancer histology over time, adapted from Reck M. *et al.* Lancet 2013

Despite the presented efficacy of targeted therapies, the vast majority of patients experience cancer relapse due to acquired resistance of the tumor, which can be caused by gene alterations within the drug target, or activations of alternative oncogenic pathways (36, 37). An example of acquired resistance mechanism is the interference of the inhibitor with its EGFR binding domain, which is caused by the EGFR T790M mutation (38-40). This led to the development of inhibitors targeting EGFR T790M mutation such as Osimertinib, an FDA approved drug for metastatic NSCLC baring this specific mutation.

Alternatively, cancer immunotherapy is a promising strategy whose aim is to tackle immune evasion, a hallmark of cancer (41). Immunologic checkpoint blockade - using antibodies targeting the programmed cell death protein 1 pathway (PD-1/PD-L1) - is a promising treatment strategy for NSCLC. PD-1 and PD-L1/PD-L2 are immune checkpoint proteins acting as co-inhibitory factors. While PD-1 is expressed in activated T cells whereas, PD-L1 and PD-L2 are commonly expressed on the surface of macrophages and dendritic cells. However, tumor cells may also express PD-L1 leading to the inhibition of T-cell response (42, 43). There are numerous ongoing phase III clinical trials based on immune checkpoints blockade using antibodies against PD1 (Nivolumab, Pembrolizumab) and PD-L1 (Atezolizumab, Durvalumab). Several clinical trials have shown the efficacy of anti PD-1 immunotherapy and most recently, Pembrolizumab combined with carboplatin and Pemetrexed chemotherapy has been approved by the Food and Drugs Administration (FDA) as first line treatment of non-squamous NSCLC (44-46).

Morphologic subtyping for NSCLC grading

In addition to staging, tumor grading aims at further stratifying tumors into prognostic groups, according to morphologic criteria. Despite ongoing efforts in this field, there are currently no established grading criteria for NSCLC (21). Nevertheless, as proposed by the International Association for the Study of Lung Cancer (IASLC)/the American Thoracic Society (ATS)/the European Respiratory Society (ERS), adenocarcinoma can present five distinct morphologic subtypes: lepidic, acinar, papillary, micropapillary and solid (figure 5) (47). The determination of the predominant pattern has been shown to be prognostic and has been suggested as grading parameter (48-52).

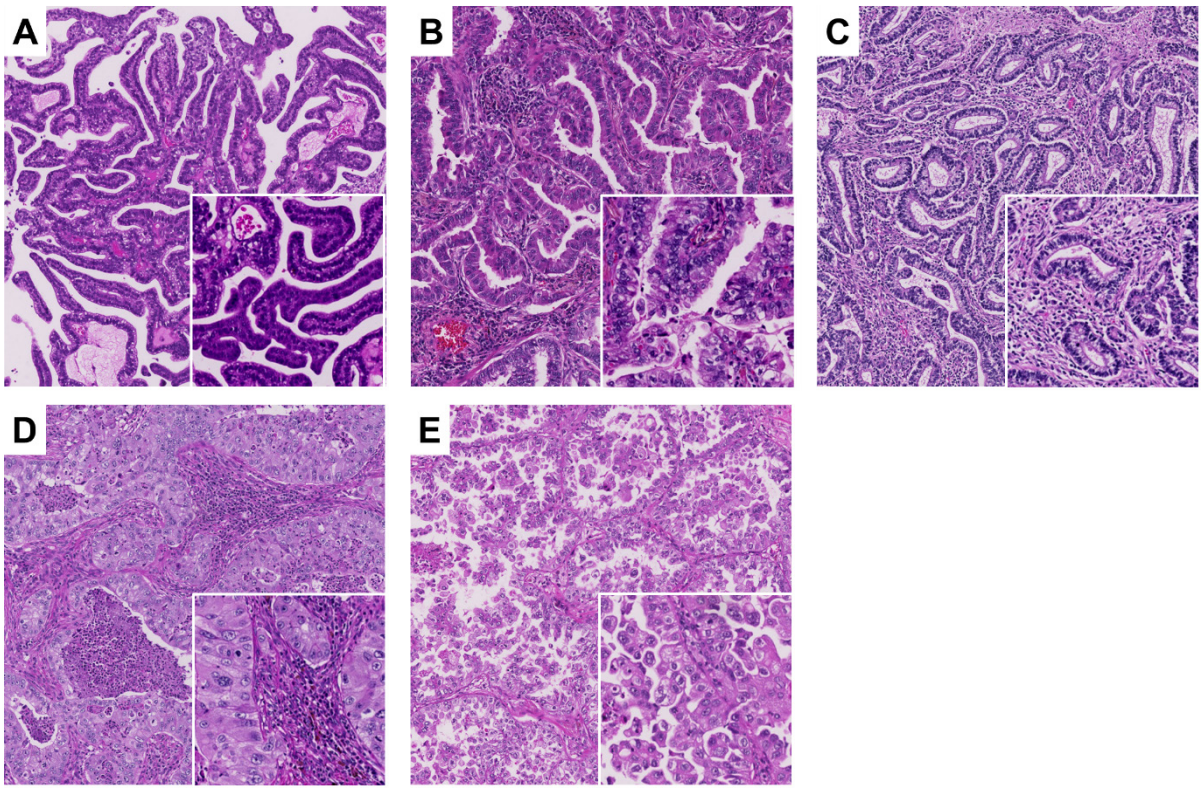

Figure 5: Hematoxylin and Eosin (H&E) stained histologic sections magnified 25x (square 80x) showing the main morphologic subtypes for adenocarcinoma. A) lepidic, B) papillary, C) acinar, D) solid, E) micro-papillary patterns. *Unpublished data.*

The presence of keratinization is the main feature of lung SCC and defines the degree of differentiation. Prominent keratinization is associated with well-differentiated SCC while poorly differentiated tumors have only focal or non-apparent keratinization. Basaloid SCC is a form of poorly differentiated squamous cell carcinoma, morphologically described by smaller cells forming lobular structures with peripheral palisading (figure 6). However, the prognostic value of this parameter remains unclear. Other prognostic parameters such as tumor budding, single cell invasion, stromal thickness have been suggested as grading parameters but are currently not in use in routine pathology (53-56).

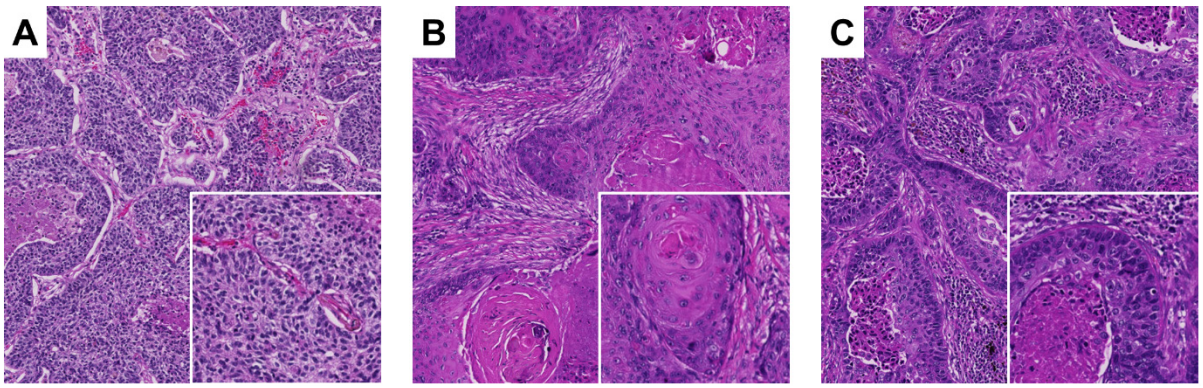

Figure 6: H&E stained histologic sections magnified 25x (square 80x) showing the main morphologic subtypes of lung squamous cell carcinoma. A) poorly differentiated/non-keratinizing, B) well differentiated/keratinizing, C) basaloid. *Unpublished data.*

Digital pathology as a tool for quantitative tumor morphologic analysis

Digital pathology is an emerging field aiming at improving tissue diagnostic by computerized approaches. With the development of high-resolution scanners allowing to scan whole tissue samples at 40x magnification and higher, it has been shown that digitalization of tumor tissue does not affect the diagnostic power in pathology (57). The most common applications include chromogenic immunohistochemistry (IHC) or immunofluorescence (IF) staining quantification as well as morphologic features extraction and quantification (58).

In the setting of routine pathology, Hematoxylin and Eosin (H&E) is the standard histochemical staining to evaluate histological morphology. Protein expression is routinely evaluated by IHC and chromogenic IHC is preferred over IF because the stained section can be preserved over decades and evaluated by bright field microscopy. Automated IHC analysis can be used for biomarker measurement (59), and has proven to yield to similar results from expert pathologists (60). While the human eye is highly efficient in recognizing patterns, the quantification of morphologic features is more challenging. In their routine, pathologists assess the histologic grade of the tumor in order to inform about the tumor aggressiveness, which is directly related to patient's prognosis. However, they are limited to a semi-quantitative scheme

to grade the disease. Computerized histological image analysis has demonstrated the ability to stratify tumors into prognostic groups using machine-learning algorithms on morphologic parameters extracted from tumor and surrounding cells (61-63). It has also shown to be efficient in detecting tumor metastases on whole histologic slides (64). Due to the tremendous image availability and because H&E discriminates nuclear and subcellular features, the vast majority of studies rely on this staining. While these methods focus on subcellular features, accurate quantification of higher-level structural features of the tumor epithelia and surrounding stroma is more challenging. A straightforward color-based segmentation approach can be achieved using chromogenic IHC, with antibodies specific to epithelial structures (65, 66). Furthermore, it has been shown that cytokeratin staining improves the pathologic evaluation of spread tumor buds (67, 68). As depicted above, current efforts lay on the development of diagnostic companions for pathologists in order to improve efficiency, accuracy and consistency in histopathology evaluations (69).

Aims

The aim of this doctoral study was to develop a computerized approach to support the pathologic evaluation of tumor tissue, in particular lung squamous cell carcinoma. An IHC-based method - using AE1/AE3 antibodies - was used to stain specifically tumor epithelia, to extract features related to the tumor microarchitecture.

In Chapter 2, the main objective was to quantify histologic prognostic markers, which are able to stratify patients into risk groups, based on tumor morphology. For this purpose, we addressed the prognostic relevance of tumor fragmentation (TF), a hypothetical histologic marker of increased invasiveness, using two cohorts of LSCC patients. Additionally, we included an external cohort of LSCC patients in order to test the prognostic value of a human-based TF scoring system using standard H&E sections. Finally, molecular data was integrated to our morphometric analysis was in order to characterize the biological processes associated to high TF.

In Chapter 3, we applied a similar morphometric analysis to characterize morphological changes after neoadjuvant chemotherapy. The objective of this project was to provide a quantitative tumor regression model, which could be used to refine current pathologic response after chemotherapy. For this purpose, a cohort of neoadjuvant chemotherapy treated LSCC cohort was compared to a chemo-naïve cohort. Four morphologic parameters related to the size and extension of the remaining tumor burden were evaluated. The performances of human-based scores for tumor regression were compared with the generated morphometric data. Additionally, we integrated FDG PET/CT parameters in order to correlate the tumor metabolic activity - before and after chemotherapy - with quantitative histologic features.

In Chapter 4 an initial study, evaluating the performances of several FDG PET/CT measurements in discriminating histopathologic response for NSCLC, is presented. The aim of this study was to identify which metabolic values - among the most common measurements – correlated best with pathologic tumor regression, assessed by conventional light microscopy.

Chapter 2

Morpho-proteomics characterization of lung squamous cell carcinoma fragmentation, a histological marker of increased tumor invasiveness

Cancer Research, published on May 15, 2017
doi: 10.1158/0008-5472.CAN-16-2363

Ruben Casanova[1], Daniel Xia[2,3], Undine Rulle[1], Paolo Nanni[4], Jonas Grossmann[4], Bart Vrugt[1], Reto Wettstein[5], Rafael Ballester[5], Alberto Astolfo[6], Walter Weder[7], Holger Moch[1], Marco Stampanoni[6,8], Andrew H. Beck[9], Alex Soltermann[1]

1. *Institute of Pathology and Molecular Pathology, University Hospital Zurich, Zurich, Switzerland*
2. *Department of Pathology, Massachusetts General Hospital, Boston, MA, USA*
3. *Department of Pathology, Brigham and Women's Hospital, Boston, MA, USA*
4. *Functional Genomics Center Zurich, University/ETH Zurich, Zurich, Switzerland*
5. *Department of Informatics, University of Zurich, Zurich, Switzerland*
6. *TOMCAT Beamline, Swiss Light Source, Paul Scherrer Institute, Villigen, Switzerland*
7. *Division of Thoracic Surgery, University Hospital Zurich, Zurich, Switzerland*
8. *Institute for Biomedical Engineering, University/ETH Zurich, Zurich, Switzerland*
9. *Department of Pathology, Beth Israel Deaconess Medical Center and Harvard Medical School Boston, MA, USA*

Running title

Morpho-proteomics of lung squamous cell carcinoma

Keywords

Lung, squamous cell carcinoma, digital pathology, prognosis, label-free mass spectrometry

Financial support

This work was supported by grants from the Swiss Cancer League (reference number F-87701-31-01) and the Swiss National Science Foundation SystemsX (reference number M-87704-01-02) to A. Soltermann.

Corresponding author

Ruben Casanova, Institute of Pathology and Molecular Pathology, University Hospital Zurich, Schmelzbergstrasse 12, CH-8091 Zurich, Switzerland. Tel: +41 44 255 29 21; ruben.casanova@usz.ch

Conflict of interest

The authors declare to have no competing financial interest

Own contribution

Conception and design, development of methodology, acquisition of data, analysis and interpretation of data, writing, review and revision of the manuscript.

Abstract

Accurate stratification of tumors is an imperative step for adequate cancer management. In addition to staging, morphological subtyping allows stratifying patients into additional prognostic groups. In this study, we used an image-based computational method on pan-cytokeratin immunohistochemical (IHC) stainings to quantify tumor fragmentation (TF), a measure of tumor invasiveness of lung squamous cell carcinoma (LSCC). We showed on two independent clinical cohorts from tissue microarrays (TMA: n=208 patients) and whole sections (WS: n=99 patients) that this novel parameter was associated with poor prognosis and increased risk of blood vessel infiltration. The poor prognostic value of increasing TF was further confirmed in a third cohort from the cancer genome atlas (TCGA: n=335 patients) using a similar human-based score on haematoxylin-eosin (H&E) histochemical stainings. The integration of mRNAseq data from TCGA, and LC-MS/MS proteomics from WS, revealed an up-regulation of extracellular matrix remodeling and focal adhesion processes in tumors with high TF, supporting their increased invasive potential. The proposed histologic parameter is an independent unfavorable prognostic marker that could be envisaged as new grading parameter for LSCC.

Introduction

Lung squamous cell carcinoma (LSCC) is the second most frequent histological subtype of non-small cell lung carcinoma (NSCLC), accounting for 25-30% of all lung cancers in Europe (11). According to the 2015 WHO classification, LSCCs are further separated into keratinizing and non-keratinizing subtypes. However, the prognostic relevance of this subtyping remains unclear (53, 54). Stratification of lung cancers is an imperative step for adequate disease management and is primarily achieved by TNM staging (primary tumor extent, lymph nodes status and distant metastases). In addition, tumor grading based on morphological parameters such as overall architecture or cell and nuclear pleomorphism also allows stratifying patients into prognostic groups. However, there is still no well-established grading system for LSCC (21). Tumor invasion is supported by *de novo* formation of desmoplastic stroma, which provides not only physical support to cancer cells but also favors tumor expansion and invasion as a net effect of tumor-stroma inter-talk (41). LSCC invasion is histologically characterized by tumor clusters of variable sizes surrounded by such specialized stroma. This is reflected by an apparent fragmentation of both central and peripheral portions of the tumor mass. The quantification of such tumor fragments on whole histological sections may be used as a metric for tumor aggressiveness which could serve as a novel grading parameter to stratify LSCC into prognostic groups.

In this study, we performed an image-based computational analysis for unbiased tumor fragmentation (TF) quantification and applied extended the method with a human-based scoring system relevant for pathologists. Additionally, we integrated tumor histology with molecular data to evaluate the biological processes associated to this morphological feature. A retrospective study on three independent clinical cohorts was performed to assess the potential prognostic relevance of TF as novel grading parameter for LSCC.

Materials and Methods

Patient cohorts

In this retrospective study, consecutive patients with surgical resection of their primary lung SCC at the University Hospital Zurich were selected. Squamous cell differentiation was reviewed on haematoxylin-eosin (H&E) and alcian blue-periodic acid schiff (AB-PAS) stains. Differential diagnosis of non-keratinizing SCC versus solid adeno-, null-phenotype or neuroendocrine large cell carcinoma was performed by respective IHC using TTF1, p40, p63, CK7 and synaptophysin antibodies. Cases with mixed or unclear histology were excluded. Patients with synchronic or metachronic second primary tumor in particular head and neck SCC, with neo-adjuvant chemo-/radiotherapy or with overall survival (OS) < 1 month post-surgery were also excluded. The TMA cohort consisted of 233 lung SCC patients between January 1993 and December 2002, as described (70). Patients were further excluded if the quality of the pan-cytokeratin IHC was insufficient for automatic image analysis on both cores, e.g. due to presence of non-cancerous tissue, more than 80% stroma or major cutting artefacts. In total 208 patients met inclusion criteria. Adjuvant treatment was administered to 75 (36%) patients from which 62 (82%) received radiotherapy, 8 (11%) chemotherapy and 5 (7%) both. The WS cohort consisted of non-redundant 167 patients between January 2003 and February 2010 having complete clinical data. After revision for exclusion criteria, 99 patients were included. Adjuvant therapy was administered to 30 (30%) of the patients from which 6 (20%) received radiotherapy, 20 (67%) chemotherapy and 4 (13%) both. TCGA clinical data was downloaded from cBioPortal for Cancer Genomics, Memorian Sloan Kettering Cancer Center (71) for 504 lung SCC patients. After exclusion due to OS<1 month, neo-adjuvant chemotherapy or insufficient image quality, 335 patients remained. Thirty-one (9%) patients had a documented adjuvant therapy whereby 3 (10%) received radiotherapy, 21 (68%) targeted therapy and 7 (22%) both. Our study was

approved by the Ethical Commission of the Canton of Zurich under reference number KEK ZH-Nr. 29-2009/14.

Tissue microarray construction and immunohistochemistry

For the TMA cohort, two representative paraffin blocks with tumor were selected. One tissue core of 600µm diameter was taken from each tissue block and transferred into a recipient block. For the whole sections cohort, two blocks representing best the overall tumor morphology were selected and 2µm thick sections were cut from each block. Immunohistochemistry (IHC) was performed on an automated platform (Ventana Medical Systems, Tucson, AZ, USA) using mouse monoclonal anti-human cytokeratin AE1/AE3 (M3515, DAKO, dilution 1:50), rabbit polyclonal Periostin (Abcam, 1:1000) and mouse monoclonal Versican (2B1, Seikagaku, 1:500). Detection was completed with a respective secondary antibody and the OptiView DAB kit (Ventana Medical Systems).

Image acquisition

Immunohistochemically stained sections were scanned with a high-resolution whole slide scanner (Nanozoomer Digital Pathology, Hamamatsu, Japan) using a 40x objective with spatial resolution of 0.23µm/pixel. TMA and whole sections images were analyzed with a spatial resolution of 1.84µm/pixel and 9.2µm/pixel, respectively. Whole sections were further annotated by a surgical pathologist (A.S.) in order to select tumor tissue. The surrounding non-tumor lung tissue was excluded from the analysis. A formalin-fixed cylindrical tissue sample of 1 cm diameter from a pT3 lung SCC was imaged by X-ray microtomography at the beamline for tomographic microscopy and coherent radiology experiments (TOMCAT), Paul Scherrer Institute (PSI, Würenlingen, Switzerland). Sample was scanned using a microscope equipped with a PCO-Edge camera mounted with a 10x objective for a spatial resolution of 0.65µm /pixel using propagation-based X-ray phase contrast CT, as described (72).

Image processing

Automatic morphometric analysis was performed using FIJI (73). Color-based segmentation allowed separating the tumor tissue (brown) from its surrounding stroma (blue/grey). Color threshold values were previously validated by the pathologist. A similar approach for tumor segmentation by cytokeratin stained sections has been described for colon carcinoma (65). The segmentation algorithm included mean shift and median filtering, color thresholding using the *L*a*b* color space and particle size filtering with a minimum size threshold of 100µm^2, considered as noise. The resulting segmentation masks were used for automated scoring of tumor fragmentation.

Tumor fragmentation scoring

Tumor fragments refer to tumor clusters completely separated from each other on a two-dimensional plane by intervening desmoplastic stroma. Tumor fragmentation was automatically scored on the pan-CK stainings of both TMA and WS by counting the total number of disconnected particles larger than 800µm^2 (circa ≥ 5 cells) for each segmentation mask. TF scores were summed up over two images when available or duplicated for cases with single images. In addition, 88/99 WS patients were also represented on a secondary TMA from which 77 had sufficient image quality for automated TF scoring. TF scores from this subset were used to address scoring heterogeneity between TMA cores and whole sections for the same tumor. Human-based TF scoring was done by one observer (obs1) on H&E stained tissues. On TMA cores, TF was scored using all available magnifications and on the area of highest fragmentation for the TCGA and WS cohorts, under a magnification of 50x. This corresponded to 1920x1036 pixels (3.5x1.9mm) for TCGA image frames and to 4mm FOV for WS with light microscopy. Two additional observers (obs2-3) evaluated 20% of the TCGA images (n=67) to address inter-observer variability.

Sample preparation for mass spectrometry

A total of 48 samples from the whole sections cohort were selected for mass spectrometry based on the availability of at least 1 tumor paraffin block containing >80% carcinoma epithelia per total tissue surface. Two 20µm thick microtome cuts were deparaffinized in xylene and washed with 96% ethanol. Samples were suspended in 120µl of SDS buffer (4% SDS, 100mM Tris / HCL pH 8.2, 0.1M DTT – dithiothreitol) and boiled at 95°C for 20 minutes followed by 2h at 80°C and processed with High Intensity Focused Ultrasound (HIFU) for 10 min, setting the ultrasonic amplitude to 65%. Protein concentration was determined using the Qubit® Protein Assay Kit (Life Technologies, Zurich, Switzerland). For each sample, 20µg protein were taken for on-filter digestion using an adaptation of the filter-aided sample preparation (FASP) protocol (74). Briefly, proteins were diluted in 200µl of UT buffer (Urea 8M in 100mM Tris/HCL pH 8.2), loaded on Ultracel 30000 MWCO centrifugal unit (Amicon Ultra, Merck, Darmstadt, Germany) and centrifuged at 14000g. SDS buffer was exchanged by one centrifugation round of 200µl UT buffer. Alkylation of reduced proteins was carried out by 5 min incubation with 100µl iodoacetamide 0.05M in UT buffer, followed by three 100µl washing steps with UT and three 100µl washing steps with NaCl 0.5M. Finally, proteins were on-filter digested using 120µl of 0.05 triethylammonium bicarbonate buffer (pH 8) containing trypsin (Promega, Madison, WI, USA) in ratio 1:50 (w/w). Digestion was performed overnight in a wet chamber at room temperature. After elution, the solution containing peptides was acidified to a final 0.1% TFA, 3% acetonitirile concentration. Peptides were desalted using self-packed C18 Stage-Tips, dried and re-solubilized in 15µl of 3% acetonitrile, 0.1% formic acid for MS analysis.

Liquid chromatography-mass spectrometry analysis

Mass spectrometry analysis was performed on an Orbitrap Fusion mass spectrometer (Thermo Fisher Scientific, Waltham, MA, USA) coupled to an Eksigent-Nano-HPLC system (Sciex,

Framingham, MA, USA). Solvent composition at the two channels was 0.1% formic acid for channel A and 0.1% formic acid, 99.9% acetonitrile for channel B. For each sample 2µL of peptides were loaded on a self-made column (75µm × 150mm) packed with reverse-phase C18 material (ReproSil-Pur 120 C18-AQ, 1.9µm, Dr. Maisch GmbH, Ammerbuch, Germany) and eluted at a flow rate of 300nL/min by a gradient from 3 to 25% B in 65 min, 35% B in 5 min and 97% B in 5 min. Samples were acquired in a randomized order. The mass spectrometer (Tune page v1.1) was configured to fragment peptide precursor ions in data-dependent mode, allowing a maximum of 3 s between the full-scan spectra (top speed mode). Full-scan MS spectra (300–1500 m/z) were acquired at a resolution of 120000 at 200 m/z after accumulation to an automated gain control (AGC) target value of 400000. Wide quadrupole isolation was used, and an injection time of 50ms was set. Precursors with an intensity above 5000 were selected for MS/MS. Ions were isolated using a quadrupole mass filter with 1.6 m/z isolation window and fragmented by higher-energy collisional dissociation (HCD) using a normalized collision energy of 30. Fragments were detected in the linear ion trap using adapted "Universal Method" settings: the scan rate was set to Rapid, the automatic gain control was set to 100 ions and the maximum injection time was 250 milliseconds. Charge state screening was enabled and singly and unassigned charge states were rejected. Precursor masses previously selected for MS/MS measurement were excluded from further selection for 25 seconds, and the exclusion window was set at 10 ppm. The samples were acquired using internal lock mass calibration on m/z 371.1010 and 445.1200.

Protein identification and label free protein quantification

Protein label-free quantification was performed using the software Progenesis QI for proteomics (v.4.0.4265.42984) software (Nonlinear Dynamics, Newcastle upon Tyne, UK), using as reference for alignment the raw-file of the pool sample. Normalization was kept with default

settings. From each Progenesis peptide ion (default sensitivity in peak picking) a maximum of the top five tandem mass spectra were exported into a Mascot generic file using charge deconvolution and deisotoping option and a maximum number of 200 peaks per MS/MS. This Mascot generic file (mgf) was searched with Mascot 2.4.3.3 (Matrix Science Ltd., London, UK) against the forward Uniprot database for *Homo sapiens*, concatenated to a reversed decoyed FASTA database and 260 common mass spectrometry protein contaminants. The parameters for precursor tolerance and fragment ion tolerance were set to ± 10 ppm and ± 0.6 Da. Enzyme was set to trypsin and one missed cleavage was allowed. Carbamidomethylation of cysteine was set as fixed modification, while oxidation (M) and deamidation (N, Q) were set as variable. The resulting .dat file was loaded into Scaffold v4.1.1 (Proteome Software) and filtered at peptide and protein False Discovery Rates (FDRs) were set to 1% and 9%, respectively. Finally, the Scaffold Spectrum Report was imported back into Progenesis. For quantification, all proteins identified with at least two peptide ions were assessed, resulting in an estimated protein FDR of 0.5%. Proteins were grouped with Progenesis and the relative quantification using Hi-N (N=3) peptides was used. For protein quantification, the average of the normalized abundance from the most intense N peptide ions of each protein group was calculated individually for each sample. This generated the normalized quantitative protein abundance. Protein levels were further log2 transformed for statistical testing. Differentially expressed proteins were identified by Significance Analysis of Microarrays as described (75). TF scores were log2 transformed and addressed as quantitative response using the standard regression method on median centered protein levels. Proteins significantly correlated with TF scores (FDR<0.05) were considered for further analysis. Gene ontology enrichment analysis was performed using WEB-based GEne SeT AnaLysis Toolkit (76) using default settings. All identified proteins (n=2614) were used as background (see original article).

Gene ontology enrichment networks and pathway analysis for TCGA mRNAseq data

Analysis-ready standardized TCGA mRNA-Seq data was downloaded from the Broad GDAC Firehose stddata__2015_11_01 run. Two groups showing clearly distinguishable TF profiles on TCGA H&E stainings, consisting of patients with the 25% lowest (TF <6) and 25% highest (TF >18) scores were selected for mRNA differential expression analysis. For statistical testing, the R-package EdgeR was used to compare them. In total mRNAseq data for 20531 genes was available. Genes with a minimum of 1 count-per-million, in at least half of the samples, were selected (n=14151). Default parameter settings were applied. Candidates having a FDR <0.05 were included in the gene ontology enrichment analysis. Gene ontology enrichment map was generated with the software Cytoscape (77) using BINGO (78) and Enrichment Map (79) plugins. Genes upregulated in high and low TF tumors, respectively, were uploaded separately in BINGO. Enrichment analysis was performed with the default hypergeometric test using a significance level <0.05 after Bonferroni correction for multiple testing. Enrichment map was generated using BINGO outputs for each tumor morphotype with the following parameter: p-value cutoff <0.001, FDR <0.05, Jaccard coefficient=0.25. The generated network is represented by nodes (gene sets), edges (mutual overlap) and colors (tumor morphology groups: blue=low TF, red=high TF). Pathway analysis was done using the KEGG database (80) through WEB-based GEne SeT AnaLysis Toolkit.

Data interpretation and statistical analysis

All statistical analyses were performed on SPSS version 22 software (SPSS Inc., Chicago, USA). Relapse-free survival was measured from the date of surgery to the date of documented relapse or death as described (81). RFS was assessed only for patients who presented no evidence of remaining tumor (incomplete resection and/or metastases) after surgery. Kaplan Meier survival curves were evaluated using log-rank tests using TF scores dichotomized at the

median. Hazard ratios were assessed by Cox regression. Clinical correlations were addressed using the non-parametric spearman's rank correlation test. The association of clinical parameters with survival was computed by univariate Cox regression. In addition, clinically relevant parameters were introduced into multivariate Cox regressions. P-values <0.05 were considered significant.

Results

LSCC shows a variable degree of tumor fragmentation

Tumor fragmentation (TF) scores were automatically computed as the total number of tumor fragments in pan-cytokeratin stained TMAs of 208 LSCC patients and whole sections (WS) of 99 patients (Table 1). The size of tumor fragments within individual tumors varied considerably (Figure 1A). By using X-ray microtomography we saw that tumor fragments represent projections of interconnected epithelial branches from a three dimensional perspective (Figure 1B). The distribution of the computed TF scores was comparable in the TMA and WS cohorts (Figure S1A-B left). The assessment of a subset of 77 patients from WS with matching TMA cores from a secondary TMA, showed a positive correlation of TF scores between whole sections and tumor cores from the same tumor (c.coeff=0.484, p<0.001). However, due to intra-tumor heterogeneity the WS analysis allows a more reliable assessment of TF scores as demonstrated by the correlation analysis of computed TF scores from two tumor regions (Figure S1A-B right). We further tested the applicability of TF scoring by human eye using H&E stained images of the TMA and WS cohorts, as well as in an external TCGA LSCC cohort with similar clinical characteristics. The distribution of TF scores was comparable between the computed and human-based evaluations (Figure S1C-E). Histological examples of tumors with high and low fragmentation from TMA, WS and TCGA cohorts are shown in Figure 2.

Table 1: Patient cohorts. Summary of clinico-pathologic parameters including OS and RFS for TMA, WS and TCGA datasets. CI=95% confidence interval; TF computer/human=tumor fragmentation scores respectively computed or assessed by eye.

Patient cohorts	TMA		WS		TCGA	
Age						
median (range)	66	(18 - 87)	65	(40 - 87)	68	(39-90)
Sex						
female	42	(20%)	19	(19%)	83	(25%)
male	166	(80%)	80	(81%)	252	(75%)
pT						
1	43	(21%)	24	(24%)	68	(20%)
2	107	(51%)	29	(29%)	213	(64%)
3	43	(21%)	34	(35%)	40	(12%)
4	15	(7%)	12	(12%)	14	(4%)
pN						
0	110	(53%)	47	(48%)	209	(63%)
1	73	(35%)	31	(31%)	88	(27%)
2 - 3	25	(12%)	21	(21%)	35	(10%)
pM						
0	196	(94%)	95	(96%)	284	(98%)
1a/b	12	(6%)	4	(4%)	5	(2%)
Stage						
I	71	(34%)	24	(24%)	165	(49%)
II	76	(37%)	35	(35%)	108	(32%)
III	50	(24%)	36	(37%)	57	(17%)
IV	11	(5%)	4	(4%)	5	(2%)
Grade						
1 - 2	121	(58%)	44	(44%)	-	-
3	87	(42%)	55	(56%)	-	-
Size (cm)						
median (range)	3.9	(0.4 - 14.0)	5	(1.1 - 11.0)	-	-
Vessel infiltration						
absent	122	(59%)	52	(53%)	-	-
present	86	(41%)	47	(47%)	-	-
Adjuvant therapy						
no	133	(64%)	69	(70%)	304	(91%)
yes	75	(36%)	30	(30%)	31	(9%)
TF score						
Computer (IHC)						
median (range)	7	(2-38)	984	(163-6093)		
Human (H&E)						
median (range)	6	(2-40)	25	(2-132)	12	(1-68)
OS (months)						
median (CI)	42	(29 - 55)	52	(36 - 69)	56	(43-69)
follow-up max	169		137		157	
RFS (months)						
median (CI)	59	(40-78)	46	(27-65)	75	(45-105)
follow-up max	169		137		154	
Total patients (n=642)	**208**		**99**		**335**	

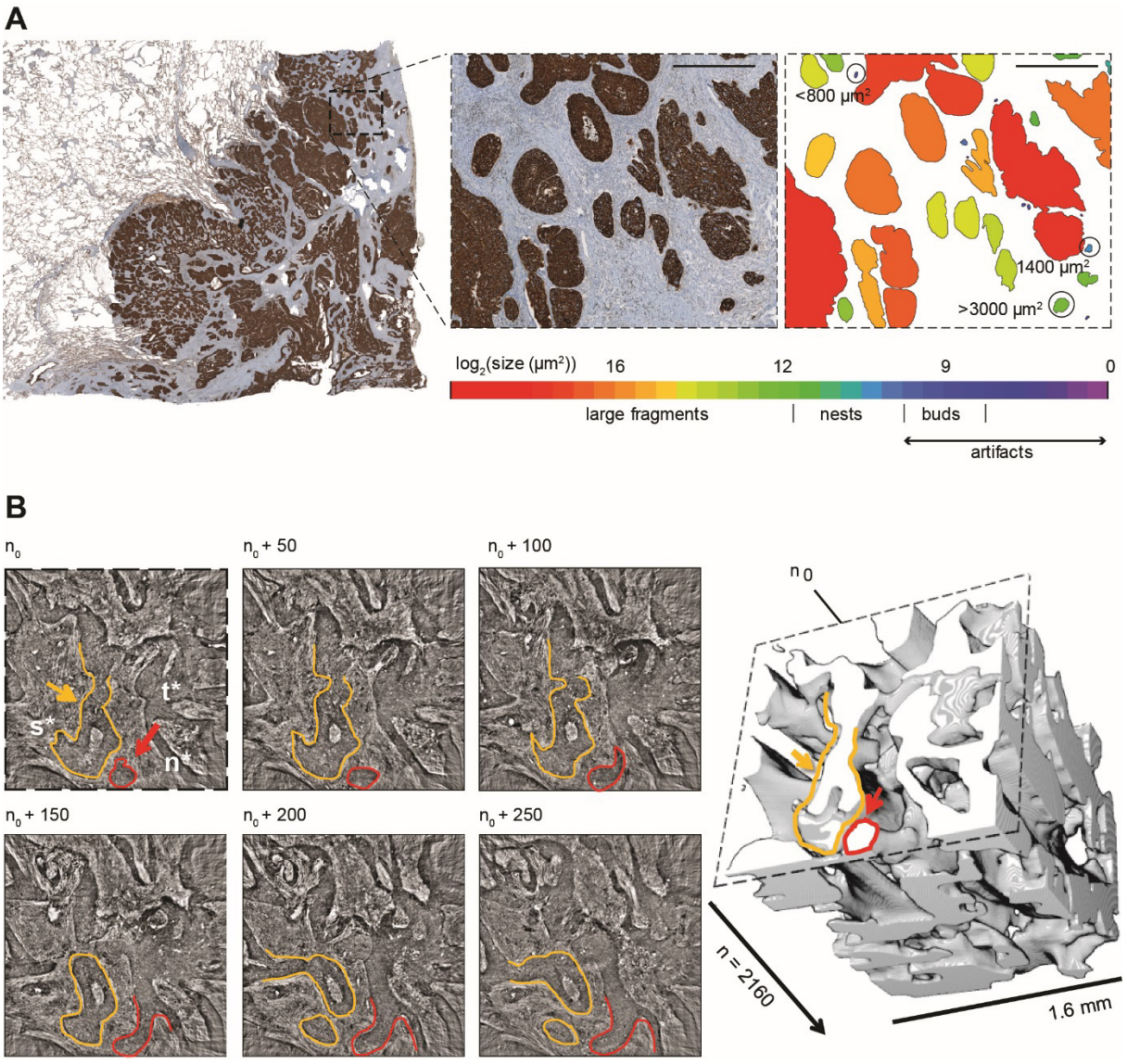

Figure 1: Computer-based morphometric analysis of tumor fragmentation. A) Left: histological whole section showing a squamous cell carcinoma of the lung stained with pan-cytokeratin IHC (brown) and its surrounding stroma (blue-grey counterstain). Right: color-based segmentation showing tumor fragments of different sizes labelled on a 32-colors scale. Approximate sizes are: single cell 200µm^2, buds ≤800µm^2, nests ≤3000µm^2, larger fragments >3000µm^2. Number of epithelial elements=32, size$_{mean}$=44'000µm^2, size$_{median}$=14'000µm^2. Scale bar: 500µm. B). Left: X-ray microtomography 2D reconstructed slice of a lung SCC example. Arrows indicate epithelial tumor fragments, t*=tumor, n*=necrosis, s*=stroma. Right: 3D rendering of the tumor microarchitecture imaged by X-ray microtomography.

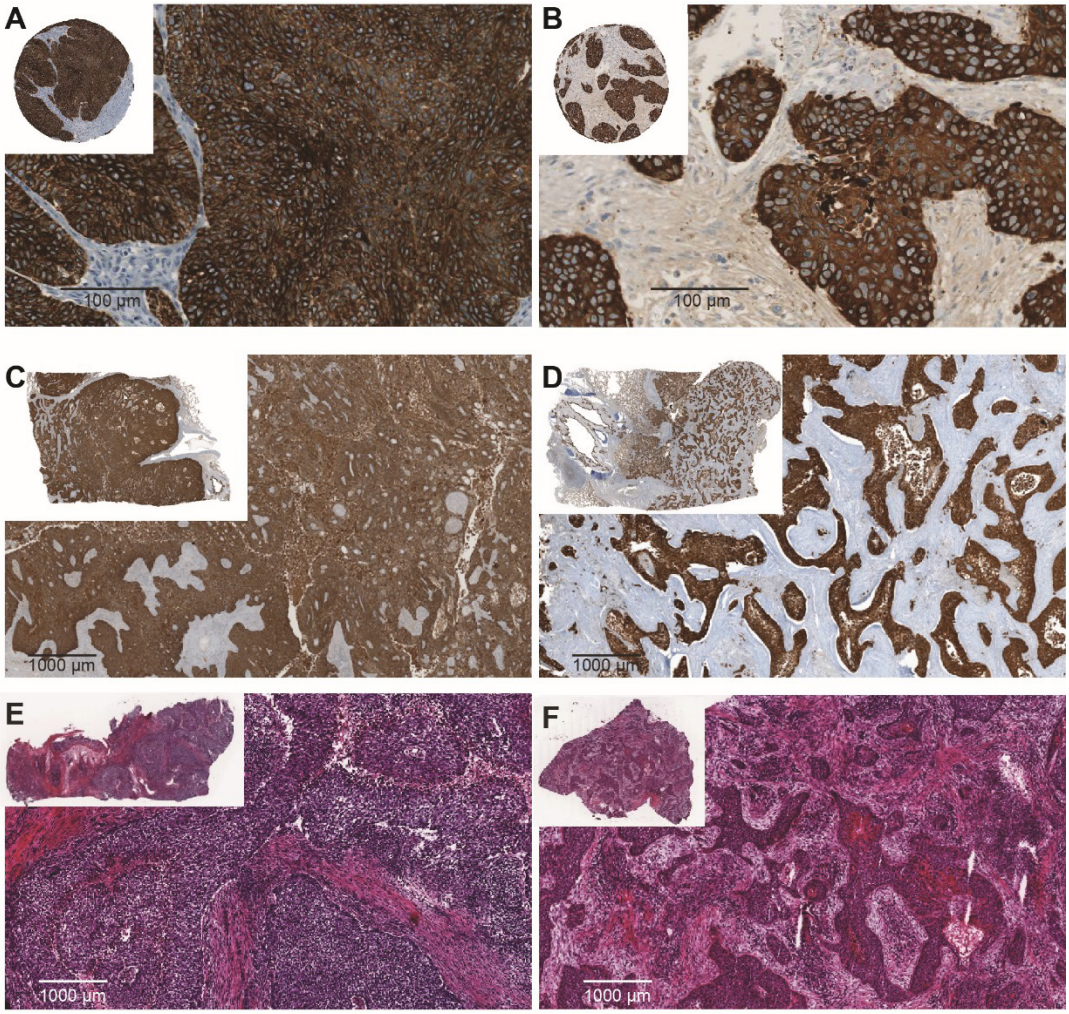

Figure 2: Lung squamous cell carcinoma microarchitecture and fragmentation. Histological examples of pan-cytokeratin stained sections from TMA (A-B) and WS (C-D) cohorts. E-F) H&E stained sections from TCGA. Left/right: low/high fragmentation.

Tumor fragmentation is associated with increased invasiveness and worse outcome

Clinico-pathologic correlations showed that high TF was consistently associated with vessel infiltration on both TMA and WS (Table S2). Perineural and mediastinal invasion were further evaluated on WS and positively correlated with TF as well (p=0.001, p=0.004 respectively). Survival analysis showed that high TF is a poor prognostic factor for OS and was confirmed using the external TCGA cohort with human-based scores (Figure 3).

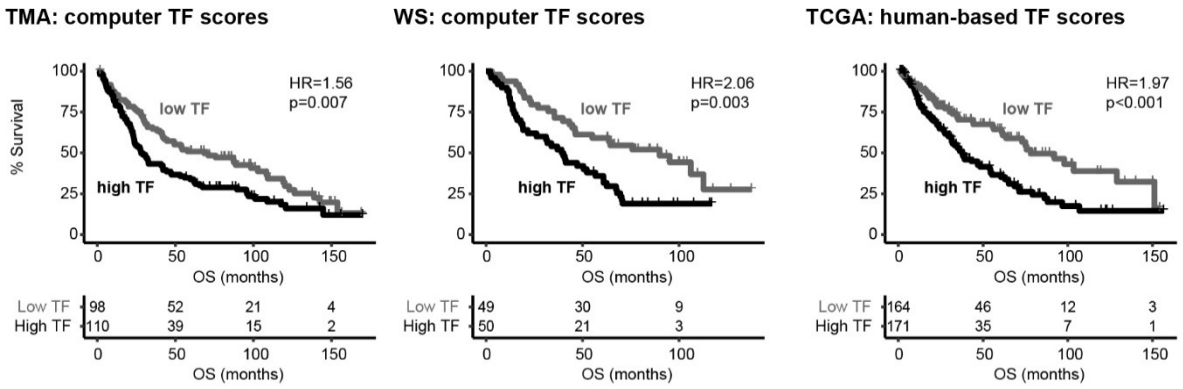

Figure 3: Overall survival curves based on tumor fragmentation. Kaplan Meier curves stratified by high/low TF, dichotomized at the median. HR=hazard ratio; CI=95% confidence interval. Computed TF scores were quantified on pan-cytokeratin stained tissue; Human-based scores were performed on H&E stained tissue.

Increasing TF scores had a significantly poor impact on OS as showed by both univariate and multivariate analysis (Table 2). Analysis for relapse free survival showed comparable results for the three patient cohorts (Table S3). Human-based scores showed similar results for WS (Table S4). By evaluating the subset of 77 patients from WS with matching TMA cores, we observed a decrease of prognostic power using TMA cores (OS/RFS: p=0.060/0.152), in comparison with whole sections (OS/RFS: p<0.001/<0.001), possibly due to the higher impact of intra-tumor heterogeneity on the TMA. TF scores using different minimal fragment size thresholds were also evaluated on WS. The prognostic relevance of TF was similar for a wide range of size cutoffs (5-100 cells) for both OS and RFS (Figure S2).

Table 2: Association of TF scores on whole sections with overall survival. Survival analysis by Cox univariate and multivariate regressions. HR=hazard ratio; CI=95% confidence interval. Computer: automatic scoring on pan-cytokeratin IHC stained tissue; Human: fragmentation scored by eye; TF (low/high): scores dichotomized at the median (categorical); TF (continuous): score as continuous variable.

OS		univariate			multivariate	
TMA (n=208)	**HR**	**95% CI**	**p-value**	**HR**	**95% CI**	**p-value**
TF (low/high) computer IHC	1.56	(1.12-2.16)	**0.008**	-	-	-
TF(continuous) computer IHC	1.05	(1.02-1.07)	**<0.001**	1.03	(1.01-1.06)	**0.018**
Stage [I, II, III, IV]	1.56	(1.29-1.90)	**<0.001**	1.45	(1.19-1.76)	**<0.001**
Grade [1,2,3]	1.34	(0.97-1.85)	0.075	1.20	(0.87-1.66)	0.266
Vessel infiltration	2.63	(1.89-3.65)	**<0.001**	1.64	(1.64-3.25)	**<0.001**
WS (n=99)	**HR**	**95% CI**	**p-value**	**HR**	**95% CI**	**p-value**
TF (low/high) computer IHC	2.06	(1.26-3.37)	**0.004**	-	-	-
TF(continuous) computer IHC	1.00	(1.00-1.00)	**<0.001**	1.00	(1.00-1.00)	**0.020**
Stage [I, II, III, IV]	1.81	(1.31-2.49)	**<0.001**	1.54	(1.08-2.20)	**0.016**
Grade [1,2,3]	1.76	(1.10-2.82)	**0.018**	1.45	(0.88-2.39)	0.144
Vessel infiltration	1.99	(1.23-3.24)	**0.005**	1.22	(0.71-2.09)	0.480
TCGA (n=335)	**HR**	**95% CI**	**p-value**	**HR**	**95% CI**	**p-value**
TF (low/high) human H&E	1.97	(1.40-2.77)	**<0.001**			
TF (continuous) human H&E	1.02	(1.01-1.03)	**0.001**	1.02	(1.01-1.03)	**0.001**
Stage [I, II, III, IV]	1.25	(1.02-1.53)	**0.030**	1.26	(1.03-1.54)	**0.025**
Grade [1,2,3]	-	-	-	-	-	-
Vessel infiltration	-	-	-	-	-	-

Tumor fragmentation is associated with changes in extracellular matrix

We selected TCGA patients with the upper and lower quartiles of TF scores to identify molecular characteristics associated with TF morphotypes and identified 910 genes associated with the high TF. Enriched biological processes involved tissue development, extra-cellular matrix (ECM) organization and cell adhesion processes (Figure S3). KEGG analysis notably showed an upregulation of pathways involved in ECM-receptor interaction, focal adhesion and protein digestion. In parallel, mass spectrometry-based label-free quantification identified 154 proteins significantly associated with increased TF (Table S5, see original publication) including extracellular (20%) and cytoskeletal (15%) components. In accordance with mRNA-Seq analysis, we observed an enrichment of genes involved in developmental processes.

In contrast, low TF was associated with 554 genes involved in diverse metabolic pathways including xenobiotics metabolism (Figure S3), and 205 proteins representing in majority

intracellular (70%) and nuclear proteins (46%). Biological nodes associated with decreasing TF were mostly related to hormone regulation processes.

We validated the expression of Periostin and Versican, two ECM proteins associated with TF in both RNA and protein analyses, by immunohistochemistry (IHC). The expression of both proteins in the tumor and stromal compartments was significantly associated with TF (Figure 4).

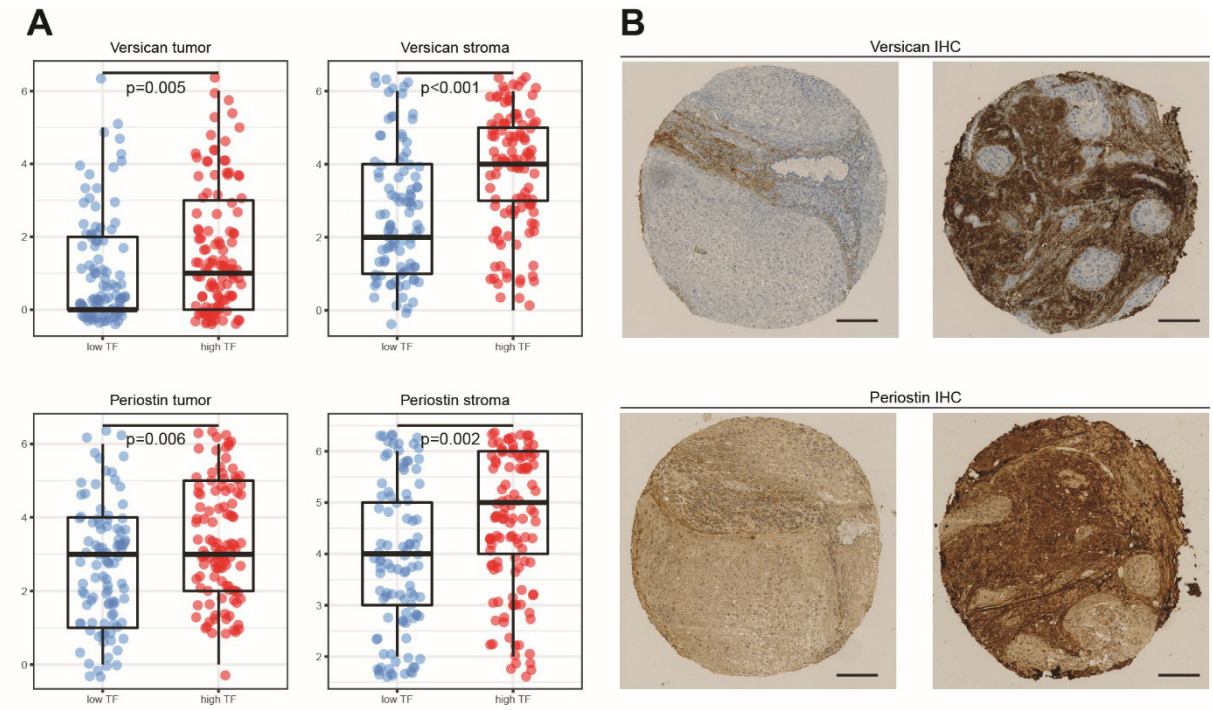

Figure 4: Versican and Periostin immunohistochemistry. Boxplots showing IHC scores for Versican and Periostin compartmentalized expression in tumor and stroma grouped by high and low TF scores dichotomized at the median. B) Matching IHC stained tumor cores. Scale bar: 100µm.

Discussion

LSCC is histologically characterized by a variable degree of keratinization and/or the formation of intercellular bridges between tumor epithelial cells. Collective cell migration is predominant in LSCC as other invasion modes such as EMT (epithelial-mesenchymal transition, fibroblastoid) or amoeboid are less observed probably due to the tight desmosomal adhesions (82, 83). This invasion pattern results in an apparent network of epithelial branches in 3D, which is

histologically depicted by a high variability of epithelia sizes in 2D. In this study, we used an image-based computational method to quantify such tumor fragments, hypothesizing that high fragmentation is a trait of increased tumor invasiveness. In support of this hypothesis, we showed that TF was associated with increased blood vessel, mediastinal and perineural invasion and worse patient outcome. Consistently, molecular analysis showed an upregulation of processes involved in ECM remodeling and focal adhesion, major characteristics of increased cellular motility (83-86). The association of TF with two identified ECM proteins, Periostin and Versican, was validated by immunohistochemistry. Periostin is a secreted ECM protein is observed in the desmoplastic stroma of a variety of cancers and known to promote cell invasion (87-90). It is also involved in cardiac remodeling after myocardial infarction (91). Versican is a major proteoglycan of the extracellular matrix upregulated in several tumor types including lung cancer (92) and has been notably associated with poor prognosis in NSCLC (93). It is also shown to favor tumor metastasis in Lewis lung carcinoma cell lines (94). In contrast, tumors with low TF showed an enrichment of diverse metabolic and xenobiotic processes notably contributing to the regulation of a number of chemotherapeutic drugs (95-97).

TNM staging is the only established system for predicting LSCC prognosis, whereas the value of tumor grading along the keratinization qualifier remains unclear. In this study, we evaluated the clinical relevance of LSCC stratification based on TF. Survival analysis showed that high TF is a poor prognostic marker independent from stage. This could be a useful additional grading parameter suggesting tumor invasiveness. Alternative histological parameters such as tumor budding have been proposed as various measures of tumor invasion in cancers notably in colorectal carcinoma (98-100). In NSCLC, single cells, tumor buds (<5 cells) or nests (≤15 cells) together with stroma thickness have also shown an impact on patient's survival (53-56), although small invasive tumor clusters are less frequent in LSCC. As shown in Figure 1, the

typical median and average LSCC epithelia clusters size in 2D is at least one order of magnitude higher than single cells and tumor buds. Furthermore, studies of the 3D tumor microarchitecture suggest that single cells may be part of tumor buds, which in turn may belong to larger tumor nests or branches (101).

Alternatively, current progresses in digital pathology have led to automated identification of prognostic features on histological sections, notably for non-small cell lung cancer (102). However, such methods are mostly based on the quantification of cellular (mostly nuclear and cytoplasmic) features. Our computational method is focused on a higher order feature of the tumor epithelia, related to tumor invasion patterns, which can be favorably translated into a human-based scoring system on H&E tissue staining. The proposed computational image-based analysis allowed unbiased scoring of tumor fragments, but has nevertheless intrinsic limitations. The main drawback is that normal epithelial lung structures as well as necrotic residues are also immune-reactive with pan-cytokeratin. To minimize false positive tumor fragments, adjacent normal tissue was covered and a minimal size threshold for tumor fragments (>800μm^2) was set. Finally, the clinical relevance of TF in the context of adjuvant therapy could not be addressed in this study, because of the high heterogeneity of treatment modalities across cohorts.

In conclusion, we have shown using an image-based computational approach, that high fragmentation of LSCC is a histologic trait associated with increased aggressiveness. In addition, the integration of molecular data showed an upregulation of proteins favoring extracellular matrix remodeling and focal adhesion, supporting the increased invasive potential of tumors with such high fragmentation. The proposed histologic parameter is an independent unfavorable prognostic marker that could be envisaged as new grading parameter for LSCC.

Acknowledgements

We would like to acknowledge Dr. Karina Silina (Institute of Experimental Immunology), Prof. Bernd Bodenmiller (Institute of Molecular Life Sciences), Prof. Renato Pajarola (Department of Informatics), Dr. Dimitri Korol (Cancer Registry) and Dr. Peter Schraml (Institute of Pathology and Molecular Pathology) for their critical input.

Supplementary figures

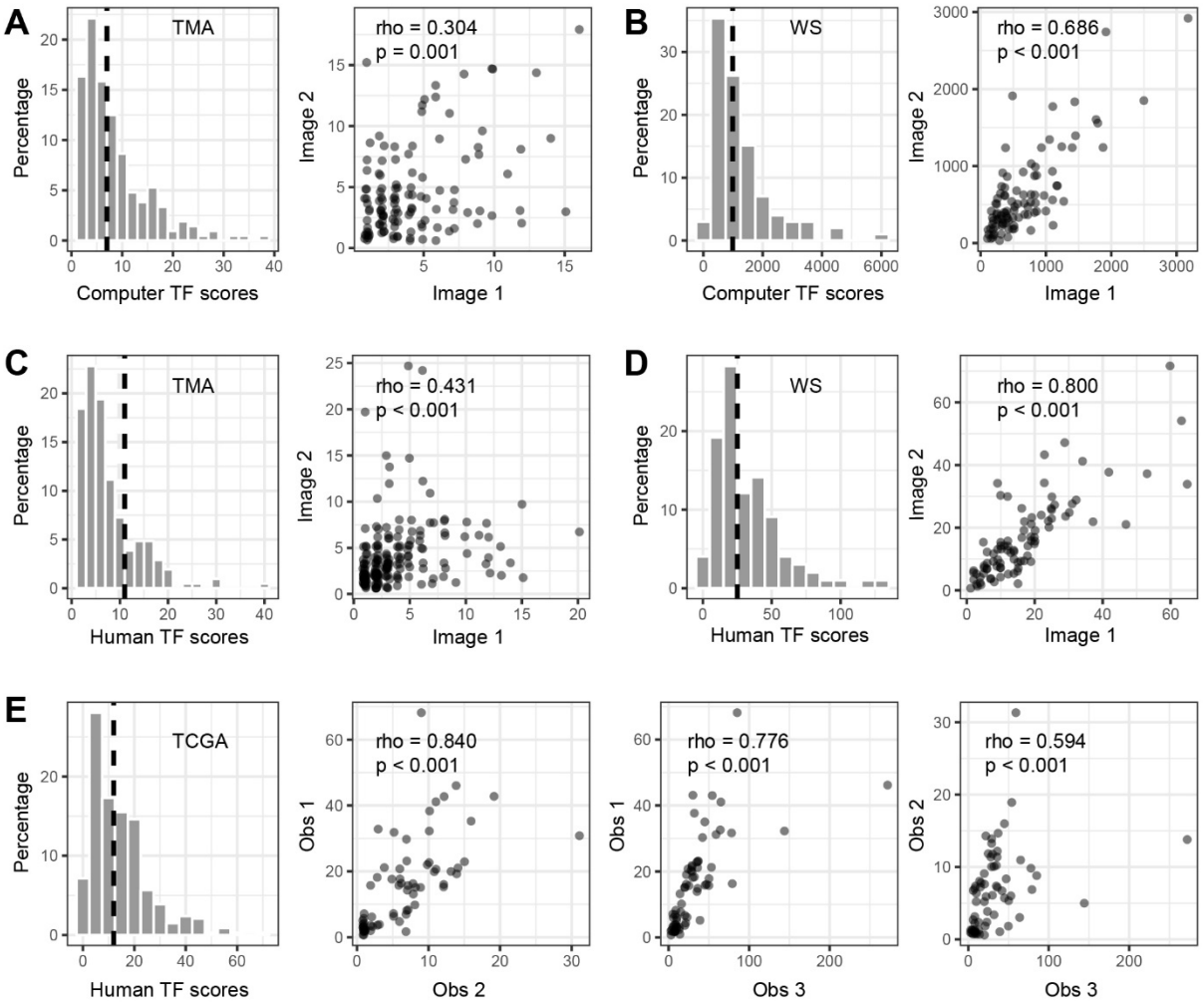

Figure S1: Frequency distributions, intra-tumor heterogeneity and inter-observer variability for TF scores. A) Percentage distribution of computed TF scores for TMA and correlation between matching cores. B) Percentage distribution of computed TF scores for WS and correlation between matching whole sections. C) Percentage distribution of human-based TF scores for TMA and correlation between matching cores. B) Percentage distribution of human-based TF scores for WS and correlation between matching whole sections. E) Percentage distribution of human-based TF scores for TCGA images from observer 1 (Obs1) and correlations between the three observers on a subset of pictures (n=67). Dashed line indicates the median.

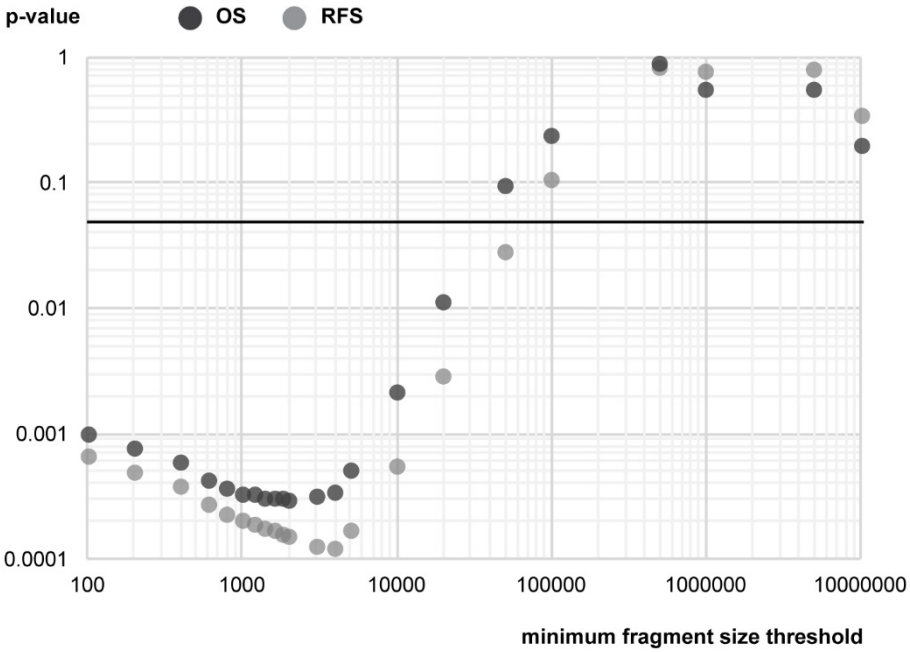

Figure S2: Threshold analysis of tumor fragmentation in correlation with RFS and OS. Series of cox univariate survival analyses are represented for the WS cohort. Data points represent single survival analyses repeated for computed TF scores using different tumor fragments size cut-offs. X-axis indicates the minimal size threshold for tumor fragments. Y-axis are the corresponding p-values. Black line indicates p=0.05.

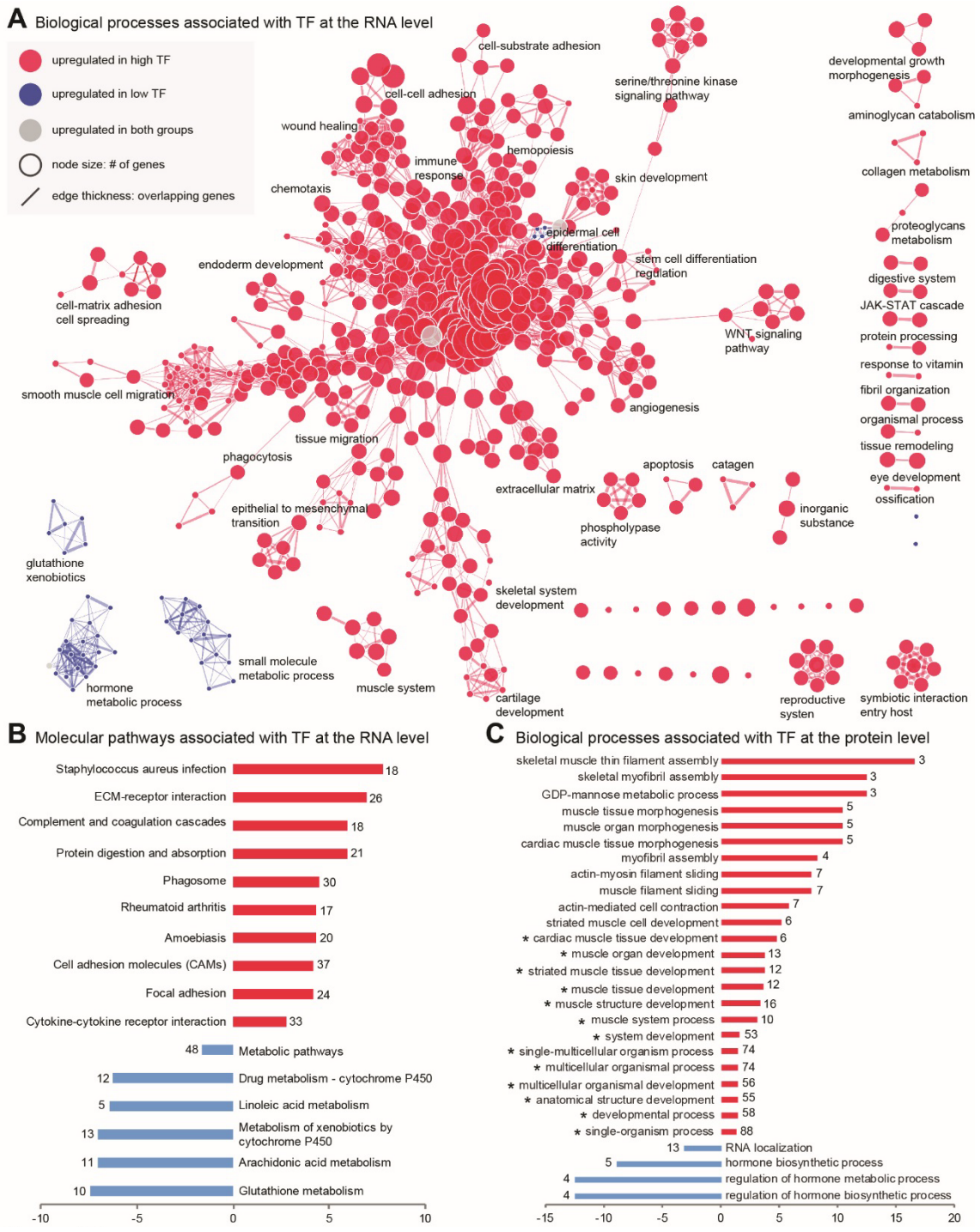

Figure S3: Biological processes associated with TF morphotypes from TCGA mRNAseq and WS Mass Spectrometry data. A) gene ontology network visualization of RNAs overexpressed in high (red) and low TF (blue) groups. B) bar plot showing molecular pathways associated with low (blue) and high (red) TF, at the RNA level. C) bar plot showing biological processes (BP) associated with increasing (red) and decreasing (blue) TF, at the protein level. Numbers indicate protein counts per category; asterisks* indicate BPs also enriched at the RNA level.

Supplementary tables

Table S2: Association of tumor fragmentation with clinico-pathological parameters.

	TMA (n=208)				WS (n=99)				TCGA (n=335)			
	low TF	high TF	p-value	p-value	low TF	high TF	p-value	p-value	low TF	high TF	p-value	p-value
	<med	>=med	low/high	continuous	<med	>=med	low/high	continuous	<med	>=med	low/high	score
Age			0.834	0.858			0.460	0.387			0.843	0.939
median	67	66			64	66			68	69		
Sex			0.084	0.414			**0.001**	**0.005**			0.269	0.88
female	12.0%	8.2%			3.0%	16.2%			13.4%	11.4%		
male	35.1%	44.7%			46.5%	34.3%			35.5%	39.7%		
pT			0.837	0.793			0.104	**0.001**			0.313	0.944
1	11.1%	9.6%			16.2%	8.1%			10.1%	10.1%		
2	22.1%	29.3%			15.2%	14.1%			30.8%	32.8%		
3	10.6%	10.1%			15.2%	19.2%			6.9%	5.1%		
4	3.4%	3.8%			3.0%	9.1%			1.2%	3.0%		
pN			0.801	0.487			0.725	0.321			0.968	0.958
0	23.6%	29.3%			25.3%	22.2%			30.7%	32.2%		
1	19.2%	15.4%			15.2%	16.2%			13.0%	13.6%		
2-3	4.3%	8.2%			9.1%	12.1%			5.4%	5.1%		
pM			0.698	0.669			0.061	0.072			0.173	0.090
0	44.7%	49.5%			49.5%	46.5%			49.8%	48.5%		
1a/b	2.4%	3.4%			0.0%	4.0%			0.3%	1.4%		
Stage			0.804	0.756			0.113	**0.009**			0.305	0.772
I	15.4%	18.8%			15.2%	9.1%			22.7%	26.6%		
II	19.2%	17.3%			18.2%	17.2%			17.6.%	14.6%		
III	10.6%	13.5%			16.2%	20.2%			8.4%	8.7%		
IV	1.8%	3.4%			0.0%	4.0%			0.3%	1.2%		
Grade			0.262	0.090			**0.012**	**0.008**			-	-
1-2	29.4%	28.8%			28.3%	16.2%			-	-		
3	17.8%	24.0%			21.2%	34.3%			-	-		
Size (cm)			0.068	0.311			0.586	**0.013**			-	-
median	3.5	4			4.3	5.8			-	-		
Vessel infiltration			**0.017**	**0.008**			**0.003**	**0.001**			-	-
absent	31.7%	26.9%			33.3%	19.2%			-	-		
present	15.4%	26.0%			16.2%	31.3%			-	-		
Adjuvant therapy			**0.016**	**0.016**			0.947	0.809			**0.028**	**0.045**
no	34.1%	29.8%			34.3%	35.3%			42.7%	48.0%		
yes	13.0%	23.1%			15.2%	15.2%			6.3%	3.0%		

Table S3: Association of TF scores with relapse-free survival.

RFS		univariate			multivariate	
TMA (n=170)	**HR**	**95% CI**	**p-value**	**HR**	**95% CI**	**p-value**
TF (low/high) computer IHC	1.64	(1.13-2.37)	**0.009**	-	-	-
TF (continuous) computer IHC	1.05	(1.02-1.08)	**0.002**	1.04	(1.01-1.08)	**0.010**
Stage [I, II, III, IV]	1.13	(0.87-1.46)	0.370	1.16	(0.88-1.52)	0.283
Grade [1,2,3]	1.21	(0.83-1.76)	0.320	1.06	(0.71-1.57)	0.784
Vessel infiltration	2.06	(1.41-3.02)	**<0.001**	1.93	(1.31-2.84)	**0.001**
WS (n=85)	**HR**	**95% CI**	**p-value**	**HR**	**95% CI**	**p-value**
TF (low/high) computer IHC	2.29	(1.32-3.96)	**0.003**	-	-	-
TF (continuous) computer IHC	1.00	(1.00-1.00)	**<0.001**	1.00	(1.00-1.00)	0.072
Stage [I, II, III, IV]	1.73	(1.22-2.45)	**0.002**	1.47	(1.00-2.16)	0.051
Grade [1,2,3]	1.67	(1.03-2.72)	**0.039**	1.41	(0.83-2.38)	0.201
Vessel infiltration	2.07	(1.23-3.48)	**0.006**	1.25	(0.67-2.33)	0.487
TCGA (n=181)	**HR**	**95% CI**	**p-value**	**HR**	**95% CI**	**p-value**
TF (low/high) computer IHC	2.08	(1.29-3.37)	**0.003**	-	-	-
TF (continuous) computer IHC	1.02	(1.00-1.04)	**0.028**	1.02	(1.00-1.04)	**0.016**
Stage [I, II, III, IV]	1.24	(0.90-1.69)	0.191	1.31	(0.94-1.81)	0.108
Grade [1,2,3]	-	-	-	-	-	-
Vessel infiltration	-	-	-	-	-	-

Table S4: Association of human-based TF scores with OS and RFS.

OS		TMA (n=208)			WS (n=99)	
univariate	**HR**	**95% CI**	**p-value**	**HR**	**95% CI**	**p-value**
TF (high/low) human H&E	1.35	(0.97-1.88)	0.080	2.48	(1.49-4.11)	**<0.001**
TF (continuous) human H&E	1.05	(1.02-1.07)	**<0.001**	1.00	(1.00-1.00)	**<0.001**
multivariate						
TF (continuous) human H&E	1.02	(0.99-1.05)	0.139	1.01	(1.00-1.02)	**0.012**
Stage [I, II, III, IV]	1.46	(1.19-1.78)	**<0.001**	1.53	(1.07-2.2)	**0.020**
Grade [1,2,3]	1.22	(0.88-1.70)	0.224	1.65	(1.02-2.69)	**0.043**
Vessel infiltration	2.37	(1.68-3.35)	**<0.001**	1.16	(0.66-2.05)	0.611
RFS		**TMA (n=170)**			**WS (n=85)**	
univariate	**HR**	**95% CI**	**p-value**	**HR**	**95% CI**	**p-value**
TF (high/low) human H&E	1.12	(0.79-1.68)	0.450	1.67	(0.99-2.81)	0.056
TF (continuous) human H&E	1.03	(0.99-1.07)	0.180	1.01	(1.00-1.02)	**0.015**
multivariate						
TF (continuous) human H&E	1.01	(0.97-1.05)	0.554	1.01	(1.00-1.01)	0.339
Stage [I, II, III, IV]	1.10	(0.84-1.44)	0.481	1.46	(0.98-2.16)	0.060
Grade [1,2,3]	1.18	(0.81-1.73)	0.390	1.57	(0.95-2.60)	0.082
Vessel infiltration	2.05	(1.39-3.03)	**<0.001**	1.44	(0.80-2.61)	0.227

Chapter 3

Computerized assessment of histologic tumor regression and correlation with FDG PET/CT in neoadjuvant chemotherapy treated lung squamous cell carcinoma

In preparation

Ruben Casanova[1], Anne-Laure Leblond[1], Martina Haberecker[1], Holger Moch[1], Irene Burger[2-3], Alex Soltermann[1].

1. *Institute of Pathology and Molecular Pathology, University Hospital Zurich, Switzerland*
2. *Department of Nuclear Medicine, University Hospital Zurich, Switzerland*
3. *Department of Radiology, University Hospital Zurich, Switzerland*

Corresponding authors

Ruben Casanova, Institute of Pathology and Molecular Pathology, University Hospital Zurich, Schmelzbergstrasse 12, CH-8091 Zurich, Switzerland. Tel: +41 44 255 39 29; ruben.casanova@usz.ch

Alex Soltermann, Institute of Pathology and Molecular Pathology, University Hospital Zurich, Schmelzbergstrasse 12, CH-8091 Zurich, Switzerland. Tel: +41 44 255 23 19; alex.soltermann@usz.ch

Running title

Tumor regression of lung squamous cell carcinoma by computational image analysis

Keywords

Lung, squamous cell carcinoma, neoadjuvant chemotherapy, digital pathology, prognosis.

Funding

This work was supported the Swiss Cancer League (reference number F-87701-31-01).

Disclosure/Conflict of interest

The authors declare to have no competing financial interest

Own contribution

Conception and design, development of methodology, acquisition of data, analysis and interpretation of data, writing of the manuscript.

Abstract

Introduction: Neoadjuvant chemotherapy is a treatment strategy aiming at reducing the tumor burden before surgery. In this setting, the amount of residual tumor burden is an important prognosticator although no regression scoring system is currently established. The integration of an image-based computational approach might provide a solid basis to measure reliably histopathologic regression.

Methods: A computerized morphometric approach was applied on whole histological sections from lung squamous cell carcinomas (LSCC), in order to quantify four morphologic features related to the residual tumor burden after neoadjuvant chemotherapy (n=55 patients). A cohort of chemo-naïve patients (n=104) was used for comparison. Positron Emission Tomography / Computed Tomography (PET/CT) measurements (n=23) were integrated for subsequent correlation analysis against quantitative morphometric parameters.

Results: After neoadjuvant chemotherapy, tumor area ($Tumor_{area}$), the percentage of tumor cells ($Tumor_{\%}$) as well as the amount (TF) and size of the largest residual fragment ($Size_{max}$) were significantly reduced compared to chemo-naïve LSCC. All four parameters significantly correlated with the maximum standard uptake value after neoadjuvant treatment. Survival analysis showed that $Tumor_{\%,}$ $Tumor_{area}$ and $Size_{max}$ were adequate parameters to stratify patients into risk categories based on a 3-years overall survival cutoff, whereas TF was the only significant parameter for chemo-naïve LSCC.

Conclusions: In this study, we emphasized the clinical relevance of using an image-based computational approach, to quantify histopathologic response after neoadjuvant chemotherapy. We believe this approach is not restricted to LSCC or to a particular treatment, and could therefore be a valuable method for quantitative pathologic readout of treatment success.

Introduction

In a neo-adjuvant setting, chemotherapy is given before surgery, as it may result in significant reduction of the tumor burden enabling radical resection in otherwise not operable patients. This treatment strategy has been shown to improve overall survival (OS) (103) and recurrence-free survival in resectable NSCLC (104). The classification of malignant tumors is done by the TNM staging (primary tumor, lymph node involvement and distant metastases) which is crucial for prognosis evaluation and treatment decisions (21). Although there is no WHO-accepted consensus for regression scoring of NSCLC, whereby the extent of residual vital tumor epithelial cells and the amount of fibrosis may be important parameters. Several regression systems have been proposed based on the percentage of remaining tumor cells (105-107) or the area of residual tumor (108).

However, previously proposed tumor regression scoring methods (TRS) relied on a semi-quantitative and subjective pathologic evaluation. The automatic quantification of morphologic parameters related to the amount and size of residual tumor tissue could be useful for improving and standardizing current tumor regression schemes in NSCLC (109).

In our study, we have evaluated two clinical cohorts of lung squamous cell carcinoma (SCC), the second most frequent histologic subtype of NSCLC. We have previously proposed an approach to quantify tumor fragmentation of LSCC, a structural feature related associated with increased tumor invasion (66). In this study, we aimed at extending our approach to quantify structural histologic changes after neoadjuvant chemotherapy (NAC). For this purpose, four histologic parameters (total tumor surface, tumor/stroma percentage as well as the amount and size of the largest residual tumor fragment) were compared between two patient cohorts, having received NAC or not.

Materials and Methods

Patient cohorts

In this retrospective study, patients with diagnosed primary lung SCC at the University Hospital Zurich were selected. Patients with non-squamous non-small cell lung cancer (NSCLC), synchronic or metachronic second primary tumor or with overall survival (OS) < 1 month post-surgery were excluded. Squamous cell differentiation was assessed on haematoxylin-eosin (H&E) and alcian blue-periodic acid schiff (AB-PAS) stains. Poorly differentiated SCC were verified by immunohistochemistry (IHC) using TTF1, p40, p63, CK7 and synaptophysin antibodies. Two clinical cohorts were selected separately in this study. The chemo-naïve cohort consisted of 179 patients diagnosed with lung SCC between January 2003 and June 2010 having complete clinical data. After revision for exclusion criteria, 104 patients were included. The neoadjuvant group consisted in 58 patients diagnosed with lung SCC between February 2000 and September 2012, undergoing surgery after neo-adjuvant chemotherapy at the University Hospital Zurich. After revision for exclusion criteria, 55 patients remained in this cohort. This study was approved by the Ethical Commission of the Canton of Zurich under reference number KEK ZH-Nr. 29-2009/14.

Histopathological samples preparation

For each cohort, two tissue blocks showing representative tumor areas were selected from H&E stained diagnostic cases. For few neoadjuvant treated cases, when the remaining tumor area was too small, only one whole section was selected. IHC was performed using mouse monoclonal anti-human cytokeratin AE1/AE3 (M3515, DAKO, dilution 1:50) on an automated platform (Ventana Medical Systems, Tucson, AZ, USA). The following detection was finalized with a secondary antibody and the OptiView DAB kit (Ventana Medical Systems). IHC stained sections were scanned using a high-resolution whole slide scanner (Nanozoomer Digital

Pathology, Hamamatsu, Japan) using a 40x objective with spatial resolution of 0.23µm/pixel. Tumor tissue was manually annotated by a surgical pathologist (A.S.) in order to exclude surrounding non-tumor lung tissue from the analysis.

Image processing and regression scoring

A color threshold was used to segment malignant tumor tissue (brown positive signal) from its surrounding desmoplastic stroma (blue-grey counterstain) using Fiji (73). The same method was used in (66). Morphologic parameters of the resulting segmentation masks were further extracted and quantified for each disconnected carcinoma fragment larger than 800µm^2. For each tumor specimen, the total surface covered by tumor cells ($Tumor_{area}$), the percentage of tumor cells ($Tumor_{\%}$), the total number of tumor fragments (TF) and the size of largest fragment ($Size_{max}$) were averaged from two histologic sections. Scores for cases with only one available tissue section were duplicated. For chemo-treated cases with extensive necrosis showing unspecific staining, tissue segmentation was performed by trainable algorithms using the software inForm Tissue Finder™ (PerkinElmer, Waltham, MA, USA) (Figure S1). Histologic regression scores were evaluated by eye on the two available tissue blocks, using a continuous scale (range: 0-100%). The tumor regression score (TRG) was evaluated for each case on the whole tissue collection, following criteria proposed by Junker *et al.*: TRG_{I}=<10% regression, TRG_{IIa}=[10-90]% regression, TRG_{IIb}=>90% regression, TRG_{III}=100% regression.

PET/CT acquisition and analysis

Patients from the NAC cohort with available FDG PET/CT before and after neoadjuvant treatment (before tumor resection) were analyzed. Patients' inclusion criteria was: acceptable quality of FDG PET/CT scans, not elevate blood glucose, fasting for at least 4 hours, FDG uptake time within 45-60 minutes and adequate FDG injection (< 100 MBq difference between both FDG injections). The detailed protocol is explained in (110).

Data interpretation and statistical analysis

All statistical analyses were performed on SPSS version 22 software (SPSS Inc., Chicago, USA). Overall survival (OS) and relapse-free survival (RFS) were evaluated from the date surgery to the date of death or documented relapse or as described (81). Only patients with no evidence of remaining tumor after surgical resection of the primary tumor were included in RFS calculations. Differences between NAC and NC morphologic parameters were addressed using the Mann-Whitney U test. Correlations between PET metrics (SUVmax, BSL, BSV) and morphologic parameters ($Tumor_{area}$, $Tumor_{\%}$, TF, $Size_{max}$) were calculated using the non-parametric Spearman's rank correlation test. A receiver operator characteristic (ROC) curve was generated for each morphologic parameter using a cutoff of 3 years RFS to separate short and long-term survivors. The area under the ROC curve (AUROC) was computed for each parameter. Patients with clinical follow-up shorter than 3 years were omitted in the ROC analysis. The optimal cut off point was determined for each parameter with the point that minimizes the distance to the (0,1) corner in the ROC plane (111). Mean overall survival and Kaplan-Meier p-values were calculated using the Log Rank test. Hazard ratios were retrieved by univariate cox regression. P-values <0.05 were considered significant.

Results

The frequency of clinic-pathologic parameters for both cohorts is summarized in Table 1. Both NAC and CN cohorts showed similar clinical parameters. In all cohorts, staging, lymph node involvement and distant metastasis were prognostic parameter. Particularly, in the NAC cohort, ypN0 and ypN1 had similar mOS (>80 months) whereas ypN2 subgroup had considerably shorter mOS (<26 months). Morphologic changes after NAC were compared with the CN group. Four morphologic parameters representing the total tumor cells surface ($Tumor_{area}$), the

percentage of tumor cells within the tumor area (Tumor %), the total number of tumor fragments (TF) and the largest fragment ($Size_{max}$) were automatically quantified for all LSCC cases (Figure1).

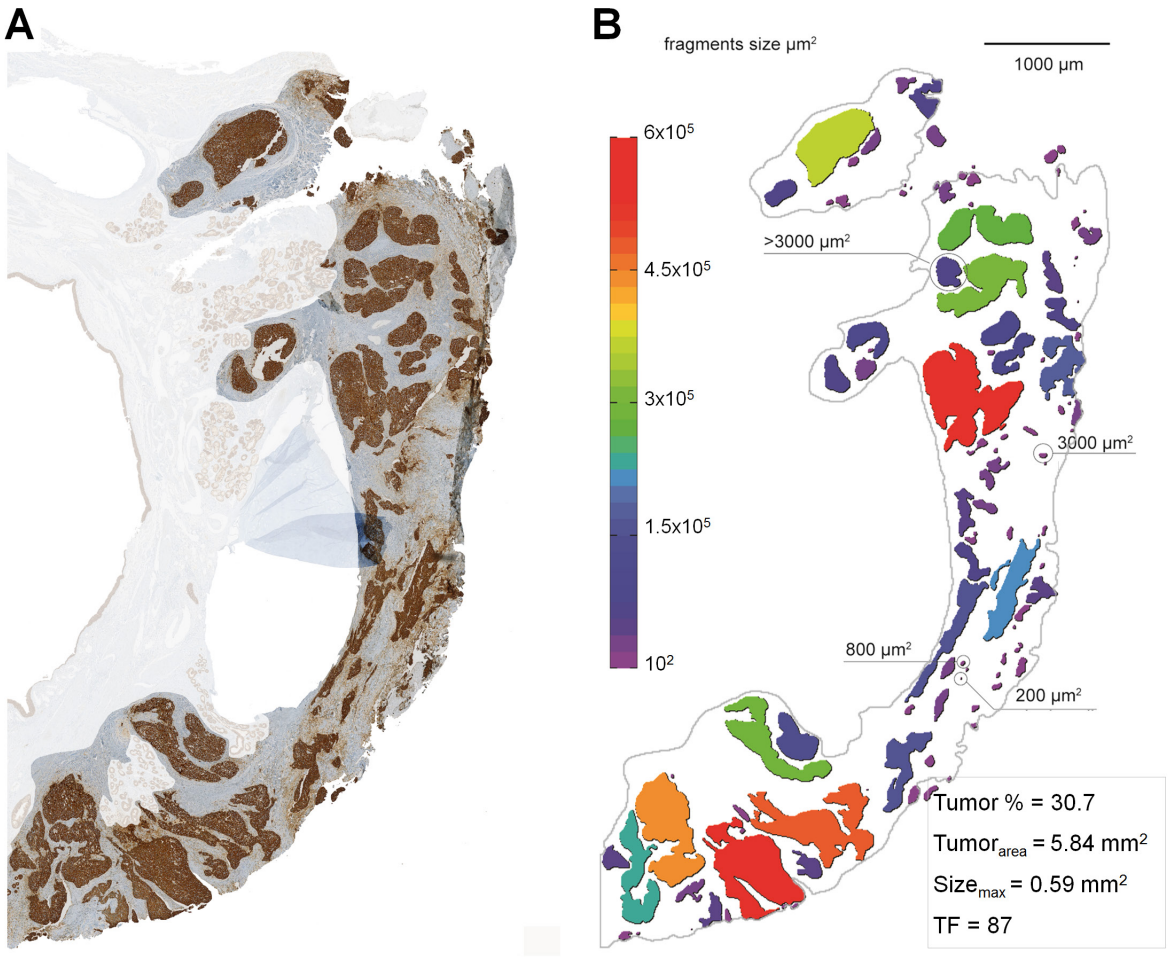

Figure 1: Computer-based morphometric analysis. A) Overview of a bronchial lung squamous cell carcinoma stained by pan-cytokeratin IHC. The non-malignant lung structures are masked by hand (glands, bronchus and cartilage). B) Corresponding segmentation mask of the tumor tissue. The tumor percentage in respect with the stroma, the tumor area, size of the largest fragment and number of fragments (TF) are computed.

Table 1: Summary of clinico-pathologic parameters and mean OS. Legend: NAC=neoadjuvant chemotherapy, mOS=mean overall survival; CI=95% confidence interval; p=Log Rank test p-value; yp(T/N/M)=pathologic evaluation after chemotherapy.

Clinical cohorts	chemo treated (NAC) n=55					chemo-naïve n=104				
	N	%	mOS	CI (95%)	p	N	%	mOS	CI (95%)	p
Age					**0.044**					0.169
≤62	33	(60%)	87.6	(67.6-107.5)		47	(45)%	75.6	(60.9-90.2)	
>62	22	(40%)	55.6	(34.4-76.7)		57	(55)%	63.4	(50.3-76.5)	
Sex					0.897					0.187
female	12	(22%)	73.3	(44.8-101.8)		21	(20)%	53.7	(39.8-67.6)	
male	43	(78%)	74.9	(56.7-93.1)		83	(80)%	71.5	(60.1-83)	
ypT/pT					0.612					**<0.001**
0	5	(9%)	87.4	(65.5-109.4)		0	(0)%	-	-	
1	19	(35%)	70.5	(42-99.1)		24	(23)%	87.7	(70.1-105.4)	
2	13	(24%)	79.2	(55.9-102.5)		34	(33)%	79.8	(63-96.5)	
3	7	(13%)	48.5	(23.5-73.4)		34	(33)%	54.7	(40.1-69.3)	
4	11	(20%)	43.3	(26.7-59.8)		12	(12)%	23.9	(9.9-37.9)	
ypN/pN					**0.005**					**0.001**
0	26	(47%)	81.5	(60.9-102)		49	(47)%	81.2	(67.1-95.3)	
1	20	(36%)	82.0	(56.3-107.6)		34	(33)%	52.5	(38.6-66.3)	
2	9	(16%)	25.9	(10-41.8)		20	(19)%	63.4	(40.8-86)	
3	0	(0%)	-	-		1	(1)%	8.1	(8.1-8.1)	
ypM/pM					**0.001**					**<0.001**
negative	54	(98%)	75.8	(60.1-91.6)		100	(96)%	71.3	(61.3-81.3)	
positive	1	(2%)	4.7	(4.7-4.7)		4	(4)%	7.2	(3.3-11)	
Stage					**<0.001**					**<0.001**
0	5	(9%)	87.4	(65.5-109.4)		0	(0)%	-	-	
I	13	(24%)	88.6	(59-118.2)		26	(25)%	89.8	(72.4-107.3)	
II	15	(27%)	87	(62.2-111.7)		38	(37)%	69.7	(56.5-82.9)	
III	21	(38%)	36	(23.5-48.4)		36	(35)%	51.2	(36.4-66.1)	
IV	1	(2%)	4.7	(4.7-4.7)		4	(4)%	7.2	(3.3-11)	
Neoadjuvant chemotherapy					0.239					-
platinum+gemcitabine	19	(35%)	56.2	(32.6-79.8)		-	-	-	-	
platinum+taxane	26	(47%)	75.8	(57.1-94.6)		-	-	-	-	
platinum+other	10	(18%)	93	(52.9-133.1)		-	-	-	-	
Cycles					0.904					-
2	3	(5%)	50.8	(12.6-89)		-	-	-	-	
3	43	(78%)	73.5	(55.8-91.2)		-	-	-	-	
4	7	(13%)	77.8	(47.1-108.6)		-	-	-	-	
5	2	(4%)	32.5	(14.5-50.5)		-	-	-	-	

The distribution of morphologic parameters was considerably different between the two cohorts and all four parameters were considerably reduced in NAC compared to CN (all p<0.001) (Figure 2A).

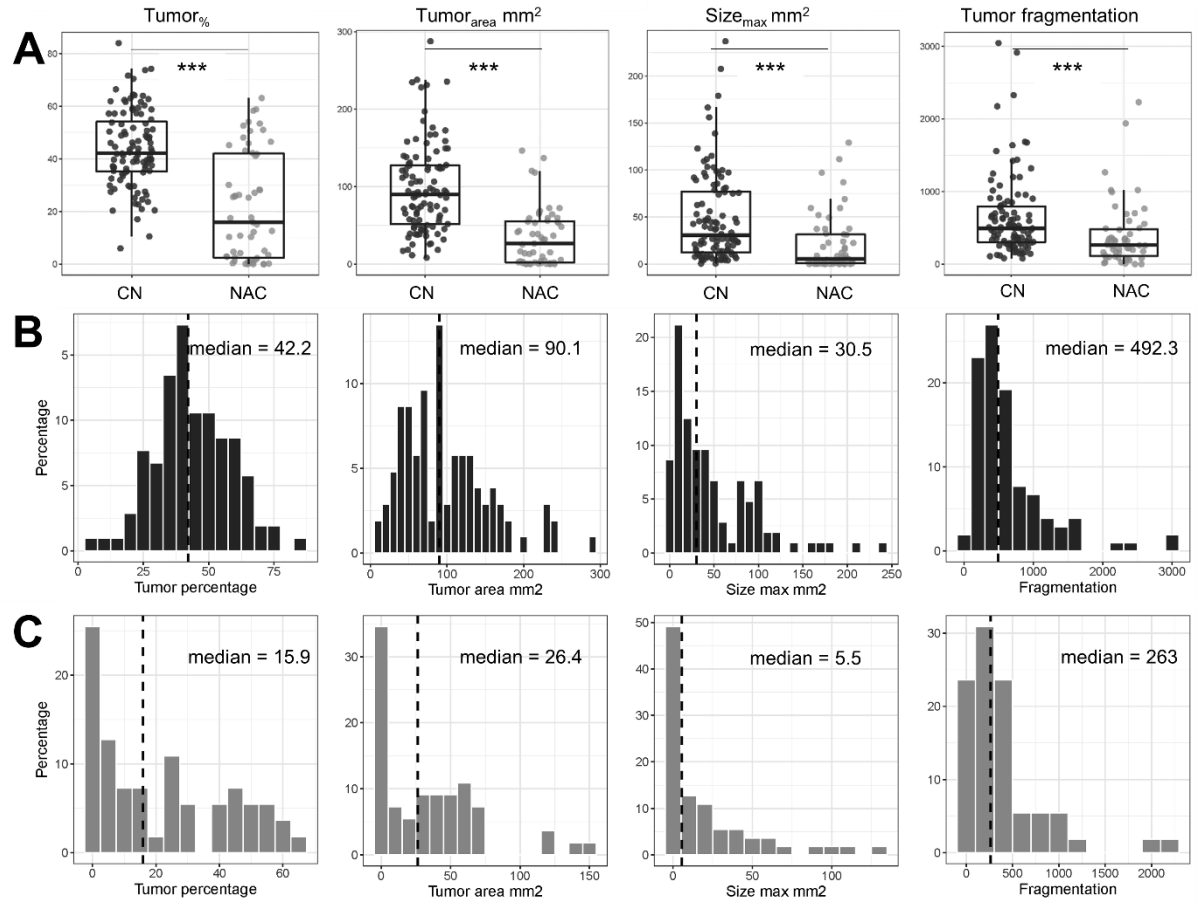

Figure 2: Morphologic changes between neoadjuvant chemotreated and chemo-naïve LSCC. A) Boxplots showing quantitative morphologic features stratified by neoadjuvant chemotherapy (NAC) and chemo-naïve (CN) LSCCs. B) Histograms showing the distributions of the four morphologic parameters for CN LSCCs and NAC (C). Legend: $Tumor_{\%}$=percentage of tumor cells; $Tumor_{area}$=tumor cells area; $Size_{max}$=size of the largest fragment; TF=number of fragments.

ROC analysis of the four morphologic parameters showed that $Tumor_{\%}$, $Tumor_{area}$, and $Size_{max}$ were able to stratify NAC patients in two risk groups - using a 3-years OS cutoff - but not TF (Figure 3A). In addition, Stage, ypN and $Tumor_{\%}$ were the most discriminant parameters and were superior than tumor regression scores performed by eye (Figure S2, left). In the ypN0-1 subpopulation, $Tumor_{\%}$ was the most significant parameter with the highest AUROC compared to the other morphologic parameters (Figure 3A) as well as Stage and ypN0-1 (Figure S2, right). This was confirmed by survival analysis (Table 2).

Table 2: Summary of morphologic parameters and mean OS for NAC patients. The computed parameters were dichotomized at the best cutoff point. Legend: NAC=neoadjuvant chemotherapy, mOS=mean overall survival; CI=95% confidence interval; p=Log Rank test p-value; TRG=tumor regression grade as described in (106); yp(T/N/M)=pathologic evaluation after chemotherapy.

NAC cohort	all patients (n=55)					ypN0-1 patients (n=46)				
	N	%	mOS	CI (95%)	p	N	%	mOS	CI (95%)	p
$Tumor_{\%}$					**0.004**					**<0.001**
<30%	38	(69%)	86.6	(68.6-104.5)		30	(65%)	100.9	(82.4-119.3)	
≥30%	17	(31%)	41.4	(18.2-64.5)		16	(35%)	43.5	(19.2-67.8)	
$Tumor_{area}$					**0.039**					**0.013**
<35 mm^2	31	(56%)	87.0	(67.5-106.6)		24	(52%)	101.6	(81.2-122)	
≥35 mm^2	24	(44%)	54.8	(33-76.6)		22	(48%)	59.3	(36.4-82.2)	
$Size_{max}$					**0.017**					**0.002**
<21mm^2	37	(67%)	85.5	(67.3-103.6)		29	(63%)	100	(81.2-118.7)	
≥21mm^2	18	(33%)	47.9	(23.5-72.3)		17	(37%)	50.3	(24.8-75.7)	
TRG					0.603					0.733
1	10	(18%)	63.5	(29.4-97.6)		9	(20%)	70.4	(35.2-105.5)	
2a	28	(51%)	73.6	(51-96.2)		22	(48%)	82.9	(57.2-108.6)	
2b	12	(22%)	63.0	(36.7-89.3)		10	(22%)	71.3	(42.1-100.5)	
3	5	(9%)	87.4	(65.5-109.4)		5	(11%)	87.4	(65.5-109.4)	

Kaplan Meier survival curves were represented for $Tumor_{\%}$ at the best cutoff point (Figure 3B). Similar results were found using a 3 years RFS cutoff (Figure S3). In contrast, for CN patients, $Tumor_{\%}$, $Tumor_{area}$, and $Size_{max}$ were not significant parameters whereas TF was the best discriminative morphologic parameter using a 3 years RFS (p=0.030) and OS (p=0.051) (Figure S4).

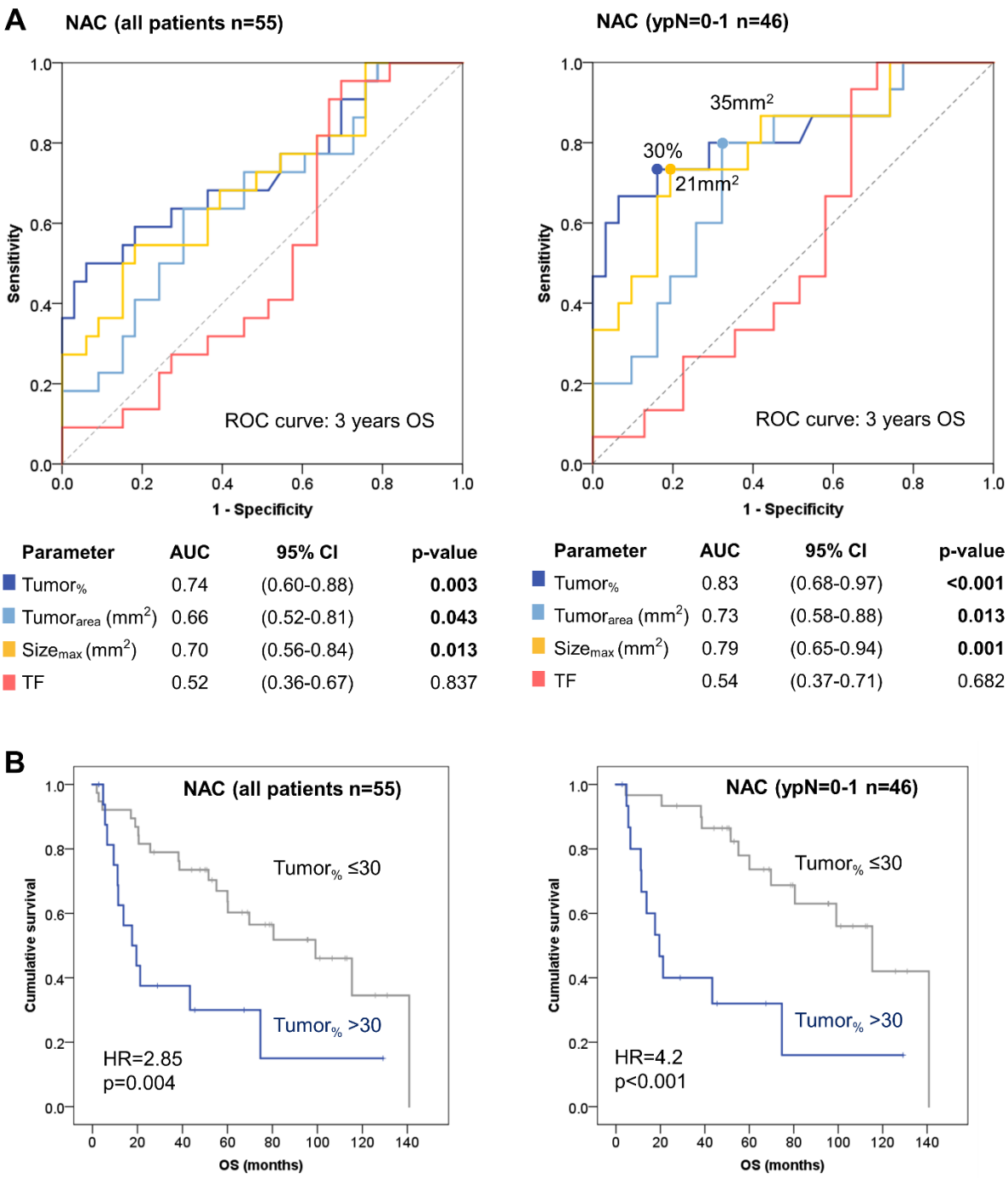

Figure 3: ROC and survival analysis of morphologic parameters for NAC patients. A) Receiver operator characteristic curve was generated for the four morphologic parameters and 3-years overall survival, for all NAC patients (left) and pN0-1 (right). Dots show the best cutoff points for significant parameters. B) Kaplan Meier survival curve for $Tumor_{\%}$, the parameter with the largest area under the curve (AUC=0.83). Legend: NAC=neoadjuvant chemotherapy group; CI=confidence interval; $Tumor_{\%}$=percentage of tumor cells; $Tumor_{area}$=tumor cells area; $Size_{max}$=size of the largest fragment; TF=number of fragments; HR=hazard ratio.

FDG PET-CT imaging data was retrieved for subset of NAC patients, before and after NAC treatment. Correlation analysis showed that SUVmax post-chemotherapy (before surgery) positively correlated with the four histologic parameters. Tumor area was the morphologic parameter best correlating with SUVmax, BSL and BSV post chemotherapy ($p<0.01$) (Figure 4). Interestingly, PET values before NAC treatment did not correlate with any morphologic parameter.

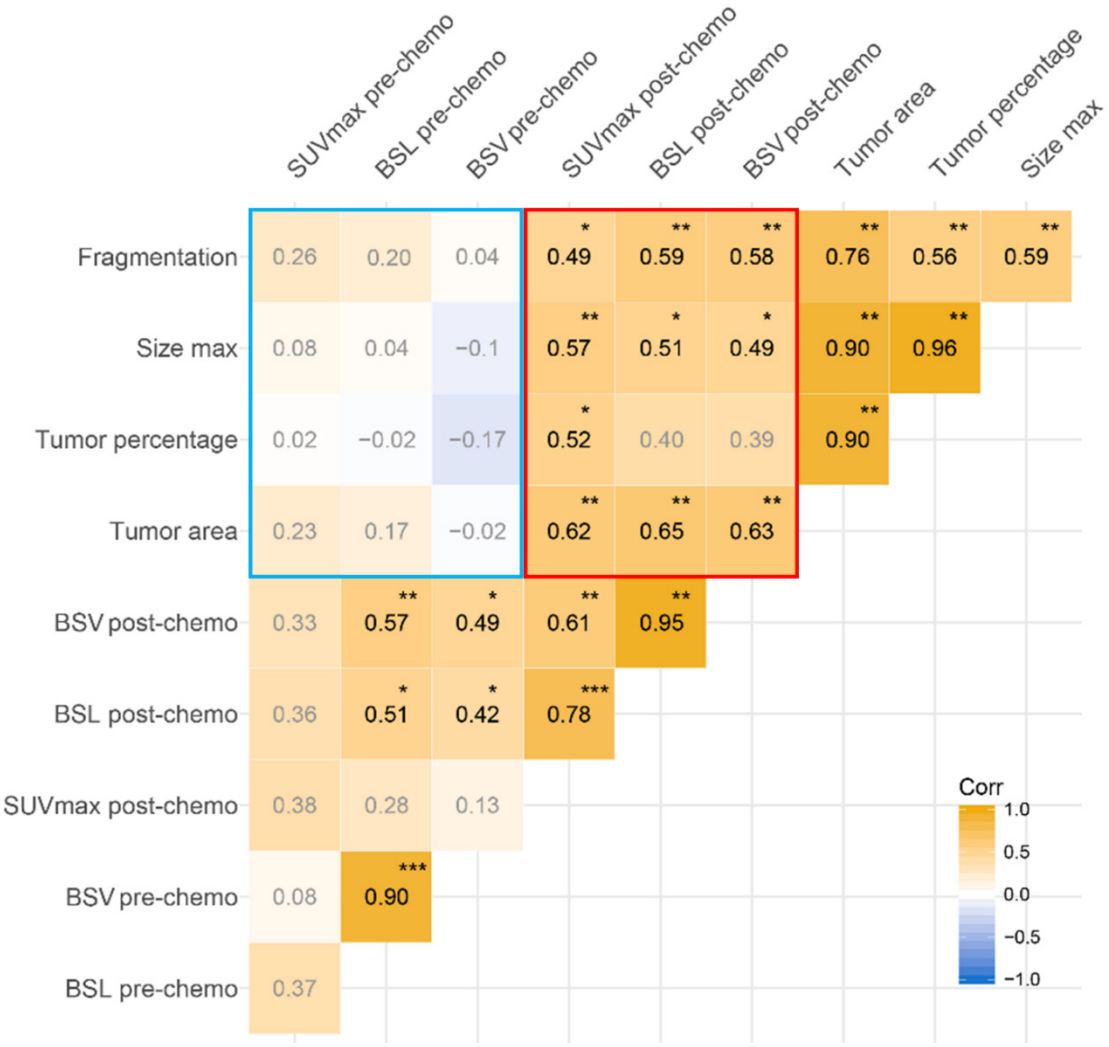

Figure 4: Correlation matrix of FDG PET/CT and morphologic parameters. PET/CT values before and after NAC (n=23 patients) were correlated with continuous morphologic values (n=55 patients). Correlation coefficients (Corr) are indicated with a corresponding color-scale: blue=negative, orange=positive. Correlations of PET values before/after NAC with morphologic parameters are highlighted by blue/red boxes. Legend: BSL=total lesion glycolysis (background subtracted); BSV=metabolic volume (background subtracted).

Discussion

Neoadjuvant chemotherapy produces distinctive morphological changes of both tumor and stromal compartments often resulting in the reduction of tumor burden accompanied by an increase of the fibrotic stroma and necrosis and the infiltration of foam cell and macrophages (112). Several tumor regression models - based on the extent of residual vital tumor epithelial cells – have been proposed for NAC treated NSCLC, by means of classical pathology. Despite past efforts, there is still no currently established tumor regression system although the pathologic response could be a valuable surrogate for overall survival (113). Junker *et al*. proposed a regression scheme in 3 grades starting from a grade 1 defined as no or only spontaneous regression, a grade 2 as incomplete regression (2a with >10%, 2b with ≤10% vital tumor cells) and grade 3 as complete regression without any detectable vital cells (105, 106). Based on this, it has been showed that NSCLC with less than 10% of residual viable tumor cells (107, 114), a pathological complete remission (115-117) or a total residual tumor area ≤400 mm^2 (108) were favorable prognostic parameters. Alternatively, tumor-infiltrating lymphocytes might also predict response to chemotherapy for NSCLC (118). However, traditional pathology relies on visual examinations and semi-quantitative scoring methods. The automatic quantification of morphologic parameters could be a good indicator of the effectiveness of therapy in NSCLC (109).

We focused our study on morphologic changes induced by NAC for lung squamous cell carcinoma (LSCC). Unlike adenocarcinoma which can present five distinct morphologic patterns (47), LSCC is histologically mainly characterized by the presence of keratinization or basaloid features (21). We evaluated four potentially prognostic parameters by quantitative pathology, using a chemo-naïve cohort for comparative analysis. We showed that parameters related to the remaining tumor burden after NAC (tumor percentage, tumor area, size of the largest

fragment) are prognostic parameters. In contrast, these parameters were not prognostic in a chemo-naïve setting, whereas TF, a parameter reflecting tumor invasiveness, was prognostic only in this group. This suggests that differential tumor grading should be performed depending if the patient received a therapy prior to surgical resection.

In addition, we observed an increase of prognostic power of morphologic parameters for cases without distant lymph node metastasis (N2). This suggests that histopathologic response at the primary site only is suboptimal for accurate regression evaluation. Although the presented parameters are highly associated to each other (figure 4), survival analysis suggested that tumor percentage might be a robust parameter to assess tumor regression. In addition, our quantitative method was more performant to stratify patients into high and low risk categories compared human-based regression scores.

FDG PET/CT is a potentially valuable imaging modality to predict histologic response after neoadjuvant therapy (119).

In our study, PET/CT analysis was performed using SUVmax, and background substracted values for the total lesion glycolysis (BSL) and metabolic tumor volume (BSV). We have previously shown that these parameters were correlated better with histopathologic tumor regression score in NSCLC than methods using a fixed threshold (42% SUVmax) (110). In this study, we showed that SUVmax measured after chemotherapy and before tumor resection significantly correlated with all morphologic parameters. However, PET values before neoadjuvant chemotherapy did not correlate with any morphologic parameter. This is in line with previous studies, showing that standardized uptake values correlate with histopathologic responses in NSCLC (120-125) whereas pre-chemo PET/CT might be insufficient to predict pathologic response in LSCC (122).

Our study has nevertheless several limitations. We presented a retrospectively and, due to the limited availability of NAC tumor specimens, no validation cohort could be analyzed. Therefore, before implementing a new tumor regression system, a larger clinical study needs to be performed. Furthermore, the morphometric analysis was performed using two tissue blocks showing remnants of tumor, whereas tissue blocks showing complete regression were ignored. For this reason, our $Tumor_{\%}$ scores are virtually higher and cannot be directly compared with previously published pathologic scores. In addition, our study focused solely on squamous cell carcinoma of the lung, which is a subtype of NSCLC. As proposed by the Association for the Study of Lung Cancer (IASLC)/the American Thoracic Society (ATS)/the European Respiratory Society (ERS), adenocarcinoma can be grouped into five morphologic subtypes: lepidic, acinar, papillary, micropapillary and solid (47). However, these morphologic patterns of might significantly affect FDG uptake (126) and it has been shown that squamous cell carcinomas have higher SUV uptake than adenocarcinomas (127-131). Therefore, we deliberately included solely LSCC in our study, in order to study a homogeneous population by morphometric and PET analyses.

In conclusion, our study suggests that quantitative pathology approaches may empower diagnostic power in pathology in particular to assess the pathologic response after treatment. Our approach is not restricted to LSCC and can be potentially applied to quantify histologic treatment response in other squamous cell carcinomas.

Acknowledgements

We would like to acknowledge Dr. Karina Silina (Institute of Experimental Immunology, University of Zurich), Dr. Dimitri Korol (Cancer Registry, University Hospital Zurich) and the Cancer Biology PhD program of the University of Zurich for their support.

Supplementary figures

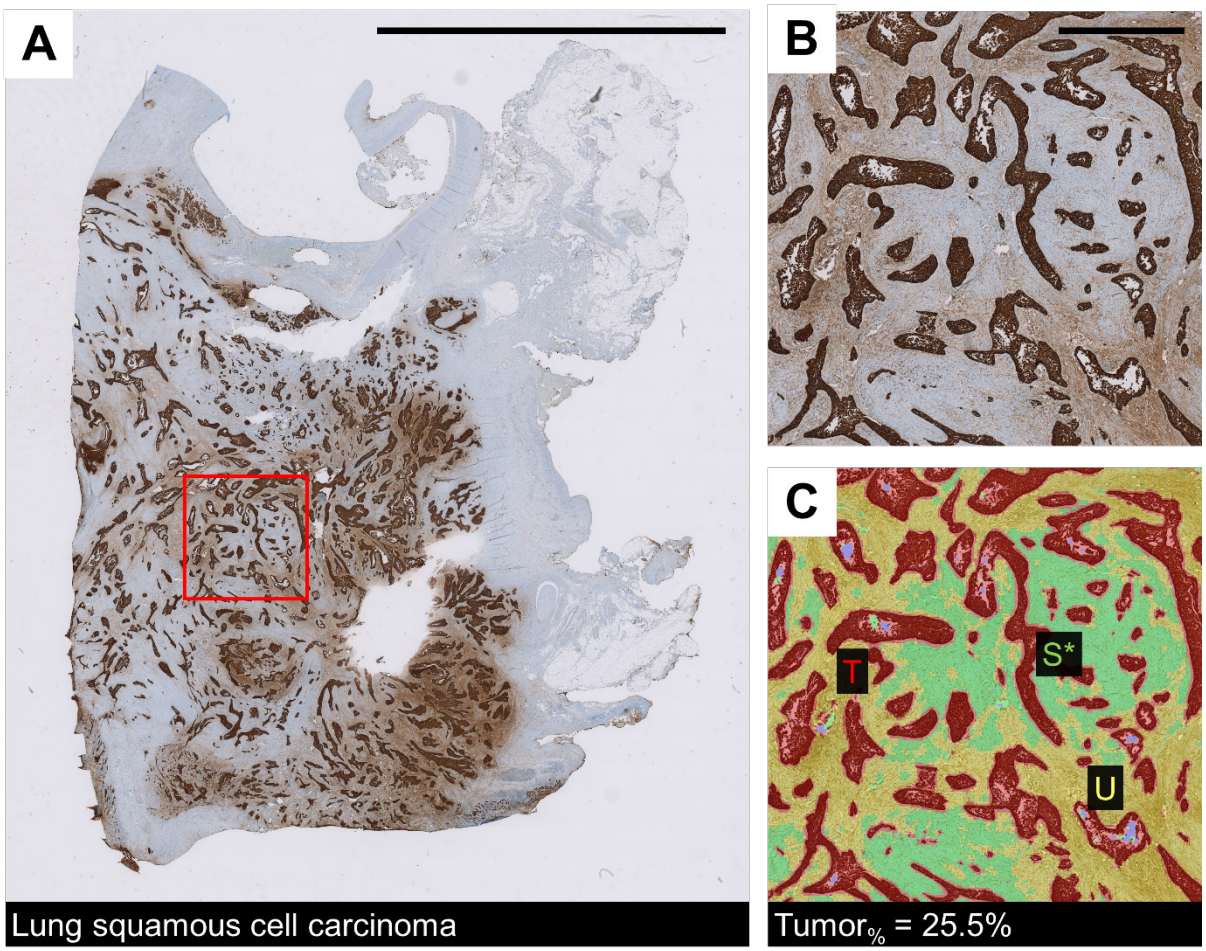

Figure S1: Tumor tissue segmentation using trainable algorithms. A) Overview of a lung squamous cell carcinoma stained by pan-cytokeratin IHC. Scale bar: 10mm. B) 10x magnification, scale bar: 1000µm. C) Corresponding segmentation mask using the software inForm Tissue Finder™. Legend: T=tumor cells; S=stroma; U=unspecific staining, accounting for stroma; background: purple.

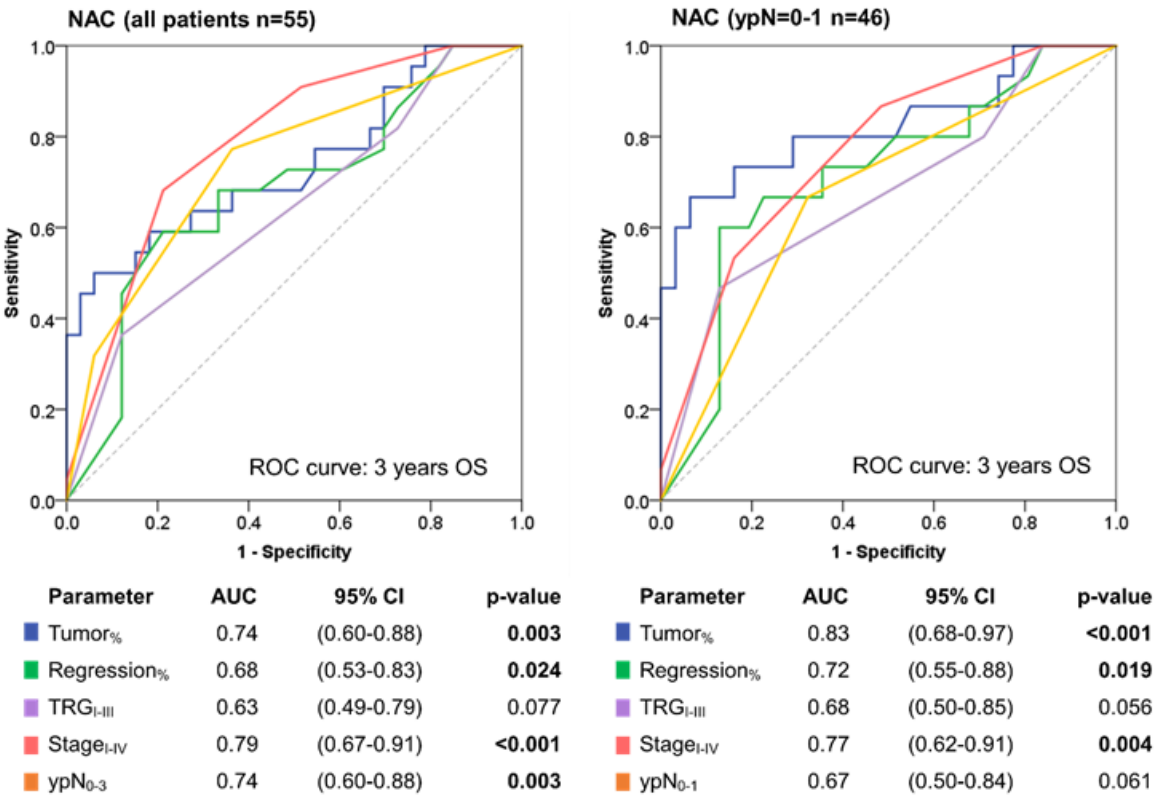

Parameter	AUC	95% CI	p-value
Tumor%	0.74	(0.60-0.88)	**0.003**
Regression%	0.68	(0.53-0.83)	**0.024**
TRGI-III	0.63	(0.49-0.79)	0.077
StageI-IV	0.79	(0.67-0.91)	**<0.001**
ypN0-3	0.74	(0.60-0.88)	**0.003**

Parameter	AUC	95% CI	p-value
Tumor%	0.83	(0.68-0.97)	**<0.001**
Regression%	0.72	(0.55-0.88)	**0.019**
TRGI-III	0.68	(0.50-0.85)	0.056
StageI-IV	0.77	(0.62-0.91)	**0.004**
ypN0-1	0.67	(0.50-0.84)	0.061

Figure S2: ROC and survival analysis of pathologic and morphologic parameters for NAC patients. Receiver operator characteristic curve was generated for Stage, ypN and histologic regression scores for all NAC patients (left) and ypN0-1 (right). Legend: NAC=neoadjuvant chemotherapy group; AUC=area under the curve; CI=confidence interval; Tumor%=percentage of tumor cells, computed; Regression%=percentage of regressed tumor tissue, scored by eye; TRG=tumor regression score (I, IIa, IIb, III), scored by eye, values were inverted in this plot; ypN=lymph node involvement.

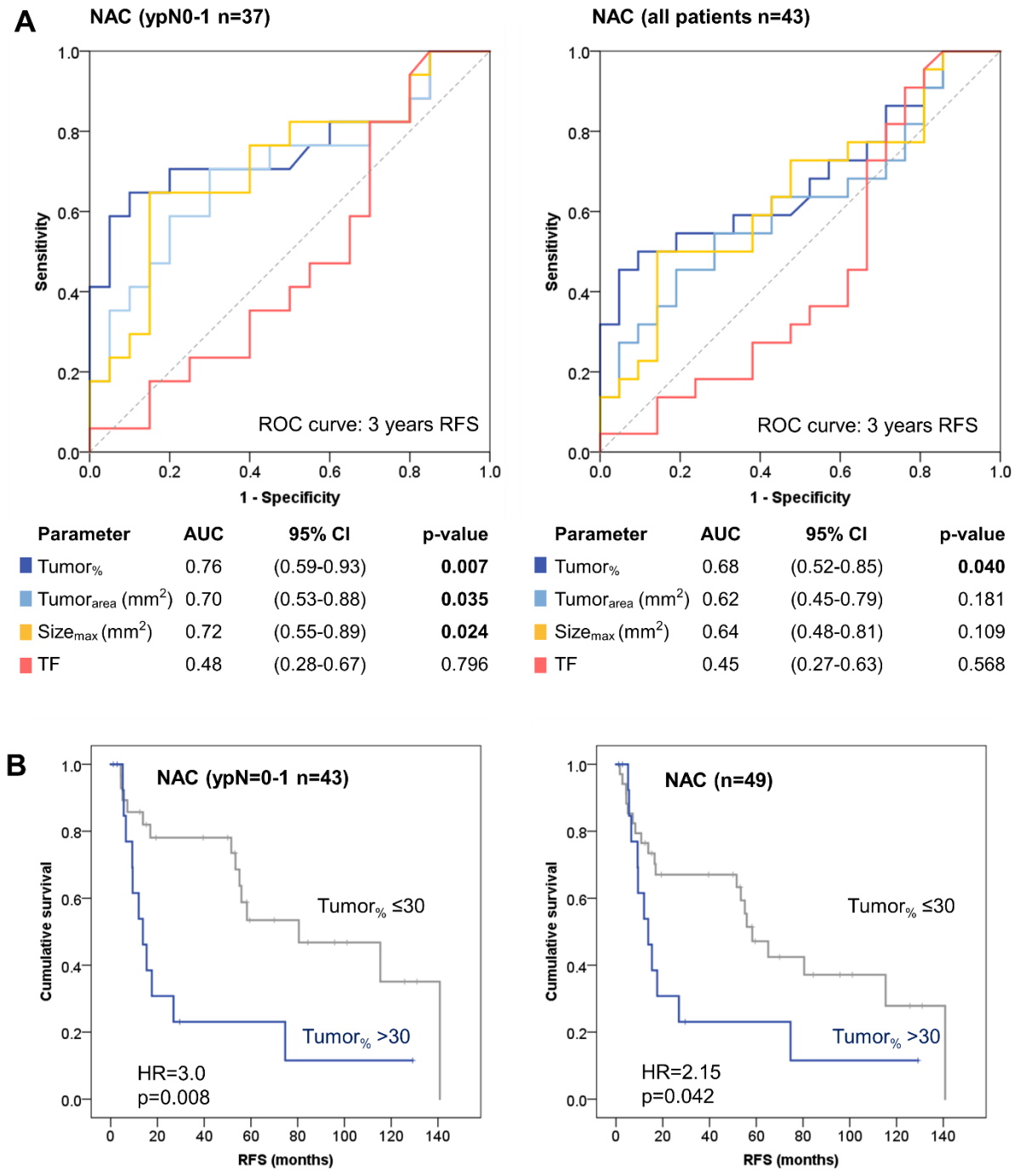

Parameter	AUC	95% CI	p-value
$Tumor_{\%}$	0.76	(0.59-0.93)	**0.007**
$Tumor_{area}$ (mm^2)	0.70	(0.53-0.88)	**0.035**
$Size_{max}$ (mm^2)	0.72	(0.55-0.89)	**0.024**
TF	0.48	(0.28-0.67)	0.796

Parameter	AUC	95% CI	p-value
$Tumor_{\%}$	0.68	(0.52-0.85)	**0.040**
$Tumor_{area}$ (mm^2)	0.62	(0.45-0.79)	0.181
$Size_{max}$ (mm^2)	0.64	(0.48-0.81)	0.109
TF	0.45	(0.27-0.63)	0.568

Figure S3: ROC and relapse-free survival analysis of morphologic parameters for NAC patients. A) Receiver operator characteristic curve was generated for the four morphologic parameters and 3 year RFS, stratified by ypN0-1 (left) and ypN2(right). B) Kaplan Meier survival curve for $Tumor_{\%}$, the parameter with the largest area under the curve (AUC=0.76). Legend: NAC=neoadjuvant chemotherapy group; CI=confidence interval; $Tumor_{\%}$=percentage of tumor cells; $Tumor_{area}$=tumor cells area; $Size_{max}$=size of the largest fragment; TF=number of fragments; HR=hazard ratio.

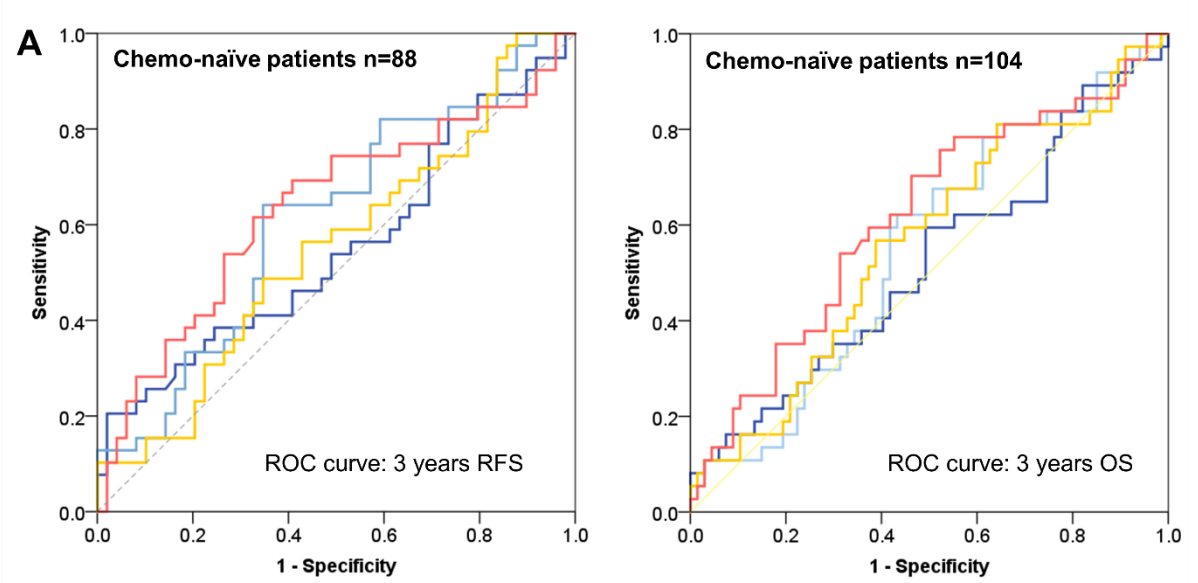

Parameter	AUC	95% CI	p-value
$Tumor_{\%}$	0.55	(0.41-0.69)	0.772
$Tumor_{area}$ (mm^2)	0.61	(0.47-0.74)	0.066
$Size_{max}$ (mm^2)	0.54	(0.41-0.68)	0.403
TF	0.65	(0.52-0.78)	**0.030**

Parameter	AUC	95% CI	p-value
$Tumor_{\%}$	0.52	(0.40-0.64)	0.716
$Tumor_{area}$ (mm^2)	0.55	(0.44-0.67)	0.365
$Size_{max}$ (mm^2)	0.56	(0.45-0.68)	0.279
TF	0.62	(0.50-0.73)	0.051

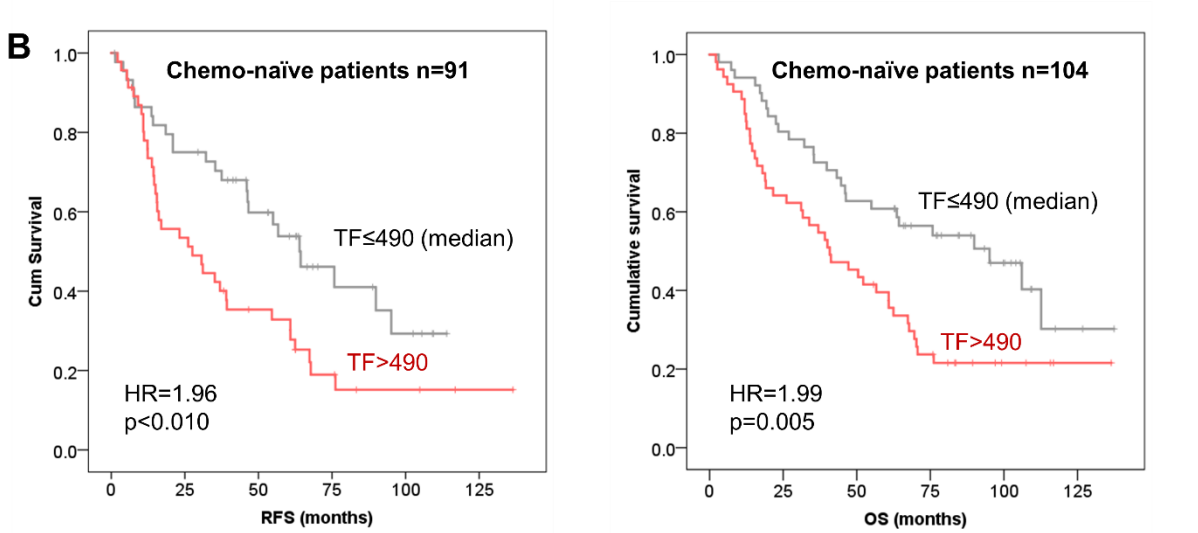

Figure S4: ROC and survival analysis of morphologic parameters for CN patients. A) Receiver operator characteristic curve was generated for the four morphologic parameters and 3 year overall survival and relapse-free survival. Below: area under the curve and corresponding lower-upper bound of the four parameters. Cases with clinical follow-up < 3years were omitted (n=3). Since there was no optimal cutoff point for TF, the median was chosen as dichotomization point for Kaplan Meier curves (B). Legend: AUC=area under the curve; CI=confidence interval; $Tumor_{\%}$=percentage of tumor cells; $Tumor_{area}$=tumor cells area; $Size_{max}$=size of the largest fragment; TF=number of fragments; HR=hazard ratio.

Chapter 4

FDG-PET/CT of non-small cell lung carcinoma under neo-adjuvant chemotherapy: background based adaptive volume metrics outperform TLG and MTV in predicting histopathological response

Journal of Nuclear Medicine, published on January 28, 2016
doi:10.2967/jnumed.115.167684

Irene A. Burger [1,2], Ruben Casanova [3], Seraina Steiger[2], Lars Husmann[1], Paul Stolzmann[1], Martin W. Huellner[1], Alessandra Curioni[4], Sven Hillinger[5], C. Ross Schmidtlein[6], Alex Soltermann[3].

1 Nuclear medicine, University Hospital Zurich, Switzerland
2 Radiology, University Hospital Zurich, Switzerland
3 Surgical Pathology, University Hospital Zurich, Switzerland
4 Medical Oncology, University Hospital Zurich, Switzerland
5 Thoracic Surgery, University Hospital Zurich, Switzerland
6 Medical Physics, Memorial Sloan Kettering Cancer Center, New York, USA

Corresponding Author:

Irene A. Burger, Department of Nuclear Medicine, University Hospital Zurich, Ramistr. 100, CH-8091 Zurich.

Tel. +41 44 255 35 55

Email: irene.burger@usz.ch

Running title

Background adapted response assessment

Acknowledgments

IAB was financially supported by the Prof. Dr. Max Cloëtta Foundation (Switzerland) and the Swiss Society of Nuclear Medicine. RC is supported by the Swiss Cancer League (ref. nr. F-87701-31-01). This research was funded in part through the NIH/NCI Cancer Center Support Grant P30 CA008748.

Conflict of interest

There is no potential conflict of interest relevant to this article.

Own contribution

Conception and design, acquisition of data, interpretation of data, review of the manuscript.

Abstract

Assessment of tumor response after chemotherapy using FDG PET metrics is gaining acceptance. Several studies have suggested that the parameters metabolically active tumor volume (MTV) or total lesion glycolysis (TLG) are superior for measuring the tumor burden compared to the maximum standardized uptake value (SUVmax). However, the measurement of MTV and TLG is still controversial; the most commonly method uses an absolute threshold of 42% of SUVmax. Recently we implemented a background adaptive method to determine the background subtracted lesion activity (BSL) and the background subtracted volume (BSV). In this study, we investigated the correlation between such PET metrics and histopathological response in non-small cell lung carcinoma (NSCLC).

Patients and Methods: Forty-four NSCLC patients were retrospectively identified. Their PET/CT data before and after neo-adjuvant chemotherapy was analyzed regarding SUVmax, MTV, TLG, BSL, and BSV on both scans and the relative changes (delta = d) were calculated (dSUVmax, dMTV, dTLG, dBSL, and dBSV). The tumor regression grade (TRG) as an indicator of histopathological response was assessed on H&E stained sections of the surgical specimens using a 4-tiered scale (TRG1–TRG4). The TRG was correlated with the absolute PET metrics after chemotherapy and their relative changes, respectively, using Spearman's rank correlation tests.

Results: Tumors that demonstrated a good response after neo-adjuvant chemotherapy had significantly lower FDG activity than non-responders (TRG3-4: SUVmax 4.2 (1.8-7.9) versus TRG1-2: SUVmax 8.1 (1.4- 40.4), p=0.001). The same was found for dSUVmax and TRG (p=0.001). PET volume metrics based on a 42% fixed threshold of SUVmax did not correlate

with TRG (TLG: p=0.505 and MTV: p=0.386). However, both background activity-based PET volume metrics BSL and BSV significantly correlated with TRG (p<0.001 each).

Conclusion: PET volume metrics based on background adaptive methods correlate better with histopathological TRG in NSCLC patients under neo-adjuvant chemotherapy than algorithms/methods using a fixed threshold (42% SUVmax).

Key words: Volume segmentation, tumor regression, quantification, NSCLC, neo-adjuvant therapy.

Introduction

Therapy response assessment is a fast increasing field for FDG PET/CT in oncology imaging *(132)*. The correlation between the maximum standardized uptake value (SUVmax) and the histopathological tumor regression upon radiotherapy (133) or neo-adjuvant chemotherapy (120) has been established in non- small cell lung cancer (NSCLC) patients. However some limiting factors might result in false elevated SUVmax, such as increased macrophage infiltration, that result in false elevated SUVmax values (134) or false negative results might occur in large bulky lesions where residual vital tumor can be present, despite complete metabolic response according to the SUVmax (122). Nevertheless, a complete metabolic response in FDG PET is superior to CT volume assessment for evaluating histopathological response (125). De Geus-Oei et al analyzed the metabolic rate of glucose (MRGlu) as well as the SUV after induction chemotherapy and showed that a decrease in SUVmean of more than 35% correlated best with a favorable progression free and overall survival (135).

Recent publications focusing on FDG PET segmentation to assess total tumor burden, including metabolically active tumor volume (MTV) and total lesion glycolysis (TLG) showed superior correlation with progression free and overall survival of NSCLC compared to SUVmax (136-139). In particular, a multivariate analysis identified TLG and treatment method (surgery vs. other) to be the only two independent prognostic factors for progression free survival (140). TLG and MTV were suggested by Larson et al in 1999 to determine total tumor burden and volume using PET data (141). With the combination of CT and PET images, volume measurement via PET became less central for NSCLC, since tumor volume can be easily assessed on CT. However, with an increasing number of publications suggesting that MTV and TLG are superior in assessing NSCLC response compared to SUVmax, the question how to

measure them is relevant again (142, 143). In most of the recent studies, MTV and TLG were computed using a fixed SUVmax threshold of 40- 50% (144-146). We have recently shown that this threshold method has limitations for the measurement of lesion activity and volume: MTV and TLG based on a fixed threshold using SUVmax (e.g. 42%) will underestimate lesion's uptake with a high activity, and overestimate lesions with a SUVmax close to background (147). Other authors have used a fixed SUV threshold, most commonly SUV 2.5 (148-150), with the obvious limitations of an arbitrary cut off. Lesions with low activity are thereby underestimated or not even measurable. We have therefore developed a background based estimation method including background subtracted lesion activity (BSL), and background subtracted lesion volume (BSV) (Fig. 1).

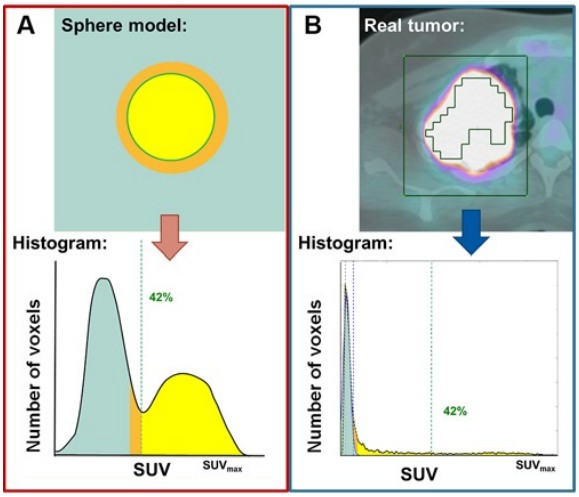

Figure 1: Illustration of both segmentation methods. (A) Using an absolute threshold of SUVmax of 42% to delineate an ideal homogeneous sphere has been shown to optimally segment the true volume of the sphere (yellow). (B) For heterogeneous real tumors however, the 42% cut off would miss a substantial number of tumor voxels (yellow), while the subtraction of the Gaussian normal distribution representing the background (green) is including all voxels with activity above background, yielding the background subtracted tumor volume (BSV).

Our method uses a single volume of interest (VOI) that surrounds the tumor and reads its histogram to measure the total activity within the lesion (147). It is based on our previously published study showing that background activity can be assessed automatically within the tumor VOI using histogram analysis (151). Since background voxels have more homogeneous

values, they will always represent the mode in a selected VOI, with a normal Gaussian distribution. Therefore, background voxels can be removed from the VOI by subtraction of a normal distribution fitted to the first peak in the histogram (147).

In this study, we wanted to test the performance of the relative change of the FDG PET tumor volume metrics MTV, TLG, BSV, and BSL in non-small cell lung carcinoma treated with neo-adjuvant chemotherapy. We chose the histopathological tumor regression grade (TRG), described by Juncker et al (105, 106) of the corresponding formalin-fixed and paraffin-embedded surgical specimens as independent reference for tumor response.

Materials and Methods

Patient selection

Patients with locally advanced stage II, stage III or oligometastatic stage IV disease underwent neo-adjuvant chemotherapy according to international guidelines following decision at our local tumor board (152). Patients must have received a FDG PET/CT scan before neoadjuvant treatment as well as before surgery between January 2002 and December 2012. This retrospective study was approved by the Ethical Commission of the Canton of Zurich and the requirement to obtain informed consent was waived. From a total of 92 NSCLC patients undergoing surgery after neo-adjuvant chemotherapy, 44 met all inclusion criteria. Most patients were diagnosed with stage III, at diagnosis. After neo-adjuvant treatment, only 3 patients showed tumors with ypT0, while ypT3 predominated. Demographic details are given in Table 1.

PET/CT acquisition and analysis

Inclusion criteria for FDG PET/CT were the following: Scans of adequate quality, patients having

been fasting for at least 4 hours, blood glucose not elevated, FDG uptake time within 45-60 minutes and FDG injection adequate (< 100 MBq difference between both FDG injections). All patients were examined using a routine clinical protocol in the Institute of Nuclear Medicine on dedicated PET/CT scanners (GE Healthcare DSTX, 16-or 64-slices CT, 7-8 frames, frame time 1.5 or 2 minutes) with injection of 350 MBq FDG 45 - 60 minutes before examination. A low dose unenhanced CT-scan was performed for attenuation correction and used for anatomical localization (80 mA, 140 kV). Image analysis was performed by a dual board certified nuclear medicine physician and radiologist (IAB), who was blinded for the results of the histopathology. A volume of interest (VOI) was placed around the primary tumor, in a way that the entire tumor activity was within the VOI, while avoiding regions of physiologically increased activity (e.g. FDG-uptake of the heart). If high activity structures cannot be avoided, they have to be cut out, prior to the analysis. VOI placement instructions were previously published (*23*). In brief, VOI size had to be slightly bigger than the tumor. For lesions with heterogeneous background (e.g. tumors abutting lung and mediastinal tissue or hilar vessels) VOIs were adjusted to make sure that more of the background tissue with higher FDG activity was included (e.g. mediastinum). Within the selected VOI SUV_{max} and MTV and TLG as well as BSL and BSV were measured. The relative change (delta = d) in FDG PET metrics before and after neo-adjuvant chemotherapy was calculated ($dSUV_{max}$, dMTV, dTLG, dBSL and dBSV). On CT, the maximal tumor diameters were measured in three dimensions (a,b,c) and tumor volume was estimated as an ellipsoid using the formula: $TVOL=4/3\pi x(a/2xb/2xc/2)$, with the corresponding relative change for CTVOL (dCTVOL) (153).

Histopathological assessment of tumor regression

For histopathologic assessment inclusion criteria were: presence of original H&E stains from

at least 2 representative whole tumor slides for regression scoring, no secondary simultaneous tumor, histologic subtype either adeno- or squamous cell carcinoma (other types were excluded). Only the primary tumors were analyzed. All H&E stains of the resection specimens manufactured for the original sign-out were entirely reviewed by RC and AS for assessment of the TRG. The TRG was scored on a 4- tiered scale based on the scoring system described by Junker et al (*24, 25*). This system evaluates the proportion of viable tumor cells in relation to the degree of tumor necrosis and fibrosis. In brief, TRG1 is defined as no or only minor, mostly spontaneous tumor regression. TRG2 shows more than 10% vital tumor tissue, whereas TRG3 includes all tumors with less than 10% vital tumor epithelia. TRG4 is complete tumor regression whereby only fibrotic and necrotic areas with macrophage-rich xanthomatous inflammation remain in the original tumor volume. For dichotomized data analysis a score of TRG1-2 was regarded as low regression and therefore patients were considered as non-responders to treatment, while patients with TRG3-4 tumors were considered as responders.

Statistical Analysis

The distribution of the relative change for all PET metrics in the different histopathological tumor regression grades was analyzed using box plots. Correlations between TRG and the different absolute and relative PET metrics $dSUV_{max}$, dMTV, dTLG, dBSL and dBSV as well as dCT_{vol} were calculated using Spearman's rank tests. A receiver operator characteristic (ROC) curve was generated for SUV_{max}, after chemotherapy and $dSUV_{max}$, dMTV, dTLG, dBSL and dBSV for TRG responders versus non-responders. The area under the curve (AUC) was calculated. The optimal cut off point for the ROC curve was determined with the Youden index, calculated as the maximum of sensitivity + specificity–1, for each cut off value (154).

Table 1: Summary of patient demographics. FDG = Fluorodeoxyglucose, cT = clinical T-stage, ypT = pathology T-stage after chemotherapy

	N	%
Patients	**44**	
Age at surgery in years (median, range)	62	(38-75)
Body weight in kg (median, range)	70	(43-123)
FDG dose in MBq (median, range)	352	(274-430)
Sex (male/female)	25/19	(56.8 / 43.2)
Histology		
Squamous cell carcinoma	23	(52.3)
Adenocarcinoma	21	(47.7)
Clinical stage at diagnosis		
II	6	(13.6)
III	35	(79.5)
IV	3	(6.8)
Tumor location		
Left lower lobe	6	(13.6)
Left upper lobe	15	(34.1)
Right lower lobe	6	(13.6)
Right middle lobe	3	(6.8)
Right upper lobe	14	(31.8)
Pathological stage after chemotherapy		
0	3	(6.8)
I	5	(11.4)
II	10	(22.7)
III	25	(56.8)
IV	1	(2.3)
CT(based cT at diagnosis		
cT1	3	(6.8)
cT2	25	(56.8)
cT3	9	(20.5)
cT4	7	(15.9)
ypT after chemotherapy		
ypT0	3	(6.8)
ypT1	5	(11.4)
ypT2	10	(22.7)
ypT3	25	(56.8)
ypT4	1	(2.3)
Chemotherapy		
Cycles (median, range)	3 (2-6)	
Platinum/Gemcitabine	17	(51.6)
Platinum/Taxane	25	(56.8)
Others	3	(6.8)

Results

In 13 patients the TRG was 3 or 4, these were thus considered as responders. Only 1 patient did not show any histologic regression (TRG1), while 30 patients had a TRG2 on histopathology. Lesions with good response to neo-adjuvant chemotherapy (TRG3-4) had a mean SUVmax of 4.2 (range: 1.8-7.9), while lesions regarded as non-responders (TRG1-2) had a mean SUVmax of 8.1 (range: 1.4-40.4). A cut off at SUVmax <6.4 after neo-adjuvant chemotherapy yielded a sensitivity and specificity of 85% and 58%, respectively to predict good pathologic response.

Differences between responders and non-responders were significant for dSUVmax (p=0.001) and dBSL and dBSV (p<0.001, respectively), while dTLG and dMTV were not significantly different between responders and non-responders (Table 2).

Table 2: Absolute values for PET metrics after chemotherapy in non-responders versus responders. *SUV = Standardized uptake value, TLG = Total lesion glycolysis, MTV = Metabolic active tumor volume, BSL = Background subtracted lesion activity, BSV = Background subtracted volume, TRG = Tumor regression grade.*

PET metrics after chemotherapy	Non-responders (TRG1-2, N = 31)				Responders (TRG3-4, N = 13)			
	Mean	Median	Min	Max	Mean	Median	Min	Max
SUVmax	8.1	7.3	1.4	40.4	4.2	4.0	1.8	7.9
TLG	59.3	38.7	6.8	229.9	41.1	45.0	9.8	76.4
MTV	13.9	9.1	1.1	43.8	23.2	15.1	5.9	69.1
BSL	82.2	32.3	0.2	344.6	22.4	9.5	1.1	76.6
BSV	19.5	9.6	0.1	82.2	6.7	3.1	0.7	20.6

Using the Spearman rank test dSUV$_{max}$ correlated with the TRG with p=0.001. PET volume metrics based on a fixed threshold of SUV$_{max}$ did not correlate with TRG (dTLG: p=0.505 and dMTV: p=0.386). However, both background activity based PET volume metrics dBSL and dBSV significantly correlated with TRG (p<0.001 for both) (Fig. 2).

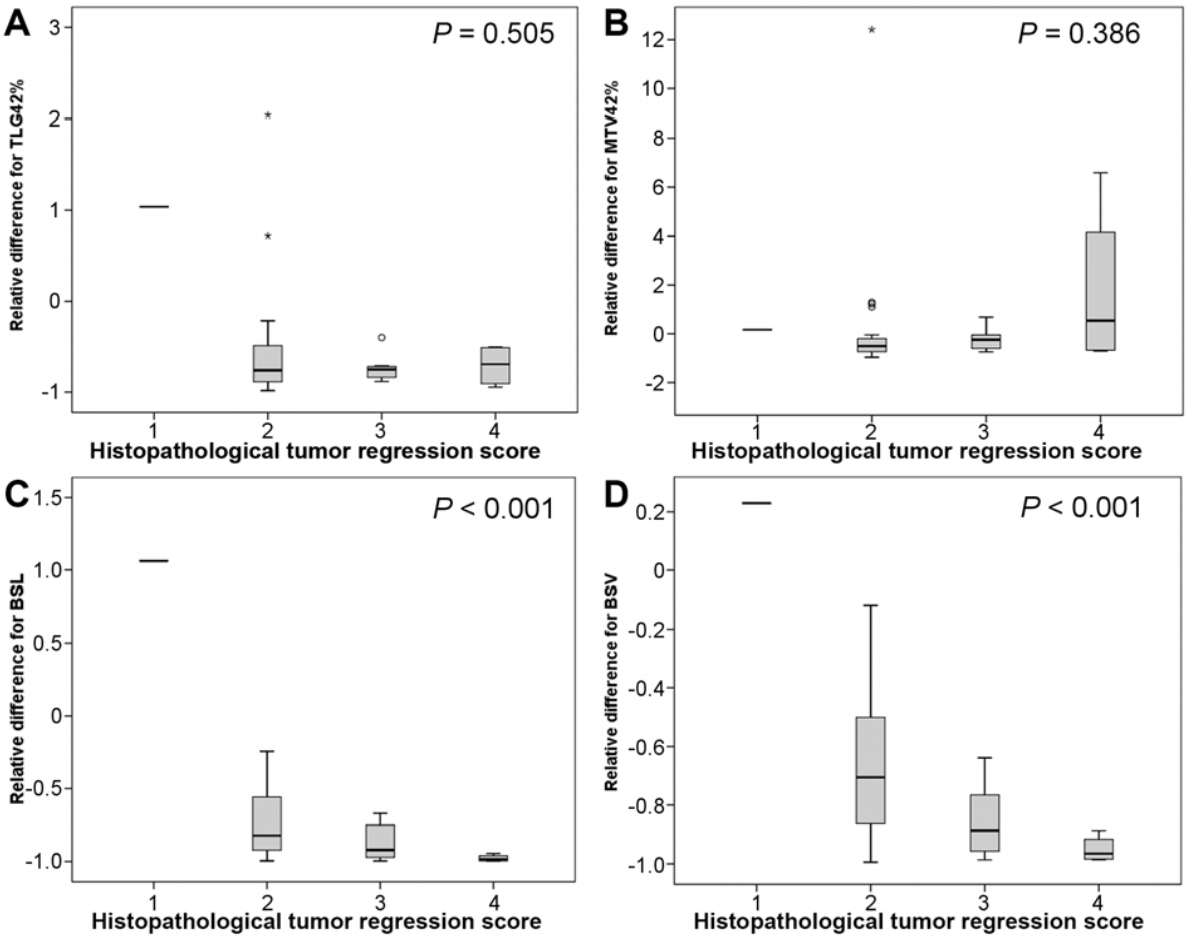

Figure 2: Boxplot illustrating that there was no correlation between TRG and the relative difference in PET volume metrics based on a fixed threshold of 42% SUVmax. (A) dTLG and (B) dMTV, while the correlation between TRG and background based metrics was significant (C) dBSL and (D) dBSV.

ROC analysis showed the largest area under the curve for BSV (AUC=0.799), followed by BSL (AUC=0.777) and SUVmax (AUC=0.767), while TLG and MTV had an AUC=0.529 and 0.387, respectively (Fig. 3).

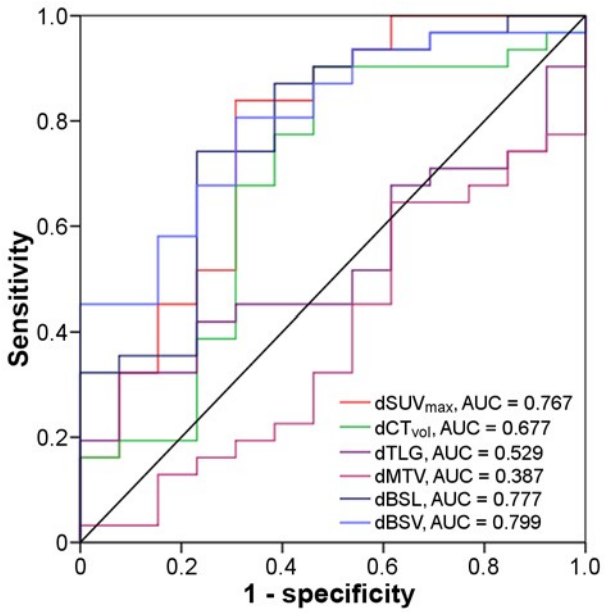

Figure 3: Receiver operator characteristic curve. ROC curve was generated for dSUVmax, dMTV, dTLG, dBSL and dBSV and TRG1-2 versus TRG3-4. BSV has the largest area under the curve (AUC=0.799), with cut off at -88% yielding a sensitivity and specificity of 69% and 81%, respectively. SUVmax and BSL are not significantly inferior with AUC=0.767 and AUC=0.777, respectively.

A cut off at -68% for dSUVmax showed a sensitivity and specificity of 69% and 84%, respectively. For dBSV a cut off at -88% gave sensitivity and specificity of 69% and 81% and for dBSL - 90% yielded a sensitivity and specificity of 77% and 74%, respectively (Table 3).

Table 3: Receiver operator characteristic curve analysis, with corresponding cut offs as well as sensitivities and specificities. SUV = Standardized uptake value, dCTvol = relative difference in CT volume, dTLG = relative difference in total lesion glycolysis, dMTV = relative difference in metabolic active tumor volume, dBSL = relative difference in background subtracted lesion activity, dBSV = relative difference in background subtracted volume, CI = confidence interval. Na = not applicable.

PET metrics	Area	Std. Error	Sig.	95% CI	Cut off	Sensitivity	Specificity
SUVmax II	0.759	0.073	0.007	0.615-0.903	6.4	85%	58%
dCTvol	0.677	0.097	0.066	0.488-0.867	-92%	54%	90%
dSUVmax	0.767	0.086	0.006	0.598-0.936	-68%	69%	81%
dTLG	0.529	0.087	0.767	0.357-0.700	na	na	na
dMTV	0.387	0.092	0.242	0.206-0.568	na	na	na
dBSL	0.777	0.080	0.004	0.620-0.934	-90%	74%	77%
dBSV	0.799	0.069	0.002	0.663-0.935	-88%	69%	84%

Figure 4 is illustrating a case of a stage IIIA central adenocarcinoma in the right hilum with high FDG-activity (SUVmax 16.1) prior to neo-adjuvant chemotherapy. After the chemotherapy a good partial metabolic response was achieved (SUV_{max} 4.9, -70%). However, MTV decreased only minimally form 22.2 to 18.4 cm^3 (-17%) while BSV decreased substantially from 55.2 to 2.4 cm^3 (-96%). Histopathology showed extensive fibroelastotic scar tissue with small residual foci of vital adenocarcinoma growing in lepidic fashion along the alveolar walls, corresponding to TRG 3 (Fig. 5).

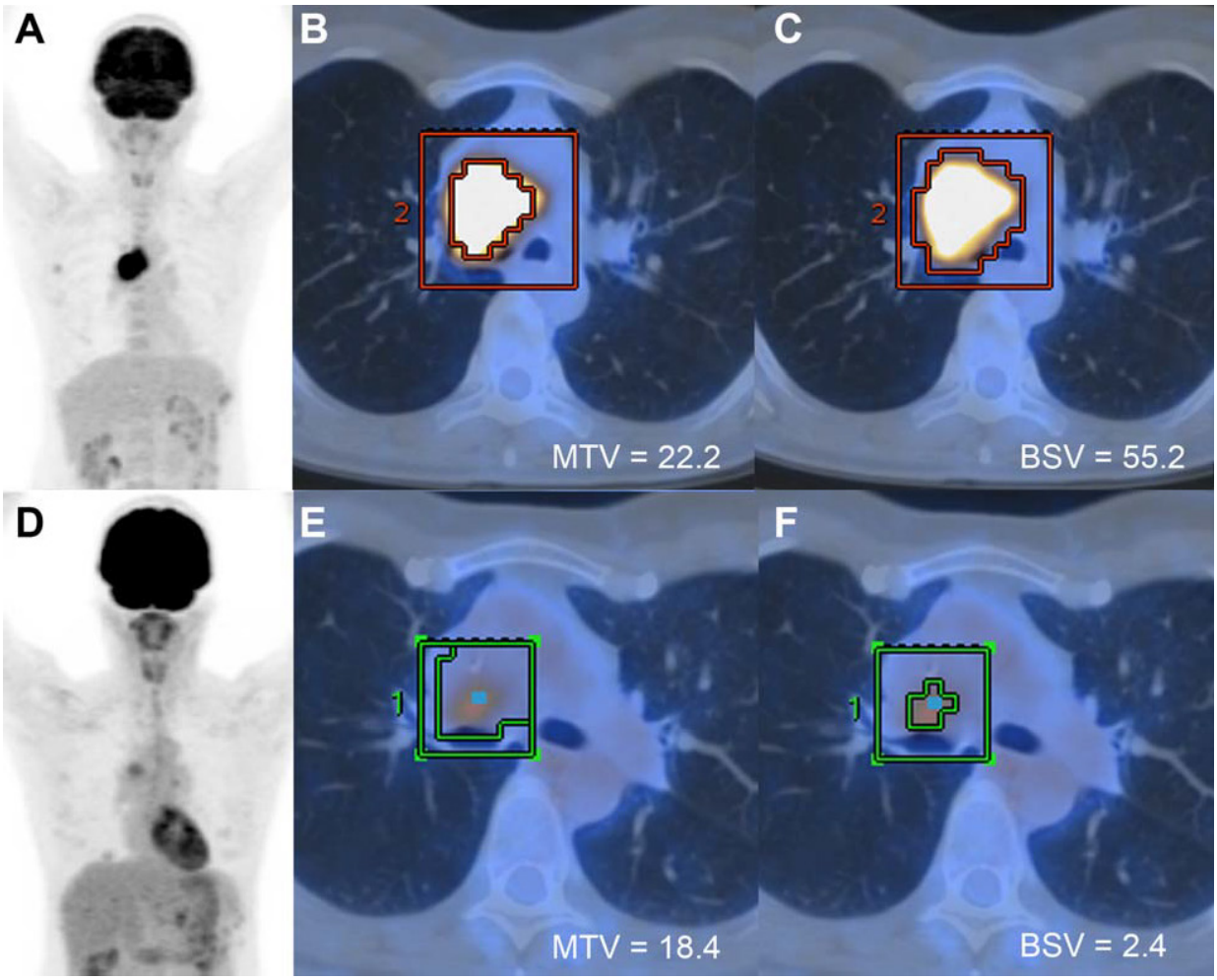

Figure 4: 52 year old woman, treated with cisplatin/pemetrexed based neo-adjuvant chemotherapy for a stage IIIA central adenocarcinoma in the right hilum (SUVmax 16.1). (A-C) Staging FDG PET/CT with (A) coronal MIP overview and (B-C) axial fused PET/CT with a tumor VOI around the lesion, illustrating that MTV gives a significantly lower volume compared to BSV in a lesion with high activity. (D-F) Restaging FDG PET/CT after 3 cycles of chemotherapy with a significant decrease in (SUVmax 4.9), correlating with a TRG3. While BSV decreased by 96%, MTV only decreased by 17% not entirely reflecting the good tumor response.

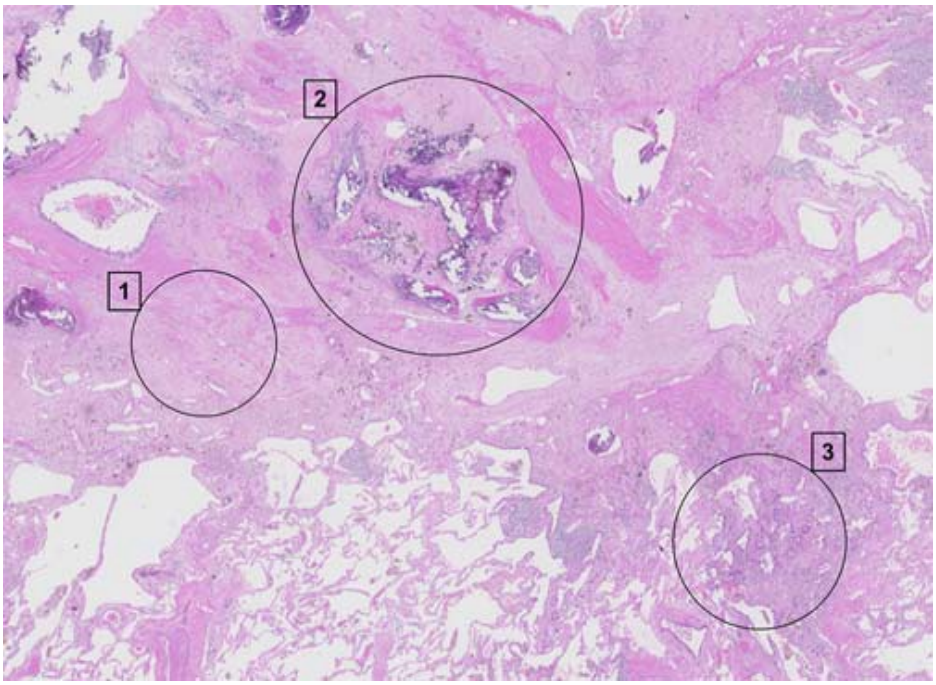

Figure 5: Corresponding histologic whole section for the patient in figure 4 with a TRG3. (1) Extensive fibroelastotic scar tissue after neo-adjuvant chemotherapy (partial response) and normal, partially emphysematic lung (bottom left). (2) Central tumor part consisting of larger calcifications, heavy elastosis with complete vessel remodeling and enclosed anthracotic pigment. (3) Small residual focus of vital adenocarcinoma growing in lepidic fashion along the alveolar walls. Original magnifications 10x, H&E stains.

Discussion

Our results show that SUVmax after neo-adjuvant chemotherapy can distinguish "responders" from "non-responders", with a high sensitivity of 85%, however with a rather low specificity of 58%. The relative change in SUVmax (dSUVmax) is associated with tumor regression and a cut off at -68% predicts good to complete tumor regression with a specificity of 81% (TRG3-4). This is in line with previous studies, suggesting that a decrease in SUVmax is associated with good tumor response (155-157). One study investigated the relation between quantitative FDG metrics with pathologic tumor response and showed a linear relation between change in SUVmax and the percentage of nonviable tumor (124). They also came to the conclusion that metabolic parameters were superior compared to CT morphology for response assessment. This is in concordance with our results, showing that a decrease in dCTvol is yielding an AUC

of 0.677, compared to dSUVmax with 0.767 or dBSL with 0.799.

An increasing number of studies are using SUV>2.5 as an absolute threshold (TLG2.5 or MTV2.5), especially for segmentation of lung tumors (148-150). In our cohort, one adenocarcinoma had an activity of SUVmax 2.4 before chemotherapy, which would not have been measurable with TLG2.5 or MTV2.5.

Moreover, this adenocarcinoma decreased in BSL and BSV only by 50 and 60%, respectively, suggesting only partial metabolic response, which was confirmed by histopathology (TRG2). Furthermore, 8 lesions had a SUVmax<2.5 after chemotherapy, but only 4 were complete responders, of these 4 non-responding lesions, BSL and BSV suggested complete response only in one case.

Previously published papers suggest that PET volume metrics such as MTV and TLG are superior to SUVmax for prediction of overall and progression free survival. However, MTV and TLG based on a fixed threshold (SUVmax 42%) failed to predict histopathological response in the current study, while the background adapted segmentation methods correlated with TRG. This might be explained with phantom results showing that a fixed threshold can lead to a substantial underestimation of TLG and MTV for lesions with high FDG uptake (147). A decrease of SUVmax under therapy therefore might lead to a false increase in MTV since a larger volume of less active tumor will be included into MTV. This is illustrated in Figure 4 with FDG PET/CT exams before and after neo-adjuvant chemotherapy, where MTV overestimates the volume after therapy, while BSV shows a good response. Histopathology confirmed tumor regression with TRG3 (Fig. 5).

Also the original paper from Erdi et al, suggested that PET tumor segmentation requires an adapted threshold based on the tumor-to-background ratio (158). Drawing a separate VOI

over background for every lesion is time consuming especially in patients with multiple metastases. Therefore, we suggest our histogram based one-step method to measure tumor activity and to estimate the volume. For tumor volume definition before radiotherapy planning however, background based tumor segmentation has already been suggested previously with a separate VOI drawn over the background area by Nestle et al (159). Others further investigate histogram indices such as standard deviation, skewness, kurtosis, entropy and energy, however results are still controversial and those metrics were not part of the current study (160).

In the present study, dSUVmax was not significantly inferior to dBSL and dBSV for prediction of tumor regression. This might reflect the importance of the most aggressive part within a tumor reflected by the highest SUV values, as compared to the metabolically active tumor volume. This will need further investigation in larger cohorts.

The study has several limitations. The retrospective nature of the analysis leads to some inconsistencies in uptake time, and the injected FDG dose varied over time. Care was taken to exclude patients with high blood sugar, paravenous injection or scan artifacts (motion, metal implants). In addition, the chosen patient cohort represents a real patient population within the selected clinical setting and quantification measures should be reliable in such a setting, too. Also, we did not perform outcome analysis on the present patient population; we investigated the direct correlation between PET quantification and histopathology and believe that this patient population is too small and heterogeneous (stage, therapy, histology) to assess a meaningful correlation with progression free and overall survival. Therefore, follow up projects with larger homogeneous patient cohorts that underwent primary surgery without neo-adjuvant chemotherapy are planned. BSL and BSV are not intended to serve as a PET segmentation tool, since space information is lost in the histogram, and therefore selected

voxels do not have a one-to-one correspondence to the voxels in the images. BSV therefore may not provide an accurate segmentation of the tumor boundary, as is necessary for radiation therapy planning. The subtraction of background activity from the tumor VOI will represent the true BSL as the entire amount of activity coming from the tumor, irrespective of the location, i.e. it includes spill-out or spill-over. As a result, for delineation of tumor volume, a spill-over correction would be necessary and was not performed in this study, since we were interested in the relative change of the total activity/volume and not the boundary. The threshold at 42% of SUV_{max} suggested by Erdi can only be applied for homogeneous spheres with high lesion-to-background ratios (158). The heterogeneous nature of real tumors might be better reflected by the 15% of the average activity plus background, suggested by Nestle et al to delineate the tumor area for radiotherapy (159). For tumor burden assessment in oncology imaging the fact that spillover is regarded as a part of tumor volume might only weakly affect the accuracy of the overall assessment. This is suggested by the fact that BSV and BLS showed very similar correlation to TRG, while MTV and TLG did not.

Conclusion

The current data confirm that PET volume metrics based on a fixed threshold (42% SUV_{max}) lead to a significant bias and do not correlate with response to chemotherapy assessed on histopathology. PET volume metrics based on background-adapted measurements however, correlate with tumor regression.

Chapter 5

Discussion and conclusions

This doctoral thesis describes an image-based computational approach aiming at refining morphologic classification of lung squamous cell carcinoma. The presented study provides evidence that automatic image analysis can provide an accurate quantification of morphological parameters, potentially useful to build novel and prognostic classification systems. The field of pathology is facing dramatic changes since the popularisation and recognition of whole slide imaging (WSI) systems for the review of digital surgical pathology slides. The digitalization of whole tissue specimens has led to an incentive to develop automatic methods to support pathologic decision. Consequently, multitude of methods have been proposed to quantify morphological parameters in histopathological images (58, 161).

Histologic revision of tissue sections is the essence of histopathologic disease classification. Since decades, pathologists have been using light microscopy to examine and extract meaningful parameters for the morphology of formalin-fixed tissue specimens or to evaluate the positivity of a given diagnostic marker (162). Because of this fixation method and the use of H&E and other chromogenic dyes, tissue specimens show extremely high longevity, which considerably facilitates retrospective studies. Among the popular dyes, diaminobenzidine (DAB) is a chromogenic IHC staining method resulting in a typical brown staining (163). Although practical for the above-mentioned reasons, this stain is not suitable for strictly quantitative intensity scoring, as most of the light is not emitted in contrast to immunofluorescence (164). Whereas most applications require a binary interpretation of the staining positivity, semi-quantitative assessments might also be required with implications for treatment decision.

Hence, precise readouts are often required for accurate disease status reporting, despite the limitations of human judgment. In immunohistochemistry-based testing, pathologists have to deliberate whether a tumor is expressing a given threshold percentage of positivity. For example, breast cancers showing HER2 (Receptor tyrosine-protein kinase erbB-2) overexpression can be treated using anti-HER2 drugs such as Trazumab or Lapatinib (165). An IHC test using the following scale can be used to determine HER2 expression (166) : 0 (negative), 1+ (also negative), 2+ (borderline), or 3+ (positive). However, this scoring method might be rather ambiguous (167) which would require fluorescence in situ hybridization (FISH) to confirm HER2-positivity (168, 169). Another representative pitfall can be shown for NSCLC, where the percentage of PD-L1 expressing tumor cells is a marker for immunotherapy efficacy. In the case of Pembrolizumab, patients with PD-L1 expression in at least 50% of tumor cells had a significantly better response to the treatment (44). However, drawing a line over a given score threshold cannot be humanly done without reliable quantitative tools other than subjective judgment or experience. For obvious reasons, the development of companion diagnostic tools to unify such quantitative measurements could have a significant impact on future clinical decisions.

IHC evaluation is not only restricted to disease diagnostics but is also an important part of tissue biomarkers research (170). Biomarker studies often use semi-quantitative scales to evaluate the expression level of a given protein. In practice, the percentage of positive tumor cells, the intensity of the staining and an integrative H-score are commonly used to describe the expression level of a given biomarker (171). However, the manual evaluation of frequency or intensity levels is highly subjective and is prone to inter-observer variability (169). While the use of computerized methods does not seem to be a necessity to determine if a tumor is

immunoreactive for a given diagnostic marker, automatic evaluation of tissue samples can considerably decrease the time spent on routine tasks.

Disease classification is another part of daily routine in pathology, whereby tumor stage is the best prognosticator and hence will decide upon disease treatment. For lung cancer, this system evaluates the extent of the disease by measuring the primary tumor and evaluating the presence the lymph node or distant metastasis (TNM staging) (21). Tumor size and location is the only determinant parameter for pathologic T (pT). However, in lung squamous cell carcinoma, it has been shown that histologic features can carry prognostic information (53-56). Therefore, another field of digital pathology is the discovery of prognostic markers able to stratify tumors into prognostic groups. A common approach relies on the extraction of cell or nuclear shape descriptors or features (161). This approach has shown to provide prognostic information for NSCLC (62, 63). However, accurate cell segmentation of H&E stained sections is complex and features extracted are highly dependent on the quality of image segmentation. Deep learning algorithms are increasingly popular for image classification as they allow unsupervised feature learning, which is particularly powerful for pattern recognition on histologic sections (172). Examples of histopathologic features detection using convolutional neural networks include cancer cell nuclei (173, 174), mitosis detection (175, 176), tumor grading (177) and metastasis detection (64).

In our study, we proposed an alternative approach to evaluate higher-level structures related to the overall tumor microarchitecture. A high contrast between tumor tissue and its surrounding stroma could be achieved using AE1/AE3 IHC, which is specific to epithelial cells. As shown previously, such an approach can reliably segment lung cancer tissue from its surrounding stroma (109, 178). Therefore, analyzing connected epithelial tumor elements rather than individual cells might reflect better the overall invasion pattern of solid carcinomas,

generally depicted as collective cell migration (82, 83). In chapter 2, we hypothesized that the amount of tumor clusters would be a marker of tumor invasiveness as several studies suggested that the presence of small clusters or buds are prognostic (budding and sheets). Nevertheless, these structures may represent two-dimensional projections of the 3D branching of the tumor (101). Instead of focusing on small clusters, we included an overall fragmentation independently of cluster size. The integration of molecular data showed that several biological processes, mostly related to extracellular matrix remodeling and cell invasion were upregulated, thus suggesting that the presence of high amount of fragments indicates tumor invasion. In this first study, we used an intuitive and understandable parameter to provide a basis grading scoring applicable in pathology. However, a more comprehensive analysis could be performed by extracting multiple shape descriptors. This data could further be used to estimate automatically the potential risk given the overall tumor morphology. This hypothesis would be ideally followed-up in further studies but would require a validation set to test such model.

Although surgical resection is the most common procedure for intended curation, additional chemotherapy or radiotherapy treatment can be given in a neoadjuvant setting, in order to reduce the tumor burden before marginal resection of the tumor (152, 179). The radiologic evaluation post-treatment is an important step to guide further treatment. This is mainly achieved following response criteria (RECIST) which is a metric of radiologic response (180). The metabolic activity of the tumor measured by PET, as standardized uptake value is an imaging method especially helpful to detect metastases (17). However, these imaging methods are not specific enough, and would require histopathologic confirmation (19).

On a daily practice, tumor size is an essential parameter for TNM staging. However, after neoadjuvant treatment, the measurement of residual tumor burden can be cumbersome as

microscopic tumor islands may remain. Several studies have proposed regression systems for NSCLC, based on the amount of residual tumor tissue (105, 107-109). Nevertheless, most studies rely on manual measurements or the remaining tumor burden on H&E stained tissue. In chapter 3, we have extended our computerized method to a patient cohort, having received neoadjuvant chemotherapy. Once again, we have used intuitive parameters related to the remaining tumor burden. We have demonstrated that the automatic scores were performing better than manual assessment of tumor regression, which highlights the significance of using automated methods to support pathologic diagnostic. In addition, we have shown in this Chapter 3 and 4 that not all PET measurements correlate with histologic tumor burden. Therefore, a careful selection of PET parameters should be done before trying to address the tumor response to treatment.

In conclusion, in this doctoral thesis, we provided evidence that the use of image-based computational methods is a reliable approach to supervise pathologists for disease classification. We have proposed an approach for accurate quantification of morphological parameters of lung squamous cell carcinomas, which could provide a solid basis for building novel classification systems.

Acknowledgements

I sincerely thank Prof. Alex Soltermann for his encouragement and support during my PhD thesis, for his trust and confidence throughout my stay at the University Hospital Zurich, allowing me to work in both a multidisciplinary and socially welcoming environment. I am grateful that he shared his passion for human clinical research with me, which I definitely wish to continue in the future.

I express my gratitude to my thesis committee members for their kind and very helpful advice during the past years. I would like to start by thanking Prof. Bernd Bodenmiller for holding the position of official supervisor as well as for his guidance and pertinent help. His expertise in proteomics was greatly relevant particularly when conducting Mass Spectrometry experiments. Secondly, I would like to thank Prof. Renato Pajarola, with whom I had the pleasure to collaborate with on a project allowing me to share enjoyable moments with his students Rafael Ballester and Reto Wettstein, who worked on the 3D modelling of lung squamous cell carcinoma. I am thankful to Prof. Holger Moch, our director of the Institute of Pathology and Molecular Pathology, for his unreserved support and guidance through my project. His expertise was greatly appreciated and provided guidance when faced with clinically relevant questions. I am also grateful to him for making all of us feel part of the pathology family notably during those summer and winter celebrations, always with a hint of humour.

This doctoral work could not have been conceived without the helpful expertise of all the people that made our collaborations possible. Therefore, I would like to acknowledge PD Dr. Irene Burger for her work on PET/CT imaging, the Paul Sherrer Institute alumni and staff : Dr. Alberto Astolfo and Prof. Dr. Marco Stampanoni for making the 3D tumor imaging possible, the Functional Genomics Center staff, in particular Dr. Paolo Nanni and Dr. Jonas Grossmann who

guided me throughout my proteomics experiments, Prof. Andrew Beck from the Beth Israel Deaconess Medical Center and Harvard Medical School Boston and Dr. Daniel Xia from the Massachusetts General Hospital whom expertise in computational image analysis was crucial when conducting our morphometric analysis.

Additionally, this project would not have been possible without the unconditional help of the entire University Hospital Zurich, notably the Biobank staff especially Susanne Dettwiler, Fabiola Prutek and Martina Storz and the IT support team, in particular Monika Bieri, Norbert Wey and André Wethmar. I would like to thank Dr. Peter Schraml and his lab members Adriana von Teichman, Aashil Batavia, Hella Bolck, Magdalena Lukamowicz, Raquel Herrador, Silvia Angori as well as Claudia Corró as well as Prof. Peter Wild's lab members, notably Nadejda Valtcheva for her help as well as Elisa Bellini, Christine Fritz, Kathrin Oehl, Markus Rechsteiner, Ulrich Wagner, and Qing Zhong for all the thrilling discussions inside and outside the lab.

I am grateful to the Life Sciences Graduate School and Cancer Biology Program, for allowing me to share my research with other PhD students and Professors in a stimulating and pleasant way.

I would also like to thank the Swiss Cancer League who provided the financial support of my PhD work.

Finally, it was my pleasure to work in a friendly environment, which can be attributed to the great colleagues and friends that I was fortunate enough to work with, in particular Anne-Laure Leblond for kindly reviewing the misprints, Chengguang Wu, Karina Silina, Undine Rulle, formerly Aditya Kashyap and Elisa Bianchi with all of whom I shared beautiful moments inside and outside the lab. A special thanks to Karina again, who always shared her knowledge and time with me. I am also grateful to my family and friends who provided me a healthy and stable life environment and helped me enjoy every bit of my student life.

References

1. Ferlay J, Soerjomataram I, Dikshit R, Eser S, Mathers C, Rebelo M, et al. Cancer incidence and mortality worldwide: sources, methods and major patterns in GLOBOCAN 2012. Int J Cancer. 2015;136(5):E359-86.

2. Parkin DM, Bray F, Ferlay J, Pisani P. Global cancer statistics, 2002. CA Cancer J Clin. 2005;55(2):74-108.

3. Brownson RC, Alavanja MC, Caporaso N, Simoes EJ, Chang JC. Epidemiology and prevention of lung cancer in nonsmokers. Epidemiol Rev. 1998;20(2):218-36.

4. Baan R, Grosse Y, Straif K, Secretan B, El Ghissassi F, Bouvard V, et al. A review of human carcinogens--Part F: chemical agents and related occupations. Lancet Oncol. 2009;10(12):1143-4.

5. Secretan B, Straif K, Baan R, Grosse Y, El Ghissassi F, Bouvard V, et al. A review of human carcinogens--Part E: tobacco, areca nut, alcohol, coal smoke, and salted fish. Lancet Oncol. 2009;10(11):1033-4.

6. El Ghissassi F, Baan R, Straif K, Grosse Y, Secretan B, Bouvard V, et al. A review of human carcinogens--part D: radiation. Lancet Oncol. 2009;10(8):751-2.

7. Straif K, Benbrahim-Tallaa L, Baan R, Grosse Y, Secretan B, El Ghissassi F, et al. A review of human carcinogens--Part C: metals, arsenic, dusts, and fibres. Lancet Oncol. 2009;10(5):453-4.

8. Bouvard V, Baan R, Straif K, Grosse Y, Secretan B, El Ghissassi F, et al. A review of human carcinogens--Part B: biological agents. Lancet Oncol. 2009;10(4):321-2.

9. Grosse Y, Baan R, Straif K, Secretan B, El Ghissassi F, Bouvard V, et al. A review of human carcinogens--Part A: pharmaceuticals. Lancet Oncol. 2009;10(1):13-4.

10. Arndt V FA, Hauri D, Heusser R, Junker C, Kuehni C, et al. Swiss Cancer Report 2015. NICER, Federal Statistical Office (FSO), National Institute for Cancer Epidemiology and Registration (NICER) Swiss Childhood Cancer Registry (SCCR). 2015.

11. Francisci S, Minicozzi P, Pierannunzio D, Ardanaz E, Eberle A, Grimsrud TK, et al. Survival patterns in lung and pleural cancer in Europe 1999-2007: Results from the EUROCARE-5 study. Eur J Cancer. 2015.

12. Sun S, Schiller JH, Gazdar AF. Lung cancer in never smokers--a different disease. Nat Rev Cancer. 2007;7(10):778-90.

13. Sutherland KD, Proost N, Brouns I, Adriaensen D, Song JY, Berns A. Cell of origin of small cell lung cancer: inactivation of Trp53 and Rb1 in distinct cell types of adult mouse lung. Cancer Cell. 2011;19(6):754-64.

14. Sutherland KD, Berns A. Cell of origin of lung cancer. Mol Oncol. 2010;4(5):397-403.

15. Silvestri GA, Gonzalez AV, Jantz MA, Margolis ML, Gould MK, Tanoue LT, et al. Methods for staging non-small cell lung cancer: Diagnosis and management of lung cancer, 3rd ed: American College of Chest Physicians evidence-based clinical practice guidelines. Chest. 2013;143(5 Suppl):e211S-e50S.

16. Rivera MP, Mehta AC, Wahidi MM. Establishing the diagnosis of lung cancer: Diagnosis and management of lung cancer, 3rd ed: American College of Chest Physicians evidence-based clinical practice guidelines. Chest. 2013;143(5 Suppl):e142S-e65S.

17. Schrevens L, Lorent N, Dooms C, Vansteenkiste J. The role of PET scan in diagnosis, staging, and management of non-small cell lung cancer. Oncologist. 2004;9(6):633-43.

18. Fischer B, Lassen U, Mortensen J, Larsen S, Loft A, Bertelsen A, et al. Preoperative staging of lung cancer with combined PET-CT. N Engl J Med. 2009;361(1):32-9.

19. Schmidt-Hansen M, Baldwin DR, Hasler E, Zamora J, Abraira V, Roque IFM. PET-CT for assessing mediastinal lymph node involvement in patients with suspected resectable non-small cell lung cancer. Cochrane Database Syst Rev. 2014(11):CD009519.

20. Crino L, Weder W, van Meerbeeck J, Felip E, Group EGW. Early stage and locally advanced (non-metastatic) non-small-cell lung cancer: ESMO Clinical Practice Guidelines for diagnosis, treatment and follow-up. Ann Oncol. 2010;21 Suppl 5:v103-15.

21. Travis WD, Brambilla E, Nicholson AG, Yatabe Y, Austin JH, Beasley MB, et al. The 2015 World Health Organization Classification of Lung Tumors: Impact of Genetic, Clinical and Radiologic Advances Since the 2004 Classification. J Thorac Oncol. 2015;10(9):1243-60.

22. Reck M, Heigener DF, Mok T, Soria JC, Rabe KF. Management of non-small-cell lung cancer: recent developments. Lancet. 2013;382(9893):709-19.

23. Scagliotti GV, Parikh P, von Pawel J, Biesma B, Vansteenkiste J, Manegold C, et al. Phase III study comparing cisplatin plus gemcitabine with cisplatin plus pemetrexed in chemotherapy-naive patients with advanced-stage non-small-cell lung cancer. J Clin Oncol. 2008;26(21):3543-51.

24. Sandler A, Gray R, Perry MC, Brahmer J, Schiller JH, Dowlati A, et al. Paclitaxel-carboplatin alone or with bevacizumab for non-small-cell lung cancer. N Engl J Med. 2006;355(24):2542-50.

25. Thomas A, Liu SV, Subramaniam DS, Giaccone G. Refining the treatment of NSCLC according to histological and molecular subtypes. Nat Rev Clin Oncol. 2015;12(9):511-26.

26. Paez JG, Janne PA, Lee JC, Tracy S, Greulich H, Gabriel S, et al. EGFR mutations in lung cancer: correlation with clinical response to gefitinib therapy. Science. 2004;304(5676):1497-500.

27. Lynch TJ, Bell DW, Sordella R, Gurubhagavatula S, Okimoto RA, Brannigan BW, et al. Activating mutations in the epidermal growth factor receptor underlying responsiveness of non-small-cell lung cancer to gefitinib. N Engl J Med. 2004;350(21):2129-39.

28. Pao W, Miller V, Zakowski M, Doherty J, Politi K, Sarkaria I, et al. EGF receptor gene mutations are common in lung cancers from "never smokers" and are associated with sensitivity of tumors to gefitinib and erlotinib. Proc Natl Acad Sci U S A. 2004;101(36):13306-11.

29. Soda M, Choi YL, Enomoto M, Takada S, Yamashita Y, Ishikawa S, et al. Identification of the transforming EML4-ALK fusion gene in non-small-cell lung cancer. Nature. 2007;448(7153):561-6.

30. Koivunen JP, Mermel C, Zejnullahu K, Murphy C, Lifshits E, Holmes AJ, et al. EML4-ALK fusion gene and efficacy of an ALK kinase inhibitor in lung cancer. Clin Cancer Res. 2008;14(13):4275-83.

31. Takeuchi K, Choi YL, Soda M, Inamura K, Togashi Y, Hatano S, et al. Multiplex reverse transcription-PCR screening for EML4-ALK fusion transcripts. Clin Cancer Res. 2008;14(20):6618-24.

32. Wong DW, Leung EL, So KK, Tam IY, Sihoe AD, Cheng LC, et al. The EML4-ALK fusion gene is involved in various histologic types of lung cancers from nonsmokers with wild-type EGFR and KRAS. Cancer. 2009;115(8):1723-33.

33. Inamura K, Takeuchi K, Togashi Y, Hatano S, Ninomiya H, Motoi N, et al. EML4-ALK lung cancers are characterized by rare other mutations, a TTF-1 cell lineage, an acinar histology, and young onset. Mod Pathol. 2009;22(4):508-15.

34. Kwak EL, Bang YJ, Camidge DR, Shaw AT, Solomon B, Maki RG, et al. Anaplastic lymphoma kinase inhibition in non-small-cell lung cancer. N Engl J Med. 2010;363(18):1693-703.

35. Lovly C HL, Pao W. Molecular Profiling of Lung Cancer. My Cancer Genome. 2016; https://www.mycancergenome.org/content/disease/lung-cancer/.

36. Camidge DR, Pao W, Sequist LV. Acquired resistance to TKIs in solid tumours: learning from lung cancer. Nat Rev Clin Oncol. 2014;11(8):473-81.

37. Holohan C, Van Schaeybroeck S, Longley DB, Johnston PG. Cancer drug resistance: an evolving paradigm. Nat Rev Cancer. 2013;13(10):714-26.

38. Jackman D, Pao W, Riely GJ, Engelman JA, Kris MG, Janne PA, et al. Clinical definition of acquired resistance to epidermal growth factor receptor tyrosine kinase inhibitors in non-small-cell lung cancer. J Clin Oncol. 2010;28(2):357-60.

39. Balak MN, Gong Y, Riely GJ, Somwar R, Li AR, Zakowski MF, et al. Novel D761Y and common secondary T790M mutations in epidermal growth factor receptor-mutant lung adenocarcinomas with acquired resistance to kinase inhibitors. Clin Cancer Res. 2006;12(21):6494-501.

40. Yu HA, Arcila ME, Rekhtman N, Sima CS, Zakowski MF, Pao W, et al. Analysis of tumor specimens at the time of acquired resistance to EGFR-TKI therapy in 155 patients with EGFR-mutant lung cancers. Clin Cancer Res. 2013;19(8):2240-7.

41. Hanahan D, Weinberg RA. Hallmarks of cancer: the next generation. Cell. 2011;144(5):646-74.

42. Pardoll DM. The blockade of immune checkpoints in cancer immunotherapy. Nat Rev Cancer. 2012;12(4):252-64.

43. Schreiber RD, Old LJ, Smyth MJ. Cancer immunoediting: integrating immunity's roles in cancer suppression and promotion. Science. 2011;331(6024):1565-70.

44. Garon EB, Rizvi NA, Hui R, Leighl N, Balmanoukian AS, Eder JP, et al. Pembrolizumab for the treatment of non-small-cell lung cancer. N Engl J Med. 2015;372(21):2018-28.

45. Herbst RS, Baas P, Kim DW, Felip E, Perez-Gracia JL, Han JY, et al. Pembrolizumab versus docetaxel for previously treated, PD-L1-positive, advanced non-small-cell lung cancer (KEYNOTE-010): a randomised controlled trial. Lancet. 2016;387(10027):1540-50.

46. Reck M, Rodriguez-Abreu D, Robinson AG, Hui R, Csoszi T, Fulop A, et al. Pembrolizumab versus Chemotherapy for PD-L1-Positive Non-Small-Cell Lung Cancer. N Engl J Med. 2016;375(19):1823-33.

47. Zugazagoitia J, Enguita AB, Nunez JA, Iglesias L, Ponce S. The new IASLC/ATS/ERS lung adenocarcinoma classification from a clinical perspective: current concepts and future prospects. J Thorac Dis. 2014;6(Suppl 5):S526-36.

48. Lee HY, Jeong JY, Lee KS, Yi CA, Kim BT, Kang H, et al. Histopathology of lung adenocarcinoma based on new IASLC/ATS/ERS classification: prognostic stratification with functional and metabolic imaging biomarkers. J Magn Reson Imaging. 2013;38(4):905-13.

49. Murakami S, Ito H, Tsubokawa N, Mimae T, Sasada S, Yoshiya T, et al. Prognostic value of the new IASLC/ATS/ERS classification of clinical stage IA lung adenocarcinoma. Lung Cancer. 2015;90(2):199-204.

50. Russell PA, Barnett SA, Walkiewicz M, Wainer Z, Conron M, Wright GM, et al. Correlation of mutation status and survival with predominant histologic subtype according to the new IASLC/ATS/ERS lung adenocarcinoma classification in stage III (N2) patients. J Thorac Oncol. 2013;8(4):461-8.

51. Yanagawa N, Shiono S, Abiko M, Ogata SY, Sato T, Tamura G. New IASLC/ATS/ERS classification and invasive tumor size are predictive of disease recurrence in stage I lung adenocarcinoma. J Thorac Oncol. 2013;8(5):612-8.

52. Zhao ZR, Xi SY, Li W, Situ DR, Chen KM, Yang H, et al. Prognostic impact of pattern-based grading system by the new IASLC/ATS/ERS classification in Asian patients with stage I lung adenocarcinoma. Lung Cancer. 2015;90(3):604-9.

53. Kadota K, Nitadori J, Woo KM, Sima CS, Finley DJ, Rusch VW, et al. Comprehensive pathological analyses in lung squamous cell carcinoma: single cell invasion, nuclear diameter, and tumor budding are independent prognostic factors for worse outcomes. J Thorac Oncol. 2014;9(8):1126-39.

54. Weichert W, Kossakowski C, Harms A, Schirmacher P, Muley T, Dienemann H, et al. Proposal of a prognostically relevant grading scheme for pulmonary squamous cell carcinoma. Eur Respir J. 2016;47(3):938-46.

55. Masuda R, Kijima H, Imamura N, Aruga N, Nakamura Y, Masuda D, et al. Tumor budding is a significant indicator of a poor prognosis in lung squamous cell carcinoma patients. Mol Med Rep. 2012;6(5):937-43.

56. Takahashi Y, Ishii G, Taira T, Fujii S, Yanagi S, Hishida T, et al. Fibrous stroma is associated with poorer prognosis in lung squamous cell carcinoma patients. J Thorac Oncol. 2011;6(9):1460-7.

57. Bauer TW, Schoenfield L, Slaw RJ, Yerian L, Sun Z, Henricks WH. Validation of whole slide imaging for primary diagnosis in surgical pathology. Arch Pathol Lab Med. 2013;137(4):518-24.

58. Gurcan MN, Boucheron LE, Can A, Madabhushi A, Rajpoot NM, Yener B. Histopathological image analysis: a review. IEEE Rev Biomed Eng. 2009;2:147-71.

59. Camp RL, Chung GG, Rimm DL. Automated subcellular localization and quantification of protein expression in tissue microarrays. Nat Med. 2002;8(11):1323-7.

60. Turbin DA, Leung S, Cheang MC, Kennecke HA, Montgomery KD, McKinney S, et al. Automated quantitative analysis of estrogen receptor expression in breast carcinoma does not differ from expert pathologist scoring: a tissue microarray study of 3,484 cases. Breast Cancer Res Treat. 2008;110(3):417-26.

61. Beck AH, Sangoi AR, Leung S, Marinelli RJ, Nielsen TO, van de Vijver MJ, et al. Systematic analysis of breast cancer morphology uncovers stromal features associated with survival. Sci Transl Med. 2011;3(108):108ra13.

62. Yu KH, Zhang C, Berry GJ, Altman RB, Re C, Rubin DL, et al. Predicting non-small cell lung cancer prognosis by fully automated microscopic pathology image features. Nat Commun. 2016;7:12474.

63. Luo X, Zang X, Yang L, Huang J, Liang F, Rodriguez-Canales J, et al. Comprehensive Computational Pathological Image Analysis Predicts Lung Cancer Prognosis. J Thorac Oncol. 2017;12(3):501-9.

64. Litjens G, Sanchez CI, Timofeeva N, Hermsen M, Nagtegaal I, Kovacs I, et al. Deep learning as a tool for increased accuracy and efficiency of histopathological diagnosis. Sci Rep. 2016;6:26286.

65. Hershkovitz T, Shenhav A, Sabo E, Ben-Izhak O, Hershkovitz D. Development of a computerized morphometry application for assessment of the tumor fraction in colon carcinoma tissue samples. Appl Immunohistochem Mol Morphol. 2013;21(1):54-8.

66. Casanova R, Xia D, Rulle U, Nanni P, Grossmann J, Vrugt B, et al. Morphoproteomic Characterization of Lung Squamous Cell Carcinoma Fragmentation, a Histological Marker of Increased Tumor Invasiveness. Cancer Res. 2017;77(10):2585-93.

67. Koelzer VH, Zlobec I, Berger MD, Cathomas G, Dawson H, Dirschmid K, et al. Tumor budding in colorectal cancer revisited: results of a multicenter interobserver study. Virchows Arch. 2015;466(5):485-93.

68. Kai K, Aishima S, Aoki S, Takase Y, Uchihashi K, Masuda M, et al. Cytokeratin immunohistochemistry improves interobserver variability between unskilled pathologists in the evaluation of tumor budding in T1 colorectal cancer. Pathol Int. 2016;66(2):75-82.

69. Hipp J, Flotte T, Monaco J, Cheng J, Madabhushi A, Yagi Y, et al. Computer aided diagnostic tools aim to empower rather than replace pathologists: Lessons learned from computational chess. J Pathol Inform. 2011;2:25.

70. Soltermann A, Tischler V, Arbogast S, Braun J, Probst-Hensch N, Weder W, et al. Prognostic significance of epithelial-mesenchymal and mesenchymal-epithelial transition protein expression in non-small cell lung cancer. Clin Cancer Res. 2008;14(22):7430-7.

71. Cerami E, Gao J, Dogrusoz U, Gross BE, Sumer SO, Aksoy BA, et al. The cBio cancer genomics portal: an open platform for exploring multidimensional cancer genomics data. Cancer Discov. 2012;2(5):401-4.

72. Astolfo A, Lathuiliere A, Laversenne V, Schneider B, Stampanoni M. Amyloid-beta plaque deposition measured using propagation-based X-ray phase contrast CT imaging. J Synchrotron Radiat. 2016;23(Pt 3):813-9.

73. Schindelin J, Arganda-Carreras I, Frise E, Kaynig V, Longair M, Pietzsch T, et al. Fiji: an open-source platform for biological-image analysis. Nat Methods. 2012;9(7):676-82.

74. Wisniewski JR, Zougman A, Nagaraj N, Mann M. Universal sample preparation method for proteome analysis. Nat Methods. 2009;6(5):359-62.

75. Tusher VG, Tibshirani R, Chu G. Significance analysis of microarrays applied to the ionizing radiation response. Proc Natl Acad Sci U S A. 2001;98(9):5116-21.

76. Wang J, Duncan D, Shi Z, Zhang B. WEB-based GEne SeT AnaLysis Toolkit (WebGestalt): update 2013. Nucleic Acids Res. 2013;41(Web Server issue):W77-83.

77. Shannon P, Markiel A, Ozier O, Baliga NS, Wang JT, Ramage D, et al. Cytoscape: a software environment for integrated models of biomolecular interaction networks. Genome Res. 2003;13(11):2498-504.

78. Maere S, Heymans K, Kuiper M. BiNGO: a Cytoscape plugin to assess overrepresentation of gene ontology categories in biological networks. Bioinformatics. 2005;21(16):3448-9.

79. Merico D, Isserlin R, Stueker O, Emili A, Bader GD. Enrichment map: a network-based method for gene-set enrichment visualization and interpretation. PLoS One. 2010;5(11):e13984.

80. Kanehisa M, Sato Y, Kawashima M, Furumichi M, Tanabe M. KEGG as a reference resource for gene and protein annotation. Nucleic Acids Res. 2016;44(D1):D457-62.

81. Punt CJ, Buyse M, Kohne CH, Hohenberger P, Labianca R, Schmoll HJ, et al. Endpoints in adjuvant treatment trials: a systematic review of the literature in colon cancer and proposed definitions for future trials. J Natl Cancer Inst. 2007;99(13):998-1003.

82. Yilmaz M, Christofori G, Lehembre F. Distinct mechanisms of tumor invasion and metastasis. Trends Mol Med. 2007;13(12):535-41.

83. Friedl P, Alexander S. Cancer invasion and the microenvironment: plasticity and reciprocity. Cell. 2011;147(5):992-1009.

84. Yamaguchi H, Wyckoff J, Condeelis J. Cell migration in tumors. Curr Opin Cell Biol. 2005;17(5):559-64.

85. Marx J. Cell biology. Podosomes and invadopodia help mobile cells step lively. Science. 2006;312(5782):1868-9.

86. Friedl P, Wolf K. Tube travel: the role of proteases in individual and collective cancer cell invasion. Cancer Res. 2008;68(18):7247-9.

87. Gillan L, Matei D, Fishman DA, Gerbin CS, Karlan BY, Chang DD. Periostin secreted by epithelial ovarian carcinoma is a ligand for alpha(V)beta(3) and alpha(V)beta(5) integrins and promotes cell motility. Cancer Res. 2002;62(18):5358-64.

88. Yan W, Shao R. Transduction of a mesenchyme-specific gene periostin into 293T cells induces cell invasive activity through epithelial-mesenchymal transformation. J Biol Chem. 2006;281(28):19700-8.

89. Butcher JT, Norris RA, Hoffman S, Mjaatvedt CH, Markwald RR. Periostin promotes atrioventricular mesenchyme matrix invasion and remodeling mediated by integrin signaling through Rho/PI 3-kinase. Dev Biol. 2007;302(1):256-66.

90. Soltermann A, Ossola R, Kilgus-Hawelski S, von Eckardstein A, Suter T, Aebersold R, et al. N-glycoprotein profiling of lung adenocarcinoma pleural effusions by shotgun proteomics. Cancer. 2008;114(2):124-33.

91. Shimazaki M, Nakamura K, Kii I, Kashima T, Amizuka N, Li M, et al. Periostin is essential for cardiac healing after acute myocardial infarction. J Exp Med. 2008;205(2):295-303.

92. Isogai Z, Shinomura T, Yamakawa N, Takeuchi J, Tsuji T, Heinegard D, et al. 2B1 antigen characteristically expressed on extracellular matrices of human malignant tumors is a large chondroitin sulfate proteoglycan, PG-M/versican. Cancer Res. 1996;56(17):3902-8.

93. Pirinen R, Leinonen T, Bohm J, Johansson R, Ropponen K, Kumpulainen E, et al. Versican in nonsmall cell lung cancer: relation to hyaluronan, clinicopathologic factors, and prognosis. Hum Pathol. 2005;36(1):44-50.

94. Kim S, Takahashi H, Lin WW, Descargues P, Grivennikov S, Kim Y, et al. Carcinoma-produced factors activate myeloid cells through TLR2 to stimulate metastasis. Nature. 2009;457(7225):102-6.

95. Balendiran GK, Dabur R, Fraser D. The role of glutathione in cancer. Cell Biochem Funct. 2004;22(6):343-52.

96. Oyama T, Kagawa N, Kunugita N, Kitagawa K, Ogawa M, Yamaguchi T, et al. Expression of cytochrome P450 in tumor tissues and its association with cancer development. Front Biosci. 2004;9:1967-76.

97. Rodriguez-Antona C, Ingelman-Sundberg M. Cytochrome P450 pharmacogenetics and cancer. Oncogene. 2006;25(11):1679-91.

98. Hase K, Shatney C, Johnson D, Trollope M, Vierra M. Prognostic value of tumor "budding" in patients with colorectal cancer. Dis Colon Rectum. 1993;36(7):627-35.

99. Ueno H, Murphy J, Jass JR, Mochizuki H, Talbot IC. Tumour 'budding' as an index to estimate the potential of aggressiveness in rectal cancer. Histopathology. 2002;40(2):127-32.

100. Mitrovic B, Schaeffer DF, Riddell RH, Kirsch R. Tumor budding in colorectal carcinoma: time to take notice. Mod Pathol. 2012;25(10):1315-25.

101. Bronsert P, Enderle-Ammour K, Bader M, Timme S, Kuehs M, Csanadi A, et al. Cancer cell invasion and EMT marker expression: a three-dimensional study of the human cancer-host interface. J Pathol. 2014;234(3):410-22.

102. Yu K-H, Zhang C, Berry GJ, Altman RB, Ré C, Rubin DL, et al. Predicting non-small cell lung cancer prognosis by fully automated microscopic pathology image features. Nature Communications. 2016;7:12474.

103. Song WA, Zhou NK, Wang W, Chu XY, Liang CY, Tian XD, et al. Survival benefit of neoadjuvant chemotherapy in non-small cell lung cancer: an updated meta-analysis of 13 randomized control trials. J Thorac Oncol. 2010;5(4):510-6.

104. Group NM-aC. Preoperative chemotherapy for non-small-cell lung cancer: a systematic review and meta-analysis of individual participant data. Lancet. 2014;383(9928):1561-71.

105. Junker K, Thomas M, Schulmann K, Klinke F, Bosse U, Muller KM. Tumour regression in non-small-cell lung cancer following neoadjuvant therapy. Histological assessment. J Cancer Res Clin Oncol. 1997;123(9):469-77.

106. Junker K, Langner K, Klinke F, Bosse U, Thomas M. Grading of tumor regression in non-small cell lung cancer : morphology and prognosis. Chest. 2001;120(5):1584-91.

107. Pataer A, Kalhor N, Correa AM, Raso MG, Erasmus JJ, Kim ES, et al. Histopathologic response criteria predict survival of patients with resected lung cancer after neoadjuvant chemotherapy. J Thorac Oncol. 2012;7(5):825-32.

108. Yamane Y, Ishii G, Goto K, Kojima M, Nakao M, Shimada Y, et al. A novel histopathological evaluation method predicting the outcome of non-small cell lung cancer treated by neoadjuvant therapy: the prognostic importance of the area of residual tumor. J Thorac Oncol. 2010;5(1):49-55.

109. Goto M, Naito M, Saruwatari K, Hisakane K, Kojima M, Fujii S, et al. The ratio of cancer cells to stroma after induction therapy in the treatment of non-small cell lung cancer. J Cancer Res Clin Oncol. 2017;143(2):215-23.

110. Burger IA, Casanova R, Steiger S, Husmann L, Stolzmann P, Huellner MW, et al. 18F-FDG PET/CT of Non-Small Cell Lung Carcinoma Under Neoadjuvant Chemotherapy: Background-Based Adaptive-Volume Metrics Outperform TLG and MTV in Predicting Histopathologic Response. J Nucl Med. 2016;57(6):849-54.

111. Rota M, Antolini L, Valsecchi MG. Optimal cut-point definition in biomarkers: the case of censored failure time outcome. BMC Med Res Methodol. 2015;15:24.

112. Liu-Jarin X, Stoopler MB, Raftopoulos H, Ginsburg M, Gorenstein L, Borczuk AC. Histologic assessment of non-small cell lung carcinoma after neoadjuvant therapy. Mod Pathol. 2003;16(11):1102-8.

113. Hellmann MD, Chaft JE, William WN, Jr., Rusch V, Pisters KM, Kalhor N, et al. Pathological response after neoadjuvant chemotherapy in resectable non-small-cell lung cancers: proposal for the use of major pathological response as a surrogate endpoint. Lancet Oncol. 2014;15(1):e42-50.

114. William WN, Jr., Pataer A, Kalhor N, Correa AM, Rice DC, Wistuba, II, et al. Computed tomography RECIST assessment of histopathologic response and prediction of survival in patients with resectable non-small-cell lung cancer after neoadjuvant chemotherapy. J Thorac Oncol. 2013;8(2):222-8.

115. Pottgen C, Stuschke M, Graupner B, Theegarten D, Gauler T, Jendrossek V, et al. Prognostic model for long-term survival of locally advanced non-small-cell lung cancer patients after neoadjuvant radiochemotherapy and resection integrating clinical and histopathologic factors. BMC Cancer. 2015;15:363.

116. Milleron B, Westeel V, Gounant V, Wislez M, Quoix E. [Pathological complete response: A predictive survival factor after neoadjuvant chemotherapy in lung cancer]. Bull Cancer. 2016;103(1):66-72.

117. Kim AW, Liptay MJ, Bonomi P, Warren WH, Basu S, Farlow EC, et al. Neoadjuvant chemoradiation for clinically advanced non-small cell lung cancer: an analysis of 233 patients. Ann Thorac Surg. 2011;92(1):233-41; discussion 41-3.

118. Liu H, Zhang T, Ye J, Li H, Huang J, Li X, et al. Tumor-infiltrating lymphocytes predict response to chemotherapy in patients with advance non-small cell lung cancer. Cancer Immunol Immunother. 2012;61(10):1849-56.

119. Cuaron J, Dunphy M, Rimner A. Role of FDG-PET scans in staging, response assessment, and follow-up care for non-small cell lung cancer. Front Oncol. 2012;2:208.

120. Nahmias C, Hanna WT, Wahl LM, Long MJ, Hubner KF, Townsend DW. Time course of early response to chemotherapy in non-small cell lung cancer patients with 18F-FDG PET/CT. J Nucl Med. 2007;48(5):744-51.

121. Pottgen C, Levegrun S, Theegarten D, Marnitz S, Grehl S, Pink R, et al. Value of 18F-fluoro-2-deoxy-D-glucose-positron emission tomography/computed tomography in non-small-cell lung cancer for prediction of pathologic response and times to relapse after neoadjuvant chemoradiotherapy. Clin Cancer Res. 2006;12(1):97-106.

122. Ryu JS, Choi NC, Fischman AJ, Lynch TJ, Mathisen DJ. FDG-PET in staging and restaging non-small cell lung cancer after neoadjuvant chemoradiotherapy: correlation with histopathology. Lung Cancer. 2002;35(2):179-87.

123. Cerfolio RJ, Ojha B, Mukherjee S, Pask AH, Bass CS, Katholi CR. Positron emission tomography scanning with 2-fluoro-2-deoxy-d-glucose as a predictor of response of neoadjuvant treatment for non-small cell carcinoma. J Thorac Cardiovasc Surg. 2003;125(4):938-44.

124. Cerfolio RJ, Bryant AS, Winokur TS, Ohja B, Bartolucci AA. Repeat FDG-PET after neoadjuvant therapy is a predictor of pathologic response in patients with non-small cell lung cancer. Ann Thorac Surg. 2004;78(6):1903-9; discussion 9.

125. Schmucking M, Baum RP, Bonnet R, Junker K, Muller KM. [Correlation of histologic results with PET findings for tumor regression and survival in locally advanced non-small cell lung cancer after neoadjuvant treatment]. Pathologe. 2005;26(3):178-89.

126. Lococo F, Galeone C, Formisano D, Bellafiore S, Filice A, Annunziata T, et al. 18F-fluorodeoxyglucose positron emission tomographic scan in solid-type p-stage-I pulmonary adenocarcinomas: what can produce false-negative results? Eur J Cardiothorac Surg. 2017;51(4):667-73.

127. Vesselle H, Salskov A, Turcotte E, Wiens L, Schmidt R, Jordan CD, et al. Relationship between non-small cell lung cancer FDG uptake at PET, tumor histology, and Ki-67 proliferation index. J Thorac Oncol. 2008;3(9):971-8.

128. Jeong HJ, Min JJ, Park JM, Chung JK, Kim BT, Jeong JM, et al. Determination of the prognostic value of [(18)F]fluorodeoxyglucose uptake by using positron emission tomography in patients with non-small cell lung cancer. Nucl Med Commun. 2002;23(9):865-70.

129. Downey RJ, Akhurst T, Gonen M, Vincent A, Bains MS, Larson S, et al. Preoperative F-18 fluorodeoxyglucose-positron emission tomography maximal standardized uptake value predicts survival after lung cancer resection. J Clin Oncol. 2004;22(16):3255-60.

130. Cerfolio RJ, Bryant AS, Ohja B, Bartolucci AA. The maximum standardized uptake values on positron emission tomography of a non-small cell lung cancer predict stage, recurrence, and survival. J Thorac Cardiovasc Surg. 2005;130(1):151-9.

131. Eschmann SM, Friedel G, Paulsen F, Reimold M, Hehr T, Budach W, et al. Is standardised (18)F-FDG uptake value an outcome predictor in patients with stage III non-small cell lung cancer? Eur J Nucl Med Mol Imaging. 2006;33(3):263-9.

132. Wahl RL, Jacene H, Kasamon Y, Lodge MA. From RECIST to PERCIST: Evolving Considerations for PET response criteria in solid tumors. J Nucl Med. 2009;50 Suppl 1:122S-50S.

133. Mac Manus MP, Hicks RJ, Matthews JP, McKenzie A, Rischin D, Salminen EK, et al. Positron emission tomography is superior to computed tomography scanning for response-assessment after radical radiotherapy or chemoradiotherapy in patients with non-small-cell lung cancer. J Clin Oncol. 2003;21(7):1285-92.

134. Poettgen C, Theegarten D, Eberhardt W, Levegruen S, Gauler T, Krbek T, et al. Correlation of PET/CT findings and histopathology after neoadjuvant therapy in non-small cell lung cancer. Oncology. 2007;73(5-6):316-23.

135. de Geus-Oei LF, van der Heijden HF, Visser EP, Hermsen R, van Hoorn BA, Timmer-Bonte JN, et al. Chemotherapy response evaluation with 18F-FDG PET in patients with non-small cell lung cancer. J Nucl Med. 2007;48(10):1592-8.

136. Chung HW, Lee KY, Kim HJ, Kim WS, So Y. FDG PET/CT metabolic tumor volume and total lesion glycolysis predict prognosis in patients with advanced lung adenocarcinoma. J Cancer Res Clin Oncol. 2014;140(1):89-98.

137. Melloni G, Gajate AM, Sestini S, Gallivanone F, Bandiera A, Landoni C, et al. New positron emission tomography derived parameters as predictive factors for recurrence in resected stage I non-small cell lung cancer. Eur J Surg Oncol. 2013;39(11):1254-61.

138. Zaizen Y, Azuma K, Kurata S, Sadashima E, Hattori S, Sasada T, et al. Prognostic significance of total lesion glycolysis in patients with advanced non-small cell lung cancer receiving chemotherapy. Eur J Radiol. 2012;81(12):4179-84.

139. Zhang H, Wroblewski K, Liao S, Kampalath R, Penney BC, Zhang Y, et al. Prognostic value of metabolic tumor burden from (18)F-FDG PET in surgical patients with non-small-cell lung cancer. Acad Radiol. 2013;20(1):32-40.

140. Chen HH, Chiu NT, Su WC, Guo HR, Lee BF. Prognostic value of whole-body total lesion glycolysis at pretreatment FDG PET/CT in non-small cell lung cancer. Radiology. 2012;264(2):559-66.

141. Larson SM, Erdi Y, Akhurst T, Mazumdar M, Macapinlac HA, Finn RD, et al. Tumor Treatment Response Based on Visual and Quantitative Changes in Global Tumor Glycolysis Using PET-FDG Imaging. The Visual Response Score and the Change in Total Lesion Glycolysis. Clin Positron Imaging. 1999;2(3):159-71.

142. Hyun SH, Ahn HK, Kim H, Ahn MJ, Park K, Ahn YC, et al. Volume-based assessment by (18)F-FDG PET/CT predicts survival in patients with stage III non-small-cell lung cancer. Eur J Nucl Med Mol Imaging. 2014;41(1):50-8.

143. Usmanij EA, de Geus-Oei LF, Troost EG, Peters-Bax L, van der Heijden EH, Kaanders JH, et al. 18F-FDG PET early response evaluation of locally advanced non-small cell lung cancer treated with concomitant chemoradiotherapy. J Nucl Med. 2013;54(9):1528-34.

144. Chang KP, Tsang NM, Liao CT, Hsu CL, Chung MJ, Lo CW, et al. Prognostic significance of 18F-FDG PET parameters and plasma Epstein-Barr virus DNA load in patients with nasopharyngeal carcinoma. J Nucl Med. 2012;53(1):21-8.

145. Vargas HA, Burger IA, Goldman DA, Micco M, Sosa RE, Weber W, et al. Volume-based quantitative FDG PET/CT metrics and their association with optimal debulking and progression-free survival in patients with recurrent ovarian cancer undergoing secondary cytoreductive surgery. Eur Radiol. 2015;25(11):3348-53.

146. Gallicchio R, Mansueto G, Simeon V, Nardelli A, Guariglia R, Capacchione D, et al. F-18 FDG PET/CT quantization parameters as predictors of outcome in patients with diffuse large B-cell lymphoma. Eur J Haematol. 2014;92(5):382-9.

147. Burger IA, Vargas HA, Apte A, Beattie BJ, Humm JL, Gonen M, et al. PET quantification with a histogram derived total activity metric: superior quantitative consistency compared to total lesion glycolysis with absolute or relative SUV thresholds in phantoms and lung cancer patients. Nucl Med Biol. 2014;41(5):410-8.

148. Lee JW, Kang CM, Choi HJ, Lee WJ, Song SY, Lee JH, et al. Prognostic Value of Metabolic Tumor Volume and Total Lesion Glycolysis on Preoperative (1)(8)F-FDG PET/CT in Patients with Pancreatic Cancer. J Nucl Med. 2014;55(6):898-904.

149. Chung HH, Kim JW, Han KH, Eo JS, Kang KW, Park NH, et al. Prognostic value of metabolic tumor volume measured by FDG-PET/CT in patients with cervical cancer. Gynecol Oncol. 2011;120(2):270-4.

150. Seol YM, Kwon BR, Song MK, Choi YJ, Shin HJ, Chung JS, et al. Measurement of tumor volume by PET to evaluate prognosis in patients with head and neck cancer treated by chemo-radiation therapy. Acta Oncol. 2010;49(2):201-8.

151. Burger IA, Vargas HA, Beattie BJ, Goldman DA, Zheng J, Larson SM, et al. How to assess background activity: introducing a histogram-based analysis as a first step for accurate one-step PET quantification. Nucl Med Commun. 2014;35(3):316-24.

152. Vansteenkiste J, De Ruysscher D, Eberhardt WE, Lim E, Senan S, Felip E, et al. Early and locally advanced non-small-cell lung cancer (NSCLC): ESMO Clinical Practice Guidelines for diagnosis, treatment and follow-up. Ann Oncol. 2013;24 Suppl 6:vi89-98.

153. Formula for geometrical figures, http://www.science.co.il/Formula.asp.

154. Fluss R, Faraggi D, Reiser B. Estimation of the Youden Index and its associated cutoff point. Biom J. 2005;47(4):458-72.

155. Burger IA, Schwarz EI, Samarin A, Breitenstein S, Weber A, Hany TF. Correlation between therapy response assessment using FDG PET/CT and histopathologic tumor regression grade in hepatic metastasis of colorectal carcinoma after neoadjuvant therapy. Ann Nucl Med. 2013;27(2):177-83.

156. Capirci C, Rampin L, Erba PA, Galeotti F, Crepaldi G, Banti E, et al. Sequential FDG-PET/CT reliably predicts response of locally advanced rectal cancer to neo-adjuvant chemo-radiation therapy. Eur J Nucl Med Mol Imaging. 2007;34(10):1583-93.

157. Palma P, Conde-Muino R, Rodriguez-Fernandez A, Segura-Jimenez I, Sanchez-Sanchez R, Martin-Cano J, et al. The value of metabolic imaging to predict tumour response after chemoradiation in locally advanced rectal cancer. Radiat Oncol. 2010;5:119.

158. Erdi YE, Mawlawi O, Larson SM, Imbriaco M, Yeung H, Finn R, et al. Segmentation of lung lesion volume by adaptive positron emission tomography image thresholding. Cancer. 1997;80(12 Suppl):2505-9.

159. Nestle U, Kremp S, Schaefer-Schuler A, Sebastian-Welsch C, Hellwig D, Rube C, et al. Comparison of different methods for delineation of 18F-FDG PET-positive tissue for target volume definition in radiotherapy of patients with non-Small cell lung cancer. J Nucl Med. 2005;46(8):1342-8.

160. Orlhac F, Soussan M, Maisonobe JA, Garcia CA, Vanderlinden B, Buvat I. Tumor texture analysis in 18F-FDG PET: relationships between texture parameters, histogram indices, standardized uptake values, metabolic volumes, and total lesion glycolysis. J Nucl Med. 2014;55(3):414-22.

161. Kothari S, Phan JH, Stokes TH, Wang MD. Pathology imaging informatics for quantitative analysis of whole-slide images. J Am Med Inform Assoc. 2013;20(6):1099-108.

162. Baak JP. The principles and advances of quantitative pathology. Anal Quant Cytol Histol. 1987;9(2):89-95.

163. Ramos-Vara JA, Miller MA. When tissue antigens and antibodies get along: revisiting the technical aspects of immunohistochemistry--the red, brown, and blue technique. Vet Pathol. 2014;51(1):42-87.

164. Rimm DL. What brown cannot do for you. Nat Biotechnol. 2006;24(8):914-6.

165. Arteaga CL, Sliwkowski MX, Osborne CK, Perez EA, Puglisi F, Gianni L. Treatment of HER2-positive breast cancer: current status and future perspectives. Nat Rev Clin Oncol. 2011;9(1):16-32.

166. Wolff AC, Hammond ME, Hicks DG, Dowsett M, McShane LM, Allison KH, et al. Recommendations for human epidermal growth factor receptor 2 testing in breast cancer: American Society of Clinical Oncology/College of American Pathologists clinical practice guideline update. J Clin Oncol. 2013;31(31):3997-4013.

167. Lim TH, Lim AS, Thike AA, Tien SL, Tan PH. Implications of the Updated 2013 American Society of Clinical Oncology/College of American Pathologists Guideline Recommendations on Human Epidermal Growth Factor Receptor 2 Gene Testing Using Immunohistochemistry and Fluorescence In Situ Hybridization for Breast Cancer. Arch Pathol Lab Med. 2016;140(2):140-7.

168. Pauletti G, Godolphin W, Press MF, Slamon DJ. Detection and quantitation of HER-2/neu gene amplification in human breast cancer archival material using fluorescence in situ hybridization. Oncogene. 1996;13(1):63-72.

169. Thomson TA, Hayes MM, Spinelli JJ, Hilland E, Sawrenko C, Phillips D, et al. HER-2/neu in breast cancer: interobserver variability and performance of immunohistochemistry with 4 antibodies compared with fluorescent in situ hybridization. Mod Pathol. 2001;14(11):1079-86.

170. Matos LL, Trufelli DC, de Matos MG, da Silva Pinhal MA. Immunohistochemistry as an important tool in biomarkers detection and clinical practice. Biomark Insights. 2010;5:9-20.

171. Fedchenko N, Reifenrath J. Different approaches for interpretation and reporting of immunohistochemistry analysis results in the bone tissue - a review. Diagn Pathol. 2014;9:221.

172. Janowczyk A, Madabhushi A. Deep learning for digital pathology image analysis: A comprehensive tutorial with selected use cases. J Pathol Inform. 2016;7:29.

173. Sirinukunwattana K, Ahmed Raza SE, Yee-Wah T, Snead DR, Cree IA, Rajpoot NM. Locality Sensitive Deep Learning for Detection and Classification of Nuclei in Routine Colon Cancer Histology Images. IEEE Trans Med Imaging. 2016;35(5):1196-206.

174. Song Y, Zhang L, Chen S, Ni D, Li B, Zhou Y, et al. A deep learning based framework for accurate segmentation of cervical cytoplasm and nuclei. Conf Proc IEEE Eng Med Biol Soc. 2014;2014:2903-6.

175. Albarqouni S, Baur C, Achilles F, Belagiannis V, Demirci S, Navab N. AggNet: Deep Learning From Crowds for Mitosis Detection in Breast Cancer Histology Images. IEEE Trans Med Imaging. 2016;35(5):1313-21.

176. Ciresan DC, Giusti A, Gambardella LM, Schmidhuber J. Mitosis detection in breast cancer histology images with deep neural networks. Med Image Comput Comput Assist Interv. 2013;16(Pt 2):411-8.

177. Ertosun MG, Rubin DL. Automated Grading of Gliomas using Deep Learning in Digital Pathology Images: A modular approach with ensemble of convolutional neural networks. AMIA Annu Symp Proc. 2015;2015:1899-908.

178. Sieren JC, Weydert J, Bell A, De Young B, Smith AR, Thiesse J, et al. An automated segmentation approach for highlighting the histological complexity of human lung cancer. Ann Biomed Eng. 2010;38(12):3581-91.

179. Novello S, Barlesi F, Califano R, Cufer T, Ekman S, Levra MG, et al. Metastatic non-small-cell lung cancer: ESMO Clinical Practice Guidelines for diagnosis, treatment and follow-up. Ann Oncol. 2016;27(suppl 5):v1-v27.

180. Eisenhauer EA, Therasse P, Bogaerts J, Schwartz LH, Sargent D, Ford R, et al. New response evaluation criteria in solid tumours: revised RECIST guideline (version 1.1). Eur J Cancer. 2009;45(2):228-47.